

**AUTONOMOUS CONTROL OF PARAFOIL AND
PAYLOAD SYSTEMS USING UPPER SURFACE
CANOPY SPOILERS**

A Thesis
Presented to
The Academic Faculty

by

Edward J. Scheuermann

In Partial Fulfillment
of the Requirements for the Degree
Doctor of Philosophy in the
School of Mechanical Engineering

Georgia Institute of Technology
August 2015

Copyright © 2015 by Edward J. Scheuermann

AUTONOMOUS CONTROL OF PARAFOIL AND PAYLOAD SYSTEMS USING UPPER SURFACE CANOPY SPOILERS

Approved by:

Dr. Mark Costello, Advisor
School of Aerospace Engineering
School of Mechanical Engineering
Georgia Institute of Technology

Dr. Aldo Ferri
School of Mechanical Engineering
Georgia Institute of Technology

Dr. Ari Glezer
School of Mechanical Engineering
School of Aerospace Engineering
Georgia Institute of Technology

Dr. Eric Johnson
School of Aerospace Engineering
Georgia Institute of Technology

Dr. Keith Bergeron
Natick Soldier Research, Development
and Engineering Center
U.S. Army

Date Approved: 29 April 2015

To my Mother, Father, and Sister.

ACKNOWLEDGEMENTS

I would first like to thank my advisor, Dr. Mark Costello, for his time, effort, and guidance over these past 5 years. His commitment to research and his students is truly inspiring. I would also like to thank my committee for their time and insightful contributions to this dissertation. Additionally, I would like to acknowledge the support of the Natick Soldier Research, Development, and Engineering Center and Dr. Keith Bergeron, Dr. Gregory Noetscher, and Michael Shurtliff. Their enthusiasm and support for these projects is very much appreciated.

Throughout my time at Georgia Tech, I have made many great friends without whom this accomplishment would not have been possible. I wish to thank all past and present members of Dr. Costello's research group for their advice and assistance with countless technical issues throughout my time as a graduate student. Additionally, I want to thank Dr. Michael Ward for his generosity, dedication, and invaluable insight for all things airdrop related. Mike has been right there with me through all the long days (and nights) of preparation and flight testing and is truly a great colleague and friend.

Lastly, I would like to thank my closest friends and family. John Dykes and Jeff Kornuta have been not only great friends and colleagues for many years, but a great source of technical knowledge and encouragement since our earliest days at LSU. I would also like to thank Crystal Bergeron for her unending kindness and support through these past few years. Finally, I want to thank my mother and father for all of the love, support, and encouragement they have given me through all of life's challenges. I could not have arrived at this point without them, and to them I am sincerely grateful.

TABLE OF CONTENTS

DEDICATION	iii
ACKNOWLEDGEMENTS	iv
LIST OF TABLES	viii
LIST OF FIGURES	ix
SUMMARY	xiii
I INTRODUCTION	1
1.1 Airdrop Technology Overview	1
1.2 Bleed Air Control of Parafoil Aircraft	6
1.3 Contributions of the Thesis	9
1.4 Thesis Outline	10
II FLIGHT DYNAMIC MODEL	13
2.1 Mathematical Nomenclature and Convention	14
2.2 Equations of Motion	15
2.2.1 Kinematics	15
2.2.2 Dynamics	16
2.3 Sensor Model	24
2.4 Wind Model	25
III SMALL SCALE TEST VEHICLE PLATFORM	27
3.1 Hardware Description	27
3.2 Canopy Modifications	29
3.3 System Identification	31
3.3.1 Parafoil and Payload System Identification Overview	32
3.3.2 Extracting Steady-State Lift, Drag, and Turn Rate	34
3.3.3 Flight Test Results	38
3.3.4 Aerodynamics Summary	43

IV GUIDANCE, NAVIGATION, AND CONTROL ALGORITHM	46
4.1 Guidance	46
4.1.1 Initialization	48
4.1.2 Loiter	48
4.1.3 Final Approach	51
4.1.4 Terminal Guidance	52
4.2 Navigation	53
4.3 Control	57
4.4 Example Autonomous Flight	60
V AUTONOMOUS LANDING PERFORMANCE	63
5.1 Lateral Control Only	63
5.2 Combined Lateral and Longitudinal Control	70
5.3 Summary and Comparison with Conventional Control Mechanisms .	76
VI IN-CANOPY BLEED AIR ACTUATION SYSTEM	79
6.1 Benefits of In-Canopy Bleed Air Actuation	80
6.2 In-Canopy Hardware Description	83
6.2.1 Actuator Mounting and Rigging	83
6.2.2 Detailed Actuator Design	85
6.2.3 Payload Relay Box and Ground Station Interface	90
VII FLIGHT TESTING OF IN-CANOPY HARDWARE	95
7.1 Vehicle Overview and Flight Testing Protocol	95
7.2 Control Authority Using In-Canopy Hardware	98
7.2.1 Lateral Control Authority	101
7.2.2 Longitudinal Control Authority	103
7.3 In-Canopy Bleed Air Actuation Force Study	104
VIII IN-CANOPY AUTONOMOUS LANDING PERFORMANCE	108
8.1 Simulation Model Modifications	108
8.1.1 Canopy Aerodynamics	109

8.1.2	Actuator Model	113
8.2	In-Canopy Steering and Glide Slope Control	117
8.2.1	Lateral Steering Only	117
8.2.2	Combined Lateral and Longitudinal Control	119
8.3	Autonomous Landing Performance in Simulation	123
8.4	Autonomous Landing Performance in Flight Tests	127
IX	CONCLUSIONS AND FUTURE WORK	130
9.1	Conclusions	130
9.2	Recommended Future Work	131
REFERENCES		134
VITA		138

LIST OF TABLES

2.1	GPS sensor error parameters [39].	24
3.1	Test vehicle geometric and mass properties.	43
3.2	Test vehicle aerodynamic coefficient summary.	44
4.1	Error parameters for position and velocity estimator.	54
4.2	Error parameters for heading, heading rate, and wind estimator [57].	57
5.1	Monte Carlo simulation parameters.	64
5.2	Simulation and experimental landing accuracy statistics.	76
5.3	Comparison of landing accuracies using upper surface canopy spoilers with conventional control mechanisms.	77
6.1	In-canopy actuator motor catalog specifications.	88
8.1	MC-4/5 system geometric and mass properties.	111
8.2	MC-4/5 system aerodynamic coefficient summary.	111
8.3	MC-4/5 in-canopy actuator model parameters.	116
8.4	MC-4/5 Monte Carlo simulation parameters.	124

LIST OF FIGURES

1.1	Typical aerial cargo delivery systems using (a) round parachutes [3] and (b) autonomously guided ram air parafoil canopy [4].	2
1.2	Firefly 2K parafoil canopy from Airborne Systems [12].	4
1.3	NASA X38 with 7,500 ft ² canopy deployed [16].	5
1.4	Typical guided parafoil aircraft flight plan [14].	7
1.5	Upper surface canopy spoilers during test flight of 100 ft ² canopy. Image courtesy of the US Army Natick Soldier Research, Development, and Engineering Center (NSRDEC).	8
2.1	Parafoil and payload system dynamic model.	15
3.1	Test vehicle in gliding flight shown with (a) Canopy 1 and (b) Canopy 2.	28
3.2	Onboard autopilot and sensing suite.	29
3.3	Cross-section view of upper surface canopy spoiler control mechanism.	29
3.4	Upper surface canopy spoiler control mechanism (front view).	30
3.5	Specialized parafoil system identification method [54].	34
3.6	Parafoil ground track velocity decomposition.	35
3.7	Parafoil side view (left) and front view (right) illustrating lift and drag relationship during steady turn.	38
3.8	Measured test vehicle turn rate vs. normalized asymmetric spoiler deflection.	39
3.9	Measured test vehicle turn rate vs. normalized asymmetric spoiler deflection.	40
3.10	Open-loop turn rate tracking using Canopy 1.	41
3.11	Steady-state flight characteristics versus normalized symmetric spoiler deflection δ_s including: (a) airspeed, (b) descent rate, and (c) glide slope.	42
3.12	Test vehicle lift coefficient versus angle of attack for several different values of symmetric spoiler deflection.	45
3.13	Test vehicle drag coefficient versus angle of attack for several different values of symmetric spoiler deflection.	45
4.1	Wind fixed reference frame.	47
4.2	T-shaped loiter pattern relative to the wind fixed frame.	49

4.3	Instantaneous distance to target.	50
4.4	Terminal guidance strategy.	51
4.5	Parafoil ground track velocity decomposition.	55
4.6	Inertial frame trajectory for example simulated autonomous flight. . .	60
4.7	Wind fixed frame trajectory for example simulated autonomous flight. .	61
4.8	Actual and estimated winds for example simulated autonomous flight.	62
4.9	Heading angle and heading rate estimates and tracking.	62
5.1	Landing dispersion for 250 simulated autonomous landings using upper surface canopy spoilers for lateral steering only.	65
5.2	Simulated mean landing accuracy vs. mean wind speed for several different levels of turbulence (lateral steering control only).	66
5.3	Example wind profiles for two different turbulence levels.	67
5.4	Landing dispersion for 31 autonomous flights using upper surface canopy spoilers for lateral steering only.	69
5.5	Simulated landing dispersion for (left) lateral only control and (right) combined lateral and longitudinal control.	71
5.6	Altitude (top) and normalized control input (bottom) versus instantaneous distance from the target for example autonomous flight trajectory.	72
5.7	Landing accuracy comparison between lateral only control and combined lateral and longitudinal control vs. turbulence for different values of mean wind.	73
5.8	Flight testing operations in Eloy, AZ.	74
5.9	Experimental landing dispersion (left) and calculated miss distance versus estimated mean wind speed (right) for 70 autonomous flight tests using upper surface canopy spoilers for combined lateral and longitudinal control.	75
6.1	Large scale autonomous parafoil and payload system in flight (front view). [12]	80
6.2	Canopy front view showing spoiler actuation from system AGU. . . .	81
6.3	In-canopy actuator mounting configuration (front view).	84
6.4	In-canopy actuator control line routing for signal spoiler and dual spoiler configurations.	85
6.5	In-canopy actuator exploded component view.	86

6.6	In-canopy actuator mounted within MC-4/5 parachute prior to flight test.	87
6.7	In-canopy actuator motor comparison.	88
6.8	Motor torque vs. winding current.	89
6.9	In-canopy actuator electronics.	90
6.10	Payload relay box internal components (left) and mounted on MC-4/5 AGU (right) prior to test flight.	91
6.11	In-canopy actuation system wireless network topology.	92
6.12	Flight control tab of ground station graphical user interface (GUI). . .	93
6.13	Controller gains tab of ground station graphical user interface (GUI). .	93
6.14	Navigation/Guidance tab of ground station graphical user interface (GUI).	94
7.1	MC-4/5 parafoil canopy in flight and internal view of in-canopy actuator. .	96
7.2	MC-4/5 in-canopy actuator configuration (canopy front view).	97
7.3	MC-4/5 control line slack measurement.	99
7.4	MC-4/5 inflated cell measurements.	100
7.5	MC-4/5 turn rate during flight test using in-canopy actuators.	101
7.6	Asymmetric spoiler configurations during MC-4/5 flight test.	102
7.7	MC-4/5 steady-state flight characteristics using in-canopy bleed air actuators versus turn rate including: (a) airspeed, (b) descent rate, and (c) glide ratio.	103
7.8	Vertical actuation force vs. vertical displacement of the upper surface spoiler opening using in-canopy actuators.	105
7.9	MC-4/5 turn rate during flight test using in-canopy actuators.	106
8.1	MC-4/5 in-canopy actuator location and naming convention.	109
8.2	Comparison of MC-4/5 flight data and simulation model turn rate vs. normalized actuator deflection.	112
8.3	Comparison of MC-4/5 flight data and simulation model steady-state flight characteristics using in-canopy bleed air actuators including: (a) airspeed, (b) descent rate, and (c) glide ratio.	113
8.4	Comparison of MC-4/5 in-canopy actuator step response during flight with in-canopy actuator dynamic model.	116

8.5	MC-4/5 modified turn rate response using in-canopy actuators.	118
8.6	MC-4/5 turn rate mapping using in-canopy actuators.	119
8.7	MC-4/5 spoiler configuration (front view) with (a) minimum and (b) maximum symmetric deflection, δ_s , for equivalent asymmetric deflection, δ_a	120
8.8	Lateral and longitudinal control mapping for the MC-4/5 system using in-canopy actuators.	122
8.9	Simulated landing dispersion of MC-4/5 system using in-canopy actuators for (left) lateral only control and (right) combined lateral and longitudinal control.	125
8.10	MC-4/5 landing accuracy comparison between lateral only and combined lateral and longitudinal control vs. turbulence for different values of mean wind.	126
8.11	Vehicle trajectory relative to inertial frame during MC-4/5 fully autonomous test flight using in-canopy actuators.	128
8.12	Estimated north and east wind components during MC-4/5 autonomous flight.	129
8.13	Commanded and estimated vehicle heading rate during MC-4/5 fully autonomous test flight.	129

SUMMARY

Autonomously guided airdrop systems have revolutionized the notion of aerial delivery by significantly improving airborne cargo landing accuracy and precision. This improvement comes in large part due to the application of steerable ram-air parafoil canopies and sophisticated guidance, navigation, and control algorithms providing the unique capability of such systems to penetrate atmospheric winds and thus maintain close proximity to the target area throughout descent and landing. However, the act of consistently delivering such cargo with pinpoint accuracy and precision is extremely difficult. Limited sensing capability and available control channels combined with variable atmospheric conditions represent some of the biggest challenges airdrop system designers have faced for decades. Furthermore, a growing need exists for improved airdrop system performance where hyper-accurate landing capability is required to ensure continued mission success.

This dissertation explored the use of upper surface bleed air spoilers for control of autonomously guided parafoil and payload aircraft. Upper surface bleed air spoilers consist of several spanwise slits in the upper surface of the parafoil canopy that, when opened, create a virtual spoiler by releasing pressurized air from within the canopy cell. Much like conventional aircraft spoilers, opening of these spanwise slits creates a disturbance in the airflow over the parafoil wing resulting in significant changes in lateral and longitudinal vehicle dynamics. In particular, estimation of the steady-state vehicle flight characteristics in response to different asymmetric and symmetric spoiler openings were determined for two different flight test vehicles. Additionally, improvements in autonomous landing accuracy using upper surface spoilers in a combined lateral and longitudinal control scheme were determined both computationally using

a high fidelity computer simulation model of the test vehicle and further validated in actual flight experiments with excellent results. In both simulation and experimental flight tests, the combined lateral and longitudinal control logic leverages the added control authority of the upper surface spoiler control mechanism in order to compensate for errors in approach trajectory and other unknown disturbances resulting in nearly a 50% reduction in median miss distance.

Lastly, a novel in-canopy bleed air actuation system suitable for large-scale parafoil aircraft was designed, fabricated, and flight tested. The in-canopy bleed air actuation system consists of several small, specifically designed wireless winch actuators mounted entirely inside the parafoil canopy. Each in-canopy actuator is capable of opening one or more upper surface canopy spoilers via a unique internal rigging structure. This system demonstrates not only the applicability of bleed air spoiler control for large-scale autonomous parafoil and payload aircraft, but also provides the potential for significant savings in size, weight, and cost of the required actuation hardware for currently fielded systems.

CHAPTER I

INTRODUCTION

Aerial cargo delivery is an attractive option for military and humanitarian personnel operating in remote areas, hostile environments, or otherwise inaccessible locations. However, the act of consistently delivering such cargo with pinpoint accuracy is an extremely difficult task. Limited sensing capability and available control channels combined with variable atmospheric conditions represent some of the biggest challenges airdrop system designers have faced for decades. Despite these inherent challenges, considerable progress has been made in both vehicle design and algorithm development. Expected landing accuracy for autonomously guided airdrop systems using current state of the art technologies has generally converged to within several hundred meters. Although this level of accuracy may be acceptable for certain situations, other mission scenarios including urban or rooftop targets, mountainous terrain, and rapidly changing battlefronts will undoubtedly demand improved payload delivery accuracy and precision. Accordingly, new methodologies and techniques are needed to meet these demands and ensure continued mission success.

1.1 Airdrop Technology Overview

In terms of currently fielded airdrop system technologies, two distinct classifications exist — unguided systems employing one or more round parachutes to slow the descent of the attached payload, and autonomously guided systems utilizing steerable ram air parafoil canopies. Figure 1.1 provides a representative example from each airdrop technology classification. Although use of round parachutes for aerial cargo delivery dates back as early as the first World War [1], such systems are purely drag based with negligible gliding performance in zero wind conditions and no directional steering



(a)

(b)

Figure 1.1: Typical aerial cargo delivery systems using (a) round parachutes [3] and (b) autonomously guided ram air parafoil canopy [4].

capability. As a result, these systems are usually released from altitudes below 2,000 ft in order to maintain accuracy and reduce landing errors due to wind drift [2]. However, low altitude deployments are often impractical in certain situations as it places the aircraft and its crew at increased risk from hostile enemy weapons.

In recent years, two different programs were developed aimed at improving landing accuracy of ballistic (unguided) airdrop systems. In 1997, the Precision Aerial Delivery Systems (PADS) program sponsored by the U.S. Air Force and Army was started in response to high altitude ballistic payload accuracy problems demonstrated during the humanitarian relief effort of Sarajevo from 1993-1995 [5]. Similar inaccuracies observed from high altitude airdrop operations in Afghanistan beginning in late 2001 prompted the reinforcement and acceleration of the PADS program [5]. PADS objectives include the development of a portable, consolidated data processing system enabling mission planning and en-route updates for ballistic payload aircraft. Based on wind and other atmospheric data assimilated from Global Positioning System (GPS) dropsondes, pilot reports, and other sources via satellite communication,

the PADS software automatically determines the optimum Computed Air Release Point (CARP) of the payload in order to maximize landing accuracy. Flight tests using PADS equipment and 26 ft diameter ring-slot parachutes with payloads ranging from 550 lbs up to 2,200 lbs and at altitudes ranging from 18,000 ft to 25,000 ft demonstrated average miss distances from C-130 and C-17 aircraft of 260 m and 308 m, respectively [5]. A significant improvement of 56% (C-130) and 70% (C-17) over current ballistic parachute operations [5]. In contrast to purely unguided round parachute systems, the Affordable Guided Airdrop System (AGAS) program, jointly managed by the U.S. Air Force and Army, was aimed at further improving landing accuracy of ballistic payload systems by incorporating four pneumatic muscle actuators (PMAs) between the system payload and parachute risers [6–8]. Actuation of each PMA subsequently distorts the shape of the round parachute causing the system to move or “slip” horizontally during its descent. Flight tests of the AGAS in 2004 and 2005 demonstrated average miss distances of approximately 211 m using forecast wind data (PADS) and 43 m using a GPS dropsonde released directly over the target area immediately before AGAS deployment [8].

Although accurate payload delivery with round parachutes is certainly possible, the concept of aerial cargo delivery is much more suited for the use of steerable ram air parafoil canopies as seen in Figure 1.2. Invented by Domina Jalbert in 1964 [9,10], the ram air parafoil canopy is essentially an arc anhedral wing comprised of several spanwise “cells” with airfoil shaped cross-section. Sewn entirely from non-rigid, low porosity fabric, the parafoil canopy inflates (pressurizes) shortly after deployment and remains inflated during flight due to the ram air inlet located at the leading edge of each cell. In contrast from purely drag based round parachutes, the ram air parafoil canopy is capable of achieving glide ratios as high as 4:1 with maximum horizontal velocity in excess of 30 mph [11]. Note glide ratio is defined as the ratio of forward velocity relative to the atmosphere over vertical descent (sink) rate. Lateral



Figure 1.2: Firefly 2K parafoil canopy from Airborne Systems [12].

directional steering is achieved via downward deflection of the parafoil canopy trailing edge.

Autonomous flights using ram air parafoil canopies were first performed by Knapp and Barton in the late 1960's in which radio frequency (RF) homing techniques were used to actively steer the canopy toward a beacon transmitter placed at the target location [13]. In this application, the guided parafoil was used as a sounding rocket recovery vehicle with reported accuracies of 1800 ft and 600 ft from altitudes as high as 5120 ft carrying a 150 pound payload [13]. Following advent of GPS in the late 1980's and early 1990's, NASA and the U.S. Army quickly recognized the feedback potential from satellite positioning and began several programs focused on the development of advanced guided parafoil aircraft and sophisticated guidance, navigation, and control (GN&C) algorithms necessary for autonomous landing capability [5, 14–16]. Initially, NASA proposed the use of the guided parafoil system as a recovery vehicle for space-craft re-entry and precision landing with a large number of documented test flights for a wide variety of vehicle sizes and weights. Most notably was the X-38 Crew



Figure 1.3: NASA X38 with $7,500 \text{ ft}^2$ canopy deployed [16].

Return Vehicle (CRV) program where a $7,500 \text{ ft}^2$ parafoil canopy was designed, built, and flight tested with payload weights of both 18,000 lbs and 25,000 lbs [16]. A total of 13 highly instrumented, autonomous flight tests of the parafoil recovery system for the X-38 were completed before the program was terminated in 2003 [16].

Recently, the Joint Precision Airdrop System (JPADS) program between the U.S. Air Force and the Army includes development of several autonomously guided systems categorized into different weight classes ranging from 10 lbs up to 30,000 lbs (potentially up to 42,000 lbs) with target landing accuracy between 50 and 100 m [17,18]. The primary goal of the JPADS program is to provide global, high altitude (up to 25,000 ft) precision airdrop capability for a wide variety of cargo types and weights [18]. Several autonomous systems currently exist within the JPADS program from both government and private organizations and represent the state of the art in guided aerial delivery systems.

1.2 Bleed Air Control of Parafoil Aircraft

Autonomous parafoil and payload systems are typically controlled by asymmetric deflection of the canopy trailing edge left and right brakes providing an effective means lateral steering control [15,19–27]. In contrast with asymmetric brake deflection, symmetric brake deflection predominantly causes a reduction in forward flight speed and descent rate with small changes in system glide ratio until stall [28]. Other methods for achieving lateral steering control include in-flight rigging angle adjustment [29] and lateral weight shift [30]. Although these systems have demonstrated substantial improvement in landing accuracy, their limited number of available control channels makes them highly susceptible to wind gusts and other unknown atmospheric conditions near the target area leading to large errors in landing position.

Unlike round parachutes, guided parafoil systems are capable of penetrating most atmospheric winds in order to maintain close proximity to the target area throughout its descent. As a result, a significant portion of flight time is spent “loitering” upwind of the target area before beginning its final approach for landing. During this time in loiter, the onboard GN&C algorithm is responsible for computing estimates of the atmospheric wind field and planning an appropriate approach path necessary to intersect the intended target. Figure 1.4 provides a graphical illustration of the typical flight path for autonomously guided parafoil aircraft. Note that the decision to leave loiter and begin final approach toward the target is extremely critical. Given the close proximity of the parafoil system to the ground during final approach, minimal reserve exists within the planned trajectory to account for wind gusts or other unexpected conditions near the target. Wind shears, defined as abrupt changes in wind speed and direction with changing altitude, are often found at altitudes consistent with final approach initiation and can have devastating consequences for autonomously guided systems. For example, if the winds aloft are consistent in both speed and direction but dissipate substantially at ground level, the previously computed approach trajectory

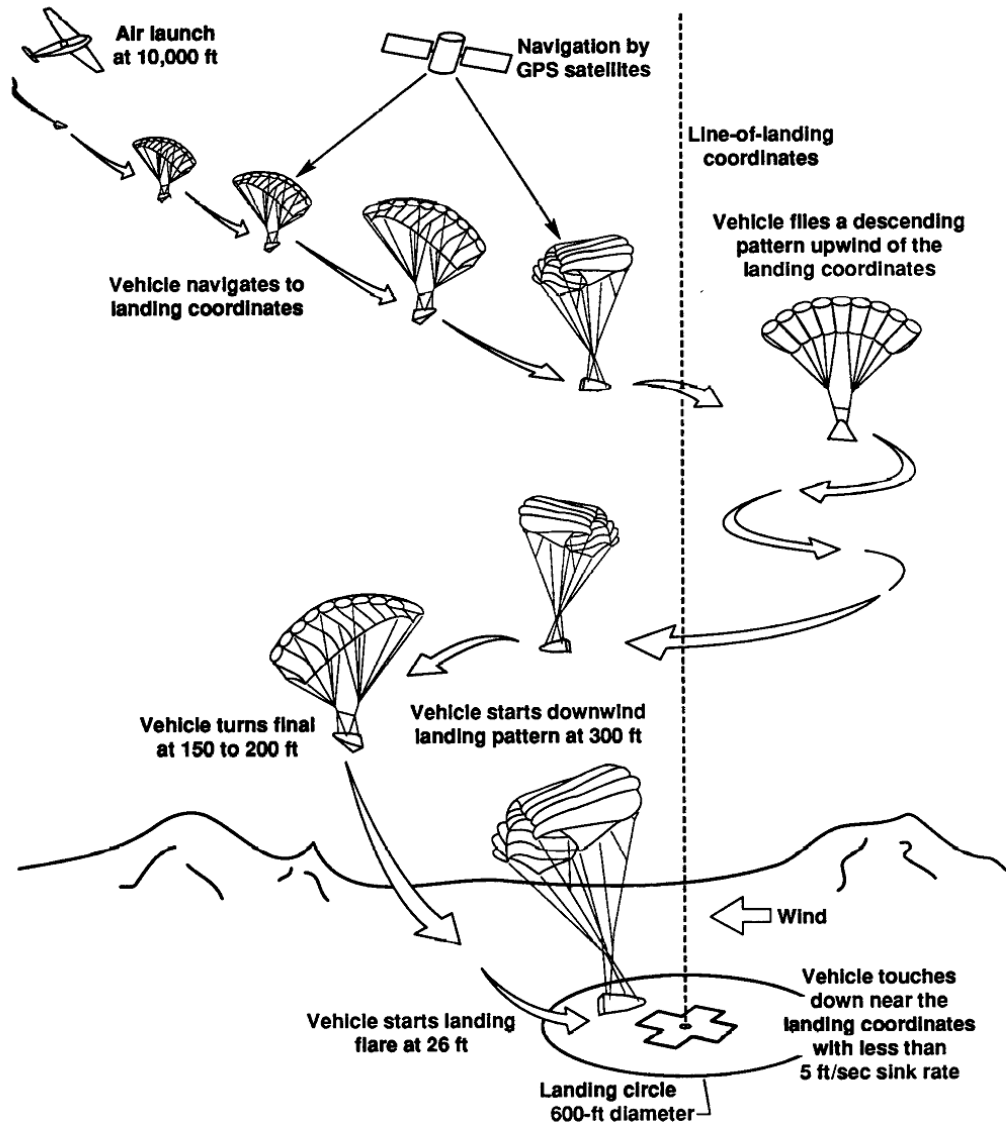


Figure 1.4: Typical guided parafoil aircraft flight plan [14].

will inevitably overshoot the intended target.

In recent years, several researchers have demonstrated that adding longitudinal control or the ability to directly alter the parafoil glide ratio during flight is a very effective means for reducing impact point errors and greatly improving landing accuracy [28,31–34]. Several mechanisms capable of effective glide slope control have been identified including symmetric brake deflection for airspeed control [31], in-flight adjustment of the canopy incidence angle [32,33], and actuation of upper surface bleed

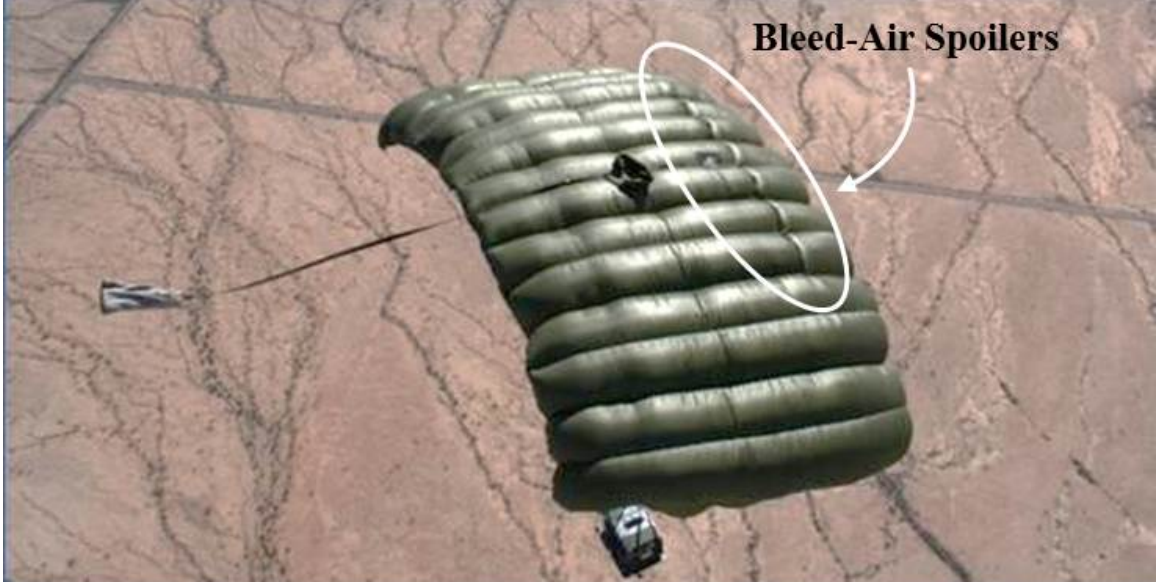


Figure 1.5: Upper surface canopy spoilers during test flight of 100 ft² canopy. Image courtesy of the US Army Natick Soldier Research, Development, and Engineering Center (NSRDEC).

air spoilers [28, 35]. This latter mechanism is the subject of the current work and consists of several spanwise slits in the upper surface of the parafoil canopy that, when opened, create a virtual spoiler by releasing pressurized air from within the canopy cell. Much like conventional aircraft, opening of these spanwise slits creates a disturbance in the airflow over the parafoil wing resulting in a localized perturbation of the associated aerodynamic forces. Although conventional aircraft spoilers are designed as retractable flaps extending from the upper surface of the wing, the concept of upper surface canopy spoilers makes use of vented ram air from within the canopy itself to create a virtual spoiler. When the slit is not actuated, the spanwise tension and internal pressure from within the canopy is sufficient to keep the slit closed. Figure 1.5 shows the upper surface bleed air spoiler mechanism implemented on a 100 ft² canopy in flight.

Gavrilovski et al. have shown that upper surface canopy spoilers provide an effective means for lateral control of parafoils [28]. Opening or actuation of canopy spoilers on one side of the canopy spanwise centerline produces a moment about the

vertical axis of the vehicle which can be used to steer the system to some intended target during its descent. However, the real advantage of the upper surface canopy spoiler mechanism is its ability to clearly and consistently alter the parafoil glide ratio during flight. Using a small scale, remotely piloted test vehicle equipped with a 2.7 m^2 elliptical planform parafoil canopy, Graviloski et al. also demonstrated continuously varying changes in glide ratio from a nominal value of 3.8 to nearly a 70% reduction at just over 1.2 [28]. Additionally, given the relatively small area of the upper canopy surface affected during opening of these spanwise slits, upper surface canopy spoilers require significantly less actuation force compared with that needed to deform large portions of the canopy trailing edge for conventional systems. As a result, substantial actuator size, weight, and cost savings are possible using bleed air spoilers for control.

It is clear that upper surface bleed air spoilers are an attractive control mechanism for parafoil and payload aircraft for several reasons. However, little work exists to optimize the design and construction of the actuation mechanism itself. Furthermore, combined lateral and longitudinal guidance and control algorithms exist for such mechanisms as symmetric brake deflection and variable canopy incidence angle control but none exist specifically aimed at leveraging the unique control authority of upper surface canopy spoilers for improved autonomous landing capability. It is precisely this application that motivates the current research.

1.3 Contributions of the Thesis

The primary objective of this thesis is concisely stated as improving current autonomous airdrop system performance through the use of advanced control mechanisms and software. Although such an objective is common amongst nearly all participating organizations within the autonomous airdrop community, this particular endeavor is scoped to focus specifically on the use of upper surface canopy spoilers for autonomous control of parafoil and payload aircraft and the mitigation of impact

point errors due to variable atmospheric conditions and other outside disturbances. Three separate research areas or “aims” have been identified to guide the current research effort and facilitate the satisfactory completion of the primary objective. These three specific aims are stated below with detailed information and results provided in subsequent chapters.

1. Lateral Control of Autonomous Parafoil and Payload Aircraft Using Upper Surface Canopy Spoilers.
2. Combined Lateral and Longitudinal Control of Autonomous Parafoil and Payload Aircraft Using Upper Surface Canopy Spoilers.
3. On-Canopy Control of Autonomous Parafoil and Payload Aircraft Using Upper Surface Canopy Spoilers.

In order to satisfy the above mentioned objective, a combined simulation and experimental solution methodology is used including development of sophisticated computer models and custom flight test vehicles and related hardware. All simulation efforts employ a specialized six degree of freedom rigid-body dynamic model with aerodynamic and control input parameters tuned to match flight test data. Autonomous guidance and control logic is also developed and integrated within the simulation environment to evaluate flight performance and expected landing accuracy. Lastly, all simulation results are validated through autonomous flight testing in a variety of realistic atmospheric conditions.

1.4 Thesis Outline

A brief description for each of the nine chapters contained within this these is presented below.

- **Chapter 1: Introduction.** A review of both past and present efforts in guided aerial delivery systems is presented. Additionally, details specific to the upper

surface canopy spoiler mechanism are discussed as well as the contribution of the current work.

- **Chapter 2: Flight Dynamic Model.** Equations of motion for the 6 degree of freedom parafoil and payload system model are developed. Sensor and atmospheric wind models are also given.
- **Chapter 3: Smale Scale Test Vehicle Platform.** The small scale parafoil and payload test vehicle used during flight tests is described. Results from several system identification flight are also presented with an emphasis on steady-state lateral and longitudinal control response using upper surface canopy spoilers.
- **Chapter 4: Guidance, Navigation, and Control Algorithm.** The guidance, navigation, and control algorithm used in both simulation and autonomous flight tests is developed. Specific details details for both lateral and longitudinal control techniques are presented as well as an example simulated autonomous trajectory.
- **Chapter 5: Autonomous Landing Performance.** Autonomous landing accuracy of the test vehicle using upper surface canopy spoilers exclusively for control is investigated in both simulation and flight experiments. Results show that nearly a 50% reduction in median miss distance is achieved when using combined lateral and longitudinal control logic with excellent agreement between simulated and experimental data.
- **Chapter 6: In-Canopy Bleed Air Actuation System.** Development of a novel in-canopy bleed air actuation system for parafoil and payload aircraft is presented. In this system, all bleed air actuators are mounted entirely within the parafoil canopy itself. Actuator mounting and rigging strategies are also

discussed as well as specific details of the in-canopy hardware.

- **Chapter 7: Flight Testing of In-Canopy Hardware.** Results from several flight tests with a large scale parafoil aircraft using the in-canopy bleed air actuation system are presented, including spoiler actuation force measurements and steady-state lateral and longitudinal control response to various combinations of upper surface spoiler openings.
- **Chapter 8: In-Canopy Autonomous Landing Performance.** Autonomous landing accuracy of a large scale parafoil and payload aircraft is investigated in both simulation and experimental flight tests. Aerodynamic and control input parameters within the simulation framework are updated to match that observed during flight tests of the in-canopy hardware. Aggregate landing accuracy statistics in a variety of atmospheric conditions and numerous trade studies demonstrate the effectiveness and potential for improved autonomous system performance using the in-canopy actuation system.
- **Chapter 9: Conclusions and Future Work.** Concluding remarks regarding use of upper surface canopy spoilers in autonomous parafoil and payload aircraft are presented. Additionally, suggested areas for future work are proposed.

CHAPTER II

FLIGHT DYNAMIC MODEL

For parafoil and payload aircraft, a large collection of work exists in literature describing several different models intended to capture various aspects of vehicle motion. Ranging in fidelity from reduced order models with 3 or 4 degrees of freedom to those with additional dynamics including relative motion between the parafoil canopy and payload, each model is designed with a specific purpose and level of detail. In the current work, a 6 degree of freedom (DOF) model encompassing a full set of rigid body states is used to accurately predict vehicle motion in order to evaluate the performance of specialized lateral and longitudinal guidance and control algorithms. This particular model structure has been used extensively in various flight dynamic modeling applications, including parafoil and payload aircraft, with good results. However, it must be noted that parafoil aircraft are inherently flexible systems with significantly more degrees of freedom than that associated with simple rigid body motion. Accordingly, the 6 DOF model presented here is only valid for those flight regimes in which the parafoil aircraft is flying under relatively mild lateral and longitudinal motion and cannot be expected to accurately predict vehicle performance during highly dynamic maneuvering.

This chapter provides a general overview of the various mathematical nomenclature and conventions used throughout this thesis followed by derivation of the 6 DOF nonlinear equations of motion governing parafoil and payload system motion. Additional details regarding the sensor model used for synthetic feedback signal generation and the atmospheric wind and turbulence models for simulating realistic atmospheric disturbances during flight are also provided.

2.1 Mathematical Nomenclature and Convention

The mathematical nomenclature and specific conventions used throughout this dissertation are provided here for reference to the reader. All position vectors are written according to the following form $\vec{r}_{\alpha \rightarrow \beta}$ denoting the vector extending from any arbitrary point α to a second arbitrary point β . Velocity and acceleration vectors are similarly written as $\vec{v}_{\alpha/F}$ and $\vec{a}_{\alpha/F}$ denoting the velocity and acceleration, respectively, of an arbitrary point α with respect to reference frame F . In terms of angular quantities, the symbols $\vec{\omega}_{F/G}$ and $\vec{\alpha}_{F/G}$ are used to represent the angular velocity and angular acceleration of reference frame F with respect to frame G , respectively. Unit vectors extending along the x , y , and z axes in frame F are written as \vec{I}_F , \vec{J}_F , and \vec{K}_F , respectively.

By convention, all vector quantities are enclosed within curly brackets $\{ \}$, while matrices are represented with square brackets $[]$. Additionally, the transformation matrix from reference frame F to reference frame G is written as $[T_{FG}]$ where the second subscript denotes the resulting reference frame following transformation. Lastly, the skew symmetric cross product operator $\mathbb{S}[\cdot]$ is used to express the cross product of two vectors as a single matrix-vector multiplication as shown below for two arbitrary vectors \vec{a} and \vec{b} expressed in frame A .

$$\vec{a} = x_a \vec{I}_A + y_a \vec{J}_A + z_a \vec{K}_A, \quad \vec{b} = x_b \vec{I}_A + y_b \vec{J}_A + z_b \vec{K}_A \quad (2.1)$$

$$\vec{a} \times \vec{b} \implies \mathbb{S}_A[\vec{a}] \begin{Bmatrix} x_b \\ y_b \\ z_b \end{Bmatrix} = \begin{bmatrix} 0 & -z_a & y_a \\ z_a & 0 & -x_a \\ -y_a & x_a & 0 \end{bmatrix} \begin{Bmatrix} x_b \\ y_b \\ z_b \end{Bmatrix} \quad (2.2)$$

2.2 Equations of Motion

Figure 2.1 shows a schematic drawing of a parafoil and payload system. Note the parafoil canopy and all rigging lines connecting the payload to the canopy are considered to be a fixed shape and modeled as a single rigid body with 6 degrees of freedom — three inertial position components of the combined system mass center, denoted x, y, z , and three Euler orientation angles, denoted ϕ, θ , and ψ .

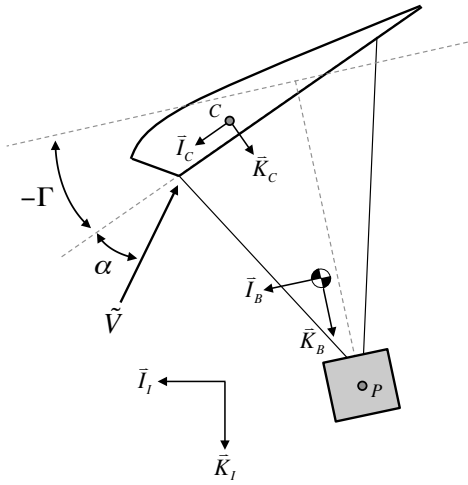


Figure 2.1: Parafoil and payload system dynamic model.

2.2.1 Kinematics

Translational velocity of the parafoil and payload mass center with respect to the inertial frame, denoted $\vec{v}_{cg/I}$, is equivalently represented using both inertial frame and body frame coordinates as shown in equation (2.3). Note the subscripts (I) and (B) represent the inertial and body reference frames, respectively.

$$\vec{v}_{cg/I} = \dot{x}\vec{I}_I + \dot{y}\vec{J}_I + \dot{z}\vec{K}_I = u\vec{I}_B + v\vec{J}_B + w\vec{K}_B \quad (2.3)$$

Accordingly, the translational kinematic equations of motion are shown below in equation (2.4). Note the use of shorthand notation for trigonometric functions:

$s_\alpha \equiv \sin(\alpha)$, $c_\alpha \equiv \cos(\alpha)$, and $t_\alpha \equiv \tan(\alpha)$. Also, the matrix $[T_{IB}]$ represents the transformation matrix from the inertial reference frame to the body reference frame according to the standard aerospace (body-fixed, 3-2-1) rotation sequence.

$$\begin{Bmatrix} \dot{x} \\ \dot{y} \\ \dot{z} \end{Bmatrix} = \begin{bmatrix} c_\theta c_\psi & c_\theta s_\psi & -s_\theta \\ s_\phi s_\theta c_\psi - c_\phi s_\psi & s_\phi s_\theta s_\psi + c_\phi c_\psi & s_\phi c_\theta \\ c_\phi s_\theta c_\psi + s_\phi s_\psi & c_\phi s_\theta s_\psi - s_\phi c_\psi & c_\phi c_\theta \end{bmatrix} \begin{Bmatrix} u \\ v \\ w \end{Bmatrix} = [T_{IB}]^T \begin{Bmatrix} u \\ v \\ w \end{Bmatrix} \quad (2.4)$$

Angular velocity of the combined parafoil and payload system with respect to the inertial frame, denoted $\vec{\omega}_{B/I}$, is similarly written using body frame components p , q , and r as shown in equation (2.5).

$$\vec{\omega}_{B/I} = p\vec{I}_B + q\vec{J}_B + r\vec{K}_B \quad (2.5)$$

The kinematic relationship between the body frame angular velocity components and each Euler angle time derivative forms the rotational kinematic equations of motion given in equation (2.6).

$$\begin{Bmatrix} \dot{\phi} \\ \dot{\theta} \\ \dot{\psi} \end{Bmatrix} = \begin{bmatrix} 1 & s_\phi t_\theta & c_\phi t_\theta \\ 0 & c_\phi & -s_\theta \\ 0 & s_\phi/c_\theta & c_\phi/c_\theta \end{bmatrix} \begin{Bmatrix} p \\ q \\ r \end{Bmatrix} \quad (2.6)$$

2.2.2 Dynamics

The dynamic equations of motion for the combined parafoil and payload system are formed by summing all forces and moments, respectively, about the system mass center and equating to the time derivative of both linear and angular momentum as

shown in equations (2.7) and (2.8) where m represents the total mass of the system, and $[I_B]$ is the vehicle inertia matrix about its mass center.

$$\begin{Bmatrix} \dot{u} \\ \dot{v} \\ \dot{w} \end{Bmatrix} + \mathbb{S}_B[\vec{\omega}_{B/I}] \begin{Bmatrix} u \\ v \\ w \end{Bmatrix} = \frac{1}{m} \begin{Bmatrix} X \\ Y \\ Z \end{Bmatrix} \quad (2.7)$$

$$[I_B] \begin{Bmatrix} \dot{p} \\ \dot{q} \\ \dot{r} \end{Bmatrix} + \mathbb{S}_B[\vec{\omega}_{B/I}] [I_B] \begin{Bmatrix} p \\ q \\ r \end{Bmatrix} = \begin{Bmatrix} L \\ M \\ N \end{Bmatrix} \quad (2.8)$$

Note the vector components X , Y , and Z , and L , M , and N , represent the total applied forces and moments, respectively, acting on the system. Expansion of both the total applied forces and moments are shown in equations (2.9) and (2.10) where subscripts denote forces and moments due to system weight ($_W$), canopy aerodynamics ($_{CA}$), payload aerodynamics ($_{PA}$), and apparent mass ($_{AM}$). Note control forces and moments are realized via changes in the total canopy aerodynamic forces and moments and are thus not explicitly included here.

$$\begin{Bmatrix} X \\ Y \\ Z \end{Bmatrix} = \begin{Bmatrix} X_W \\ Y_W \\ Z_W \end{Bmatrix} + \begin{Bmatrix} X_{CA} \\ Y_{CA} \\ Z_{CA} \end{Bmatrix} + \begin{Bmatrix} X_{PA} \\ Y_{PA} \\ Z_{PA} \end{Bmatrix} + \begin{Bmatrix} X_{AM} \\ Y_{AM} \\ Z_{AM} \end{Bmatrix} \quad (2.9)$$

$$\begin{aligned} \begin{Bmatrix} L \\ M \\ N \end{Bmatrix} &= \begin{Bmatrix} L_{CA} \\ L_{CA} \\ Z_{CA} \end{Bmatrix} + \mathbb{S}_B[\vec{r}_{cg \rightarrow C}] \begin{Bmatrix} X_{CA} \\ Y_{CA} \\ Z_{CA} \end{Bmatrix} + \mathbb{S}_B[\vec{r}_{cg \rightarrow P}] \begin{Bmatrix} X_{PA} \\ Y_{PA} \\ Z_{PA} \end{Bmatrix} \\ &\quad + \begin{Bmatrix} L_{AM} \\ M_{AM} \\ N_{AM} \end{Bmatrix} + \mathbb{S}_B[\vec{r}_{cg \rightarrow M}] \begin{Bmatrix} X_{AM} \\ Y_{AM} \\ Z_{AM} \end{Bmatrix} \end{aligned} \quad (2.10)$$

The weight force acting at the combined parafoil and payload system mass center is computed according to equation (2.11).

$$\begin{Bmatrix} X_W \\ Y_W \\ Z_W \end{Bmatrix} = mg \begin{Bmatrix} -s_\theta \\ s_\phi c_\theta \\ c_\phi c_\theta \end{Bmatrix} \quad (2.11)$$

All canopy aerodynamic forces and moments are computed at a single point C shown in Figure 2.1 representing the mean canopy aerodynamic center of pressure. Accordingly, velocity of point C relative to the atmosphere (aerodynamic velocity) is shown in equation (2.12) with components \tilde{u}_C , \tilde{v}_C , and \tilde{w}_C expressed in the canopy reference frame.

$$\begin{Bmatrix} \tilde{u}_C \\ \tilde{v}_C \\ \tilde{w}_C \end{Bmatrix} = [T_{BC}] \left(\begin{Bmatrix} u \\ v \\ w \end{Bmatrix} - \mathbb{S}_B[\vec{r}_{cg \rightarrow C}] \begin{Bmatrix} p \\ q \\ r \end{Bmatrix} - [T_{IB}] \begin{Bmatrix} V_{W,x} \\ V_{W,y} \\ V_{W,z} \end{Bmatrix} \right) \quad (2.12)$$

Transformation between the vehicle body frame (B) and canopy frame (C) is represented as the constant matrix $[T_{BC}]$ consisting of a single rotation about the \vec{J}_B

axis through the canopy incidence angle Γ . Additionally, the vector components $V_{W,x}$, $V_{W,y}$, and $V_{W,z}$ represent the atmospheric wind velocities relative to the inertial frame along the \vec{I}_I , \vec{J}_I , and \vec{K}_I directions, respectively. Other aerodynamic quantities including total airspeed \tilde{V} , angle of attack α , and sideslip angle β are subsequently calculated according to equations (2.13) – (2.15).

$$\tilde{V} = \sqrt{\tilde{u}_C^2 + \tilde{v}_C^2 + \tilde{w}_C^2} \quad (2.13)$$

$$\alpha = \tan^{-1}(\tilde{w}_C/\tilde{u}_C) \quad (2.14)$$

$$\beta = \sin^{-1}(\tilde{v}_C/\tilde{V}) \quad (2.15)$$

Canopy aerodynamic forces are determined by lift, drag, and side force coefficients, denoted C_L , C_D , and $C_{Y\beta}$, respectively, where lift and drag coefficients are dependent on both canopy angle of attack and symmetric actuation (opening) of the upper surface bleed air spoilers, denoted δs . Note δs is simply computed as the average opening between the left and right spoilers δl and δr , respectively, as shown in equation (2.16). Exact forms of the canopy lift and drag coefficients are shown in equations (2.17) and (2.18).

$$\delta s = 0.5 (\delta l + \delta r) \quad (2.16)$$

$$C_L = C_{L0} + C_{L\alpha}\alpha + C_{L\alpha 3}\alpha^3 + C_{L0\delta s}\delta s \quad (2.17)$$

$$C_D = C_{D0} + C_{D\alpha 2}\alpha^2 + C_{D0\delta s}\delta s \quad (2.18)$$

The total aerodynamic forces expressed in the body frame are computed according to equation (2.19). Note ρ represents the atmospheric density and S_C is the total canopy surface area.

$$\begin{Bmatrix} X_{CA} \\ Y_{CA} \\ Z_{CA} \end{Bmatrix} = \frac{1}{2} \rho \tilde{V}^2 S_C [T_{BC}]^T \begin{bmatrix} c_\alpha & 0 & -s_\alpha \\ 0 & 1 & 0 \\ s_\alpha & 0 & c_\alpha \end{bmatrix} \begin{Bmatrix} -C_D \\ C_{Y\beta}\beta \\ -C_L \end{Bmatrix} \quad (2.19)$$

In terms of payload aerodynamic forces, the velocity of point P (refer Figure 2.1) with respect to the atmosphere is given by equation (2.20)

$$\begin{Bmatrix} \tilde{u}_P \\ \tilde{v}_P \\ \tilde{w}_P \end{Bmatrix} = \begin{Bmatrix} u \\ v \\ w \end{Bmatrix} - \mathbb{S}_B[\vec{r}_{cg \rightarrow P}] \begin{Bmatrix} p \\ q \\ r \end{Bmatrix} - [T_{IB}] \begin{Bmatrix} V_{W,x} \\ V_{W,y} \\ V_{W,z} \end{Bmatrix} \quad (2.20)$$

where orientation of the payload frame axes are assumed collinear with the body frame axes. Accordingly, all aerodynamic force acting on the payload consist entirely of profile drag given by Eq. 2.21 where $C_{D,p}$ is the payload drag coefficient.

$$\begin{Bmatrix} X_{PA} \\ Y_{PA} \\ Z_{PA} \end{Bmatrix} = \frac{1}{2} \rho S_p C_{D,p} \sqrt{\tilde{u}_P^2 + \tilde{v}_P^2 + \tilde{w}_P^2} \begin{Bmatrix} \tilde{u}_P \\ \tilde{v}_P \\ \tilde{w}_P \end{Bmatrix} \quad (2.21)$$

Steady aerodynamic moments are computed as cross products between the distance vectors extending from the combined system mass center to both the canopy and payload center of pressure, points C and P , respectively, and the aerodynamic forces shown above. Additionally, unsteady canopy aerodynamic moments are given by equation (2.22)

$$\begin{Bmatrix} L_{CA} \\ M_{CA} \\ N_{CA} \end{Bmatrix} = \frac{1}{2} \rho \tilde{V}^2 S_C [T_{BC}]^T \begin{Bmatrix} b C_l \\ c C_m \\ b C_n \end{Bmatrix} \quad (2.22)$$

where b and c denote dimensions of the canopy span and chord, respectively. Note canopy roll, pitch, and yaw moment coefficients C_l , C_m , and C_n are dependent on components of the vehicle angular velocity expressed in the canopy frame (\tilde{p} , \tilde{q} , and \tilde{r})

with additional terms necessary to model the turning moments created from asymmetric opening of the upper surface spoilers, denoted δa , where $\delta a = \delta r - \delta l$.

$$\vec{\omega}_{B/I} = \tilde{p}\vec{I}_C + \tilde{q}\vec{J}_C + \tilde{r}\vec{K}_C \quad (2.23)$$

$$C_l = \frac{b}{2\tilde{V}} \left(C_{lp}\tilde{p} + C_{lr}\tilde{r} \right) + C_{l\delta a}\delta a \quad (2.24)$$

$$C_m = \frac{c}{2\tilde{V}} C_{mq}\tilde{q} \quad (2.25)$$

$$C_n = \frac{b}{2\tilde{V}} \left(C_{np}\tilde{p} + C_{nr}\tilde{r} \right) + C_{n\beta}\beta + C_{n\delta a}\delta a \quad (2.26)$$

Parafoils with small mass to volume ratios can experience significant forces and moments from accelerating fluid [36,37]. These added forces and moments are termed apparent mass effects and can substantially complicate the dynamic equations of motion. However, it is possible to obtain a good approximation of these effects with only two terms. The approximate forms used for the apparent mass forces and moments are given in equations (2.27) and (2.28), respectively. Note that only unsteady terms are included in each expression. All steady apparent mass effects are assumed to be included within the canopy steady aerodynamic forces and moments. Also, atmospheric winds are assumed to vary slowly such that the time derivatives of each wind component shown in equation (2.27) are neglected. Lastly, the apparent mass center is assumed to be coincident with the canopy center of pressure for simplicity. Parametric approximations given by Lissaman and Brown [37] are used to determine the apparent mass and inertia coefficients A , B , C , P , Q , and R shown in equations (2.29) and (2.30) where the diagonal matrices $[I_{AM}]$ and $[I_{AI}]$ are relative to the canopy frame and must be transformed into the body frame.

$$\begin{Bmatrix} X_{AM} \\ Y_{AM} \\ Z_{AM} \end{Bmatrix} = -[I_{AM}]' \begin{Bmatrix} \dot{u} \\ \dot{v} \\ \dot{w} \end{Bmatrix} - \mathbb{S}_B[\vec{r}_{cg \rightarrow C}] \begin{Bmatrix} \dot{p} \\ \dot{q} \\ \dot{r} \end{Bmatrix} - [T_{IB}] \begin{Bmatrix} \dot{V}_{W,x} \\ \dot{V}_{W,y} \\ \dot{V}_{W,z} \end{Bmatrix} \quad (2.27)$$

$$\begin{Bmatrix} L_{AM} \\ M_{AM} \\ N_{AM} \end{Bmatrix} = -[I_{AI}]' \begin{Bmatrix} \dot{p} \\ \dot{q} \\ \dot{r} \end{Bmatrix} \quad (2.28)$$

$$[I_{AM}]' = [T_{BC}]^T [I_{AM}] [T_{BC}], \quad [I_{AM}] = \begin{bmatrix} A & 0 & 0 \\ 0 & B & 0 \\ 0 & 0 & C \end{bmatrix} \quad (2.29)$$

$$[I_{AI}]' = [T_{BC}]^T [I_{AI}] [T_{BC}], \quad [I_{AI}] = \begin{bmatrix} P & 0 & 0 \\ 0 & Q & 0 \\ 0 & 0 & R \end{bmatrix} \quad (2.30)$$

By substituting all of the applied forces and moments defined previously in equations (2.11), (2.19), (2.21), (2.22), (2.27), and (2.28) into the dynamic equations shown in equations (2.7) and (2.8), the following matrix solution is found

$$\begin{bmatrix} m[I_{3x3}] + [I_{AM}]' & -[I_{AM}]' \mathbb{S}_B[\vec{r}_{cg \rightarrow C}] \\ \mathbb{S}_B[\vec{r}_{cg \rightarrow C}][I_{AM}]' & [I_B] + [I_{AI}]' - \mathbb{S}_B[\vec{r}_{cg \rightarrow C}][I_{AM}]' \mathbb{S}_B[\vec{r}_{cg \rightarrow C}] \end{bmatrix} \begin{Bmatrix} \dot{u} \\ \dot{v} \\ \dot{w} \\ \dots \\ \dot{p} \\ \dot{q} \\ \dot{r} \end{Bmatrix} = \begin{Bmatrix} B_1 \\ \dots \\ B_2 \end{Bmatrix} \quad (2.31)$$

where

$$B_1 = -m \mathbb{S}_B[\vec{\omega}_{B/I}] \begin{Bmatrix} u \\ v \\ w \end{Bmatrix} + \begin{Bmatrix} X_W \\ Y_W \\ Z_W \end{Bmatrix} + \begin{Bmatrix} X_{CA} \\ Y_{CA} \\ Z_{CA} \end{Bmatrix} + \begin{Bmatrix} X_{PA} \\ Y_{PA} \\ Z_{PA} \end{Bmatrix} \quad (2.32)$$

$$\begin{aligned} B_2 = -\mathbb{S}_B[\vec{\omega}_{B/I}][I_B] \begin{Bmatrix} p \\ q \\ r \end{Bmatrix} + \begin{Bmatrix} L_{CA} \\ M_{CA} \\ N_{CA} \end{Bmatrix} \\ + \mathbb{S}_B[\vec{r}_{cg \rightarrow C}] \begin{Bmatrix} X_{CA} \\ Y_{CA} \\ Z_{CA} \end{Bmatrix} + \mathbb{S}_B[\vec{r}_{cg \rightarrow P}] \begin{Bmatrix} X_{PA} \\ Y_{PA} \\ Z_{PA} \end{Bmatrix} \end{aligned} \quad (2.33)$$

Equation (2.31) represents a system of six coupled, nonlinear differential equations. The 6-by-6 matrix on the left hand side of Eq. 2.31 is exclusively a function of the combined parafoil and payload system mass and geometrical properties and is assumed constant throughout the entire simulation. As a result, this matrix must only be inverted once at the start of each simulation. Beginning from some known set

of initial conditions, the dynamic system is numerically integrated forward in time using a 4th order Runge-Kutta numerical integration algorithm to obtain a single trajectory [38].

2.3 Sensor Model

Synthetic feedback signals representative of a commercially available GPS receiver are modeled with exponentially correlated Gaussian noise added to the corresponding true state value. Equations (2.34) – (2.36) detail computation of the synthetic sensor data where v_k is the simulated measurement, y_k is the true value, and n_k is the measurement noise.

$$v_k = y_k + n_k \quad (2.34)$$

$$n_k = e^{-\Delta t/\tau_n} n_{k-1} + \xi_k \sqrt{1 - e^{-2\Delta t/\tau_n}} \quad (2.35)$$

$$\xi_k \sim N(0, \sigma_n) \quad (2.36)$$

Table 2.1 presents the sensor error parameters used for all simulations included within this dissertation. Note measurement standard deviations (σ_n) and time constants (τ_n) were chosen to match the expected accuracy for typical commercially available sensors.

Table 2.1: GPS sensor error parameters [39].

	Horizontal Position	Horizontal Velocity	Vertical Position	Vertical Velocity
Standard Deviation, σ_n	2.0 m	0.2 m/s	3.0 m	0.2 m/s
Time Constant, τ_n	20 s	1.0 s	20 s	1.0 s

2.4 Wind Model

The atmospheric wind model used within the parafoil and payload simulation framework is a discrete implementation of the Dryden turbulence spectrum [40–42]. Accordingly, wind gust velocities and angular rates are computed along all three inertial axes by driving discrete filter elements with unit variance, white noise signals, denoted η_i , as shown below.

$$\eta_i = N(0, 1) \quad i \in 1, \dots, 4 \quad (2.37)$$

$$u_g(k+1) = \left(1 - \frac{V}{L_u} \Delta t\right) u_g(k) + \sqrt{2\Delta t \frac{V}{L_u}} \sigma_u \eta_1 \quad (2.38)$$

$$v_g(k+1) = \left(1 - \frac{V}{L_v} \Delta t\right) v_g(k) + \sqrt{2\Delta t \frac{V}{L_v}} \sigma_v \eta_2 \quad (2.39)$$

$$w_g(k+1) = \left(1 - \frac{V}{L_w} \Delta t\right) w_g(k) + \sqrt{2\Delta t \frac{V}{L_w}} \sigma_w \eta_3 \quad (2.40)$$

$$p_g(k+1) = \left(1 - \frac{2.6}{\sqrt{2L_w b}} \Delta t\right) p_g(k) + \sqrt{2\Delta t \frac{2.6}{\sqrt{2L_w b}}} \frac{1.9}{\sqrt{2L_w b}} \sigma_w \eta_4 \quad (2.41)$$

$$q_g(k+1) = \left(1 - \frac{\pi V}{4b} \Delta t\right) q_g(k) + \frac{\pi}{4b} (w_g(k+1) - w_g(k)) \quad (2.42)$$

$$r_g(k+1) = \left(1 - \frac{\pi V}{3b} \Delta t\right) r_g(k) + \frac{\pi}{3b} (v_g(k+1) - v_g(k)) \quad (2.43)$$

Note u_g , v_g , and w_g represent the wind gust velocity components along the \vec{I}_I , \vec{J}_I , and \vec{K}_I axes, respectively. Similarly, p_g , q_g , and r_g represent the wind gust angular velocity components along the same directions. Additionally, vehicle airspeed and wing span are denoted by V and b , respectively.

Turbulence length scales and intensities are set according to the MIL-HDBK-1797 handbook [40]. Note at high altitudes, the length scales are longer resulting in more slowly varying gust components as opposed to altitudes nearest ground level where the wind gusts are allowed to vary more rapidly. Exact forms for each are shown below in equations (2.44) and (2.45) where h is measured in feet.

$$L_w = h, \quad L_u = L_v = \frac{h}{(0.177 + 0.000823h)^{1.2}} \quad (2.44)$$

$$\sigma_u = \sigma_v = \frac{\sigma_w}{(0.177 + 0.000823h)^{0.4}} \quad (2.45)$$

The only input parameters needed for the atmospheric wind model include the standard deviation of the vertical wind gust component σ_w to define the expected turbulence level and the mean wind speed and direction with changing altitude. Example wind profiles generated using this model are shown in subsequent sections.

CHAPTER III

SMALL SCALE TEST VEHICLE PLATFORM

In this chapter, a description of the small scale test vehicle used in flight tests is presented, including a summary of the necessary modifications for converting a typical parafoil canopy with trailing edge brakes to one using upper surface canopy spoilers for control. Additionally, the results from several system identification flights using the small scale test vehicle are presented with an emphasis on steady-state lateral and longitudinal response to various combinations of upper surface spoiler openings. These results are used to construct an accurate mathematical representation of the test vehicle using the dynamic model previously described in Chapter II enabling both refinement of the autonomous control logic necessary for precision landing and simulation of entire autonomous missions from altitude to ground impact.

3.1 Hardware Description

Although most autonomous parafoil and payload aircraft are significantly large in size with payloads weighing several hundred pounds or more, the majority of testing described within this thesis employs the use of a small scale test vehicle capable of being hand-launched and remotely piloted by a single person. The test vehicle, shown in Figure 3.1, consists of an airdrop-style rectangular planform parafoil canopy attached to a small payload. The canopy itself is comprised of 18 individual cells with a total surface area of 0.96 m^2 and an aspect ratio of 2.62. Total flying weight of the vehicle is approximately 4.5 lbs.

Two different parafoil canopies, denoted Canopy 1 and Canopy 2, are shown in Figure 3.1. Each canopy is identical in size, shape, and rigging, and sewn entirely from zero-porosity ripstop nylon fabric. However, the fabric stiffness varies slightly

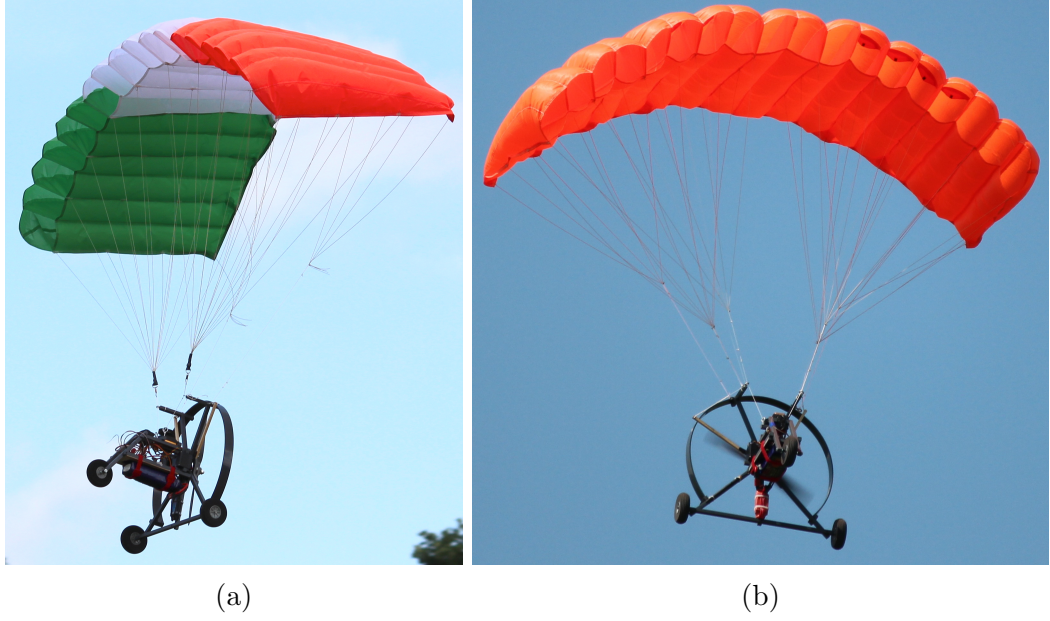


Figure 3.1: Test vehicle in gliding flight shown with (a) Canopy 1 and (b) Canopy 2.

between canopies and even between the three different color sections seen in Canopy 1. For example, the white center section in Canopy 1 is the softest in texture while the orange section (left) and green section (right) are increasingly more rigid and nearly paper-like. Alternatively, Canopy 2 is significantly softer in texture than either section in Canopy 1 and more closely resembles the fabric stiffness expected in typical airdrop parachute construction.

The test vehicle payload also features an electric motor and propeller for use during powered ascent to altitude, an onboard autopilot and sensing suite for executing autonomous guidance algorithms, and three servo actuators for canopy incidence angle (trim) adjustment and steering control. Note the onboard autopilot, shown in Figure 3.2, is equipped with an embedded microprocessor, GPS receiver, barometric altimeter, non-volatile storage for data logging, and a 2.4 GHz wireless transceiver for communicating with a ground station laptop computer during flight. In practice, the test vehicle is hand-launched from ground level and remotely piloted to some desired altitude. Once at altitude, the motor is stopped and the onboard autopilot activated initiating autonomous control throughout descent and landing.

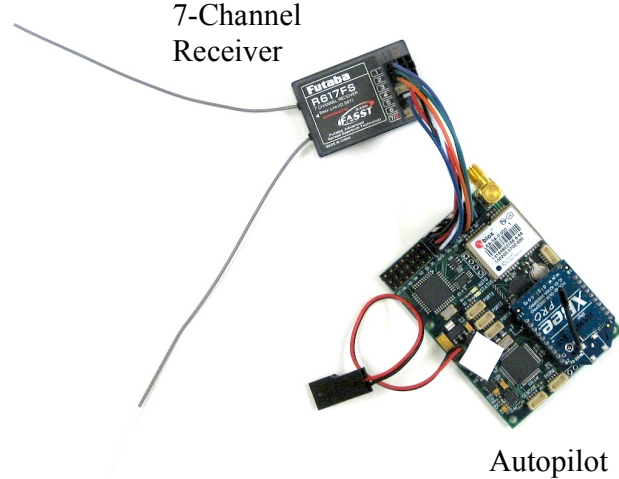


Figure 3.2: Onboard autopilot and sensing suite.

3.2 Canopy Modifications

Conversion from conventional trailing edge brakes to upper surface canopy spoilers involves first introducing a series of spanwise slits in the upper surface of several cells on either side of the canopy centerline. In practice, each slit is actuated by pulling down from a single control line attached at the center of the leading edge side of the upper surface opening that runs down through the bottom surface of the canopy to the payload. As the upper surface slit opens, a stream of high pressure ram air from within the canopy cell is expelled creating a virtual aerodynamic spoiler. When

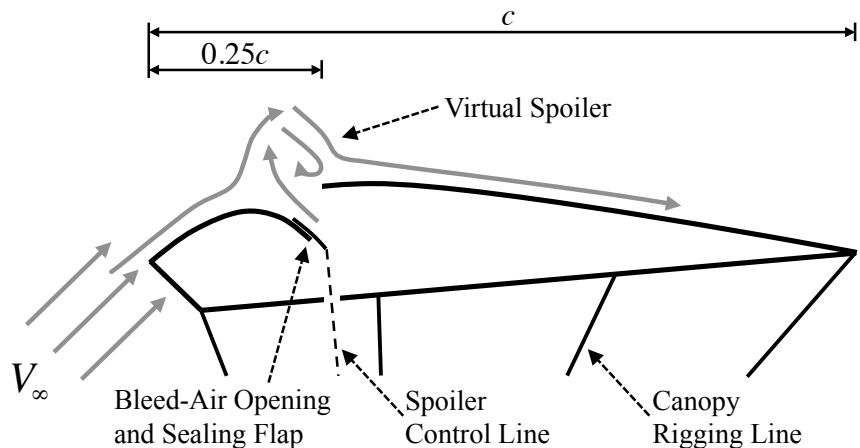


Figure 3.3: Cross-section view of upper surface canopy spoiler control mechanism.

not actuated, the spanwise tension and internal pressure from within the canopy cell is sufficient to force the upper surface spoiler closed preventing any further airflow to the outside. Additionally, a small piece of fabric or sealing flap is added to the actuated edge of the slit to help prevent air leakage when the spoiler is closed. A cross-sectional view of the upper surface canopy spoiler mechanism within a single cell is shown in Figure 3.3. Note the upper surface bleed air opening is located at approximately $0.25c$ back from the leading edge where c represents the mean airfoil chord. Moving the bleed air opening closer to the leading edge of the wing does increase the effectiveness of the spoiler; however, additional complications with keeping the cell properly inflated during flight have been documented when the slits are positioned at distances of $0.15c$ or less from the canopy ram air opening [28].

In total, 8 cells (4 left, 4 right) within the test vehicle canopy are modified to include upper surface spoiler openings. Figure 3.4 provides a front view of the test vehicle canopy with each shaded gray region denoting the relative location of those cells with bleed air openings. Note 4 cells within the canopy center section are left

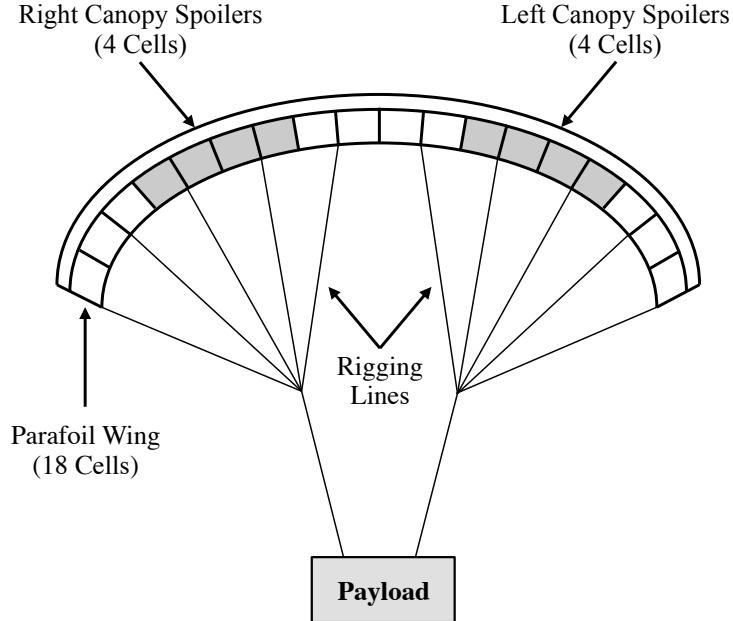


Figure 3.4: Upper surface canopy spoiler control mechanism (front view).

unmodified while two groups of 4 cells each on either side are configured with bleed air openings. This specific configuration was selected in order to balance the expected lateral and longitudinal control authority of the vehicle noting that spoiler openings nearest the canopy center contribute primarily to changes in vehicle airspeed and descent rate while openings nearest the canopy wingtips contribute mostly to changes in turn rate. Although independent control of each individual cell is possible, the 4 cells on either side of the center section are connected together such that only two separate servo actuators are needed for independent opening of the left and right spoilers.

It must be noted that significant work exists in literature regarding bleed air control for conventional aircraft and rigid wing structures. In particular, a wide variety of bleed air flows or jets both normal and tangential to the airfoil surface have been investigated demonstrating significant aerodynamic performance manipulation including complete reattachment of separated flow [43–45]. In the current work, only the upper surface spanwise slit based on the work of Gavrilovski et al. in [28] is considered where its performance is first characterized and later used for mathematical model development and landing accuracy prediction. Although the possibility exists to further improve performance of the upper surface spoiler control mechanism by altering or refining spoiler construction, this work falls outside the scope of this dissertation and is left for future work.

3.3 System Identification

The following sections provide a brief overview of parafoil aircraft system identification as well as the data reduction procedure and results using the small scale test vehicle described previously.

3.3.1 Parafoil and Payload System Identification Overview

In order to quantify the effects of upper surface spoiler activation with regard to parafoil aircraft flight performance, a series of system identification flight tests were conducted in order to estimate basic aerodynamic properties of the test vehicle under development. Although a significant amount of work exists in the literature regarding aircraft system identification, the process of estimating various aerodynamic parameters for parafoil and payload aircraft is both unique and challenging for several reasons. Parafoil aircraft are unique in that typically very little sensory information exists from flight test data aside from positional information provided via GPS and barometric pressure measurements. Other types of sensors including inertial measurement units (IMU) and magnetometers have limited applications for parafoil aircraft in that these sensors are often mounted on the payload itself and separated from the canopy by a network of flexible rigging. Additionally, parafoil and payload aircraft have a limited number of available control channels in order to fully excite the dynamics of the system and often exhibit a high degree of variability from flight to flight due to their inherently flexible construction. An extreme sensitivity to outside disturbances including atmospheric wind and turbulence further complicates the estimation process considering the relatively slow flight speeds and low mass to volume ratios of airdrop systems.

In recent years, a number of techniques aimed at aerodynamic parameter estimation for airdrop systems have been explored including various output error methods (OEM) and other filtered estimation algorithms [46–52]. Resulting models range in fidelity from reduced order, linear models with as few as 3 or 4 degrees of freedom (DOF) to highly complex nonlinear 8 DOF models that take into account relative motion between the payload and parafoil canopy. Jann, Doherr, and Gockel have also led efforts to estimate various aerodynamic coefficients through the application of lifting line theory to an arc anhedral wing with good results [46]. Yakimenko and

Statnikov have also presented a method for estimating an 8 DOF parafoil model using a sophisticated multi-criteria optimization method [52]. However, the existence of local minima and infeasible regions made determination of the exact aerodynamic parameter set difficult. More specifically, many different sets of the unknown aerodynamic parameters were found to match equally well with observed flight data. The additional degrees of freedom accounting for payload motion helped match the natural eigenvalues of the measurements but provided little improvement in matching overall system trajectory.

Although a highly detailed case study in parafoil system identification is beyond the scope of this dissertation, the following sections detail the testing procedures and data reduction process for extracting steady-state flight characteristics including lift, drag, and turn rate, and matching the measured vehicle response to a suitable simulation model. As described in Chapter II, a “point” aerodynamic model is used within the 6 DOF equations of motion where all forces and moments acting over the entire canopy are computed at a single point. This technique is both computationally efficient and provides for a minimum number of coefficients needed to match the observed vehicle trajectory. However, it must be noted that several simplifying assumptions have been made in order to make the estimation problem more tractable given the limited sensory information and available control authority. Accordingly, the estimated aerodynamic model presented here is valid only for those flight regimes observed in test data and can not be assumed to accurately predict all of the transient modes exhibited during highly dynamic maneuvering. To this end, the resulting aerodynamic model is tuned to closely match steady-state lateral and longitudinal dynamics of the test vehicle while adequately capturing the measured transient response to changes in control input.

3.3.2 Extracting Steady-State Lift, Drag, and Turn Rate

The basic technique for extracting steady-state flight characteristics from parafoil aircraft test data follows that previously described by Ward, Costello, and Slegers [53, 54]. Here a specific set of input sequences or maneuvers are flown using the test vehicle while GPS position data and control inputs are continually logged and later post-processed to obtain high quality state estimates. Aerodynamic coefficients within the simulation model are then used to match these estimated steady-state characteristics instead of actual test data and later validated against select segments of test data not used during the estimation process. Figure 3.5 provides a simple flowchart of the specialized parafoil system identification method found in [54].

The input sequences used during flight tests include relatively long periods of constant control input allowing the system to not only reach steady-state, but continue its trajectory for several seconds or more thus minimizing the effect of sensor errors and

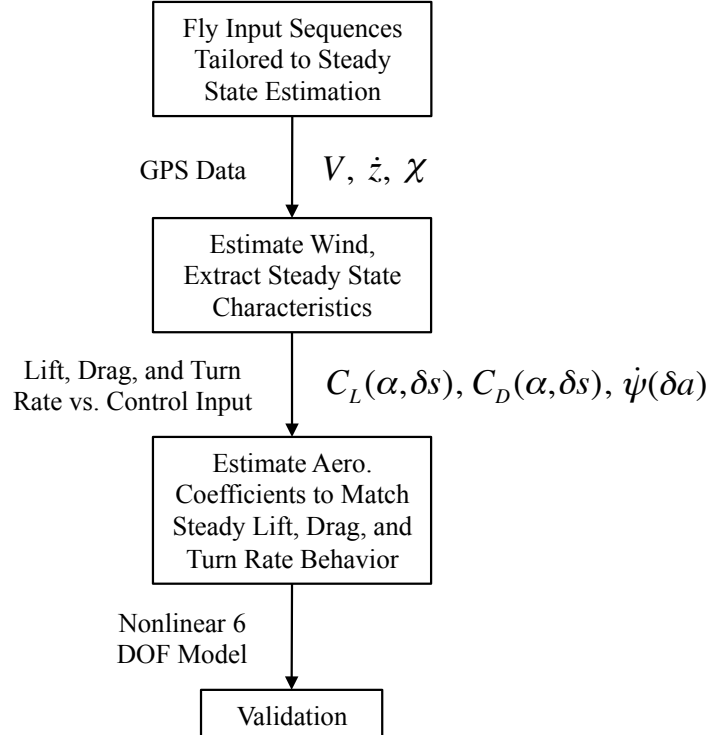


Figure 3.5: Specialized parafoil system identification method [54].

turbulence. Additionally, multiple tests are performed for each combination of both symmetric and asymmetric spoiler openings in order obtain an average response and further mitigate the possibility of sensor errors and other unknown disturbances. As noted previously, accurate estimation of the atmospheric wind vector for each period of constant control input is crucial for obtaining high quality steady-state estimates. Each period of constant control input should be held long enough for the test vehicle to fly at least one complete circle thus exposing the magnitude and direction of the atmospheric wind. Those control inputs in which the test vehicle is turning at a very low rate or flying nearly straight are performed either immediately before or after one complete rotation in which case the wind is assumed constant between test segments.

The atmospheric wind vector for a single period of constant control input is estimated by first decomposing the measured GPS ground track velocity vector, denoted V , into both a forward airspeed vector V_0 and a horizontal wind vector V_W as shown in the vector diagram in Figure 3.6. Note for each period of constant control input, both the forward airspeed and horizontal wind vector are assumed constant over the

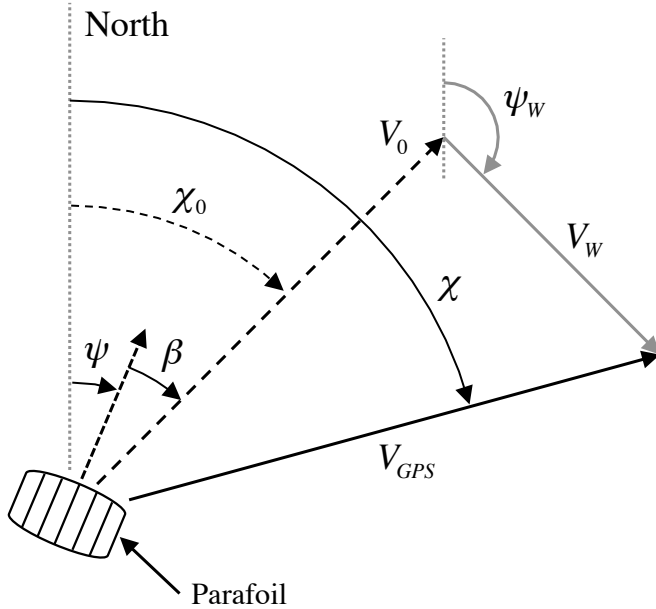


Figure 3.6: Parafoil ground track velocity decomposition.

entire data segment. For a series of n measurements acquired during one constant control segment, the i^{th} components of the ground track velocity along the north and east directions, denoted \dot{x}_i and \dot{y}_i , respectively, are written as follows:

$$\dot{x}_i = V_{W,X} + V_0 \cos(\psi_i) \quad (3.1)$$

$$\dot{y}_i = V_{W,Y} + V_0 \sin(\psi_i) \quad (3.2)$$

where $V_{W,X}$ and $V_{W,Y}$ are the constant wind speeds along the north and east directions, respectively, and ψ_i is the current vehicle heading angle. Note sideslip angle β is typically small for parafoil and payload aircraft in which case the azimuthal angle χ_0 is assumed to be equal to the actual system heading angle ψ . By combining equations (3.1) and (3.2) and solving for the forward airspeed term V_0 , the following expression shown in equation (3.3) is achieved.

$$V_0^2 = (\dot{x}_i - V_{W,X})^2 + (\dot{y}_i - V_{W,Y})^2 = V_i^2 + V_W^2 - 2(\dot{x}_i V_{W,X} + \dot{y}_i V_{W,Y}) \quad (3.3)$$

Equation (3.3) can be further simplified by subtracting the expected value of each term noting that any constant term minus its expected value is simply zero. This result is shown in equation (3.4).

$$0 = V_i^2 - E(V_i^2) - 2[(\dot{x}_i - E(\dot{x}_i))V_{W,X} + (\dot{y}_i - E(\dot{y}_i))V_{W,Y}] \quad (3.4)$$

Additionally, the expected value of all measured quantities are approximated by sample means shown in equation (3.5).

$$E(V_i^2) = \mu_{V^2}, \quad E(\dot{x}_i) = \mu_{\dot{x}}, \quad E(\dot{y}_i) = \mu_{\dot{y}} \quad (3.5)$$

At this point, the problem of estimating atmospheric wind for a single period of constant control input can be cast as a simple linear regression problem according to equation (3.6). Note without any heading angle variation, the matrix on the left hand side of equation (3.6) will contain only measurement noise thus resulting in a

poor wind estimate. Conditioning of the estimation process is improved by flying in a complete or nearly complete circular path in which data is captured over a variety of azimuth angles.

$$\begin{bmatrix} \dot{x}_1 - \mu_{\dot{x}} & \dot{y}_1 - \mu_{\dot{y}} \\ \vdots & \vdots \\ \dot{x}_n - \mu_{\dot{x}} & \dot{y}_n - \mu_{\dot{y}} \end{bmatrix} \begin{Bmatrix} V_{W,X} \\ V_{W,Y} \end{Bmatrix} = \frac{1}{2} \begin{Bmatrix} V_1^2 - \mu_{V^2} \\ \vdots \\ V_n^2 - \mu_{V^2} \end{Bmatrix} \quad (3.6)$$

With both north and east wind components known, vehicle forward airspeed and heading angle for each data point are subsequently computed according to equations (3.7) and (3.8). Note average forward airspeed is simply the mean of all data points for a single constant control segment.

$$V_{0,i} = \sqrt{(\dot{x}_i - V_{W,X})^2 + (\dot{y}_i - V_{W,Y})^2}, \quad V_0 = \frac{1}{n} \sum_{i=1}^n V_{0,i} \quad (3.7)$$

$$\psi_i = \tan^{-1} \frac{\dot{y}_i - V_{W,Y}}{\dot{x}_i - V_{W,X}} \quad (3.8)$$

Vehicle heading rate is subsequently computed by numerically differentiating the estimated heading angle for all data points and averaging. Lastly, vehicle descent rate is computed by simply averaging the vertical velocity directly measured from GPS or by numerically differentiating the barometric altitude measurement and averaging depending on what sensor information is currently available. Although not explicitly mentioned up to this point, vertical winds cannot be directly measured or estimated during the system identification process and are thus included within all vertical velocity measurements. As a result, system identification flight tests were performed during those days with relatively calm atmospheric winds and minimal thermal activity in order to minimize the effect of unknown vertical winds.

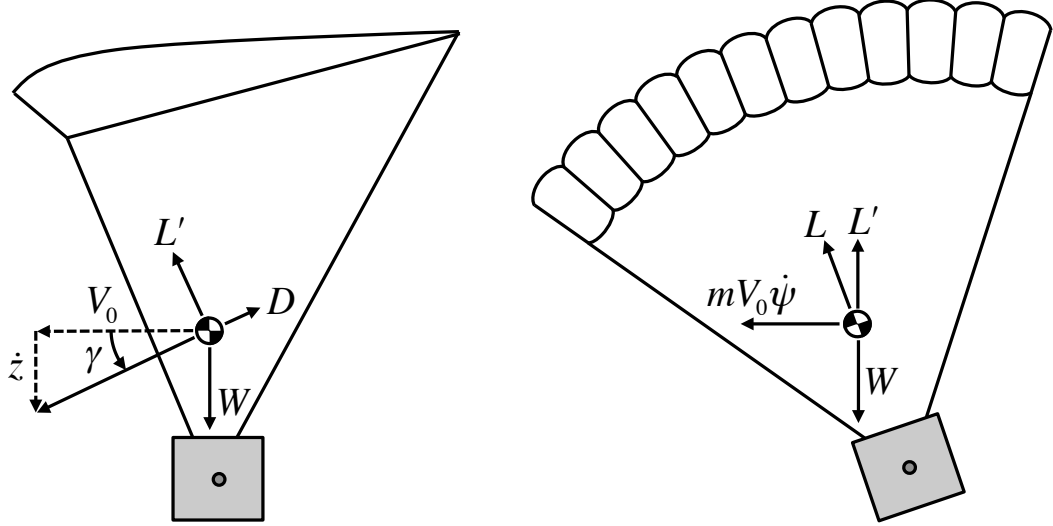


Figure 3.7: Parafoil side view (left) and front view (right) illustrating lift and drag relationship during steady turn.

Once airspeed, descent rate, and turn rate are known for each constant control segment, steady-state lift and drag are determined according to the diagram shown in Figure 3.7. Equations (3.9) – (3.12) detail the solution to the vector diagram where the corresponding steady-state lift and drag forces, denoted L and D , respectively are computed.

$$\gamma = \tan^{-1} \frac{\dot{z}}{V_0} \quad (3.9)$$

$$L' = W \cos(\gamma) \quad (3.10)$$

$$L = \sqrt{(L')^2 + (mV_0\dot{\psi})^2} \quad (3.11)$$

$$D = W \sin(\gamma) \quad (3.12)$$

3.3.3 Flight Test Results

In terms of lateral steering performance using upper surface canopy spoilers, several system identification flights were performed in order to measure the steady-state turn rate of the test vehicle in response to different levels of asymmetric spoiler opening.

The resulting turn rate versus asymmetric spoiler deflection for both Canopy 1 and Canopy 2 is shown in Figure 3.8 with dashed black lines representing the typical turn rate limits of ± 15 deg/s imposed by the guidance algorithm during autonomous flight. Recall from Section 3.1 that both Canopy 1 and Canopy 2 are geometrically identical with only slight differences in fabric stiffness. Positive values for asymmetric spoiler deflection correspond to right turns.

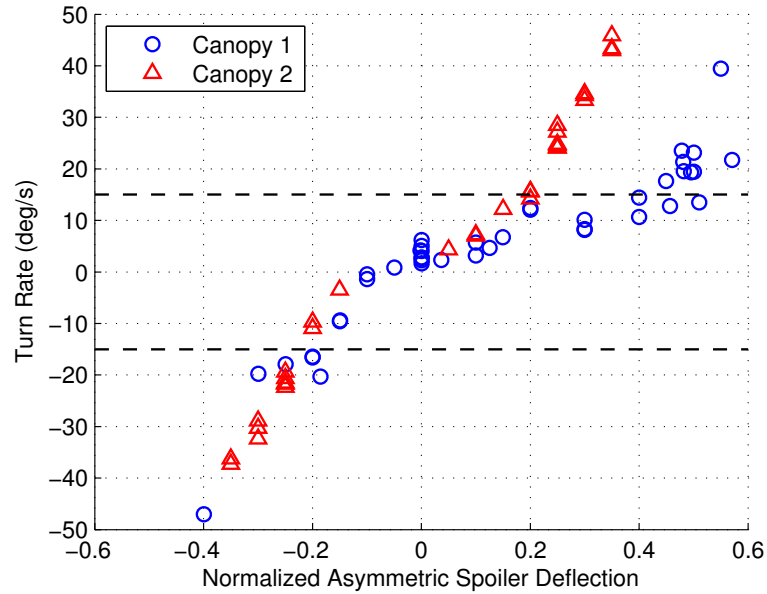


Figure 3.8: Measured test vehicle turn rate vs. normalized asymmetric spoiler deflection.

As seen in Figure 3.8, the estimated vehicle turn rate is both highly nonlinear and asymmetric with respect to turning direction. Right spoiler deflections for Canopy 1 result in significantly less lateral control authority than that of Canopy 2. Additionally, a slight reduction in turn rate with increasing deflection is evident for Canopy 1 between 0.2 and 0.3 of the total normalized asymmetric spoiler deflection. Left turns are more consistent for both Canopy 1 and Canopy 2 reaching a maximum of nearly 50 deg/s at 0.4 deflection placing the test vehicle in a near spiral dive.

Although nonlinear, asymmetric turn mappings are often encountered in airdrop systems, the degree to which these turn mappings vary given their identical size,

shape, and rigging suggests a high sensitivity of the upper surface spoiler mechanism to material stiffness. Opening of the upper surface spoilers involves pulling down at the center of the leading edge side of the upper surface slit causing the fabric nearest the opening to smoothly deform under the internal pressure within the canopy cell. In terms of Canopy 1, it was noted that the green fabric forming the right most section of cells was significantly more rigid and near paper-like in stiffness when compared to all other sections. The reduced right turning performance of Canopy 1 seen in Figure 3.8 is believed to result from the inability of the upper surface material on that side of the canopy to deform smoothly and uniformly when actuated. As a result, airflow through the right side upper surface spoilers is somewhat restricted compared to those on the left resulting in the observed asymmetric turn rate response.

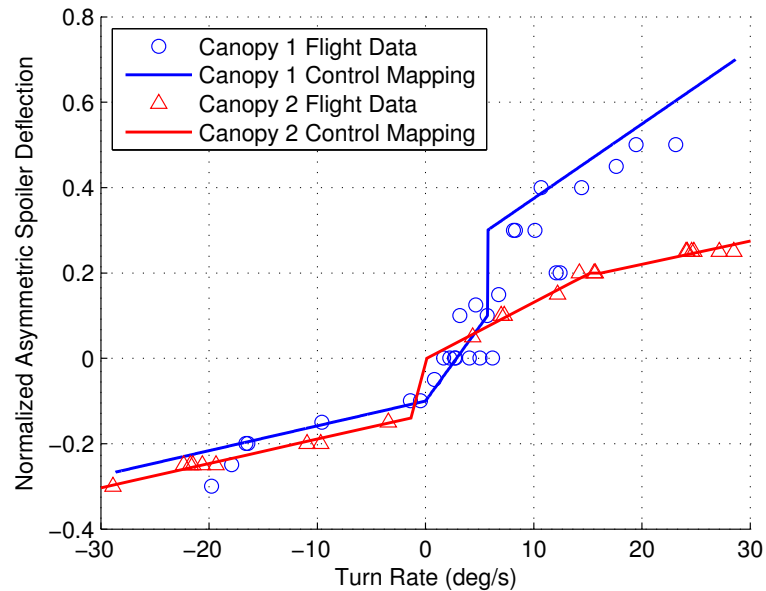


Figure 3.9: Measured test vehicle turn rate vs. normalized asymmetric spoiler deflection.

Using the measured turn rate versus asymmetric spoiler deflection for Canopy 1 and Canopy 2, a unique mapping relating the required normalized asymmetric spoiler deflection as a function of expected vehicle turn rate was constructed. This mapping, shown in Figure 3.9, is simply the inverse of the measured turn rate response and

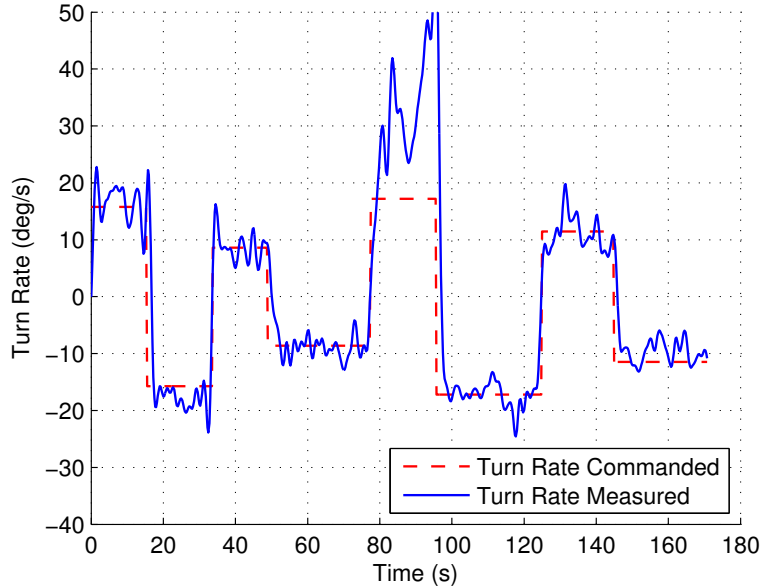


Figure 3.10: Open-loop turn rate tracking using Canopy 1.

is intended for use by the steering controller to relate the required control inputs given some commanded vehicle heading rate. Note that this mapping is essentially a static mapping unique to one specific canopy and vehicle and must be determined prior to autonomous flight. Validation of the turn rate mapping was performed in flight where several open-loop turn rate commands in either direction were specified while continuously estimating vehicle turn rate. Figure 3.10 shows the commanded and estimated vehicle turn rate time history for one of these open-loop flights using Canopy 1. Measured vehicle turn rate matches extremely well for nearly all specified turn rate commands except between 78 and 96 seconds where a right turn rate of 18 deg/s was commanded forcing the test vehicle into a near right spiral turn.

Aside from lateral steering performance, Figure 3.11 details the results of a second series of system identification flights specifically focused on longitudinal steady-state response (i.e. airspeed, descent rate, and turn rate) with different levels of symmetric spoiler deflection. Note these results are presented as a function of normalized symmetric spoiler deflection. Airspeed values ranging from 6.8 m/s to 7.7 m/s are estimated and shown in Figure 3.11a although no clear increasing or decreasing trend

is evident with increasing symmetric deflection. Alternatively, forward airspeed is relatively unaffected with changes in symmetric spoiler deflection from a nominal value of approximately 7.3 m/s.

Figure 3.11b shows significant changes in vehicle descent rate with increasing symmetric spoiler deflection ranging from a nominal value of approximately 3.0 m/s with all spoilers fully closed to over 5.0 m/s at near maximum usable symmetric spoiler deflection. Lastly, Figure 3.11c shows the range of expected glide slope variation with symmetric spoiler actuation. Note glide slope is computed as simply the ratio of forward airspeed over vertical descent rate. This result is extremely important

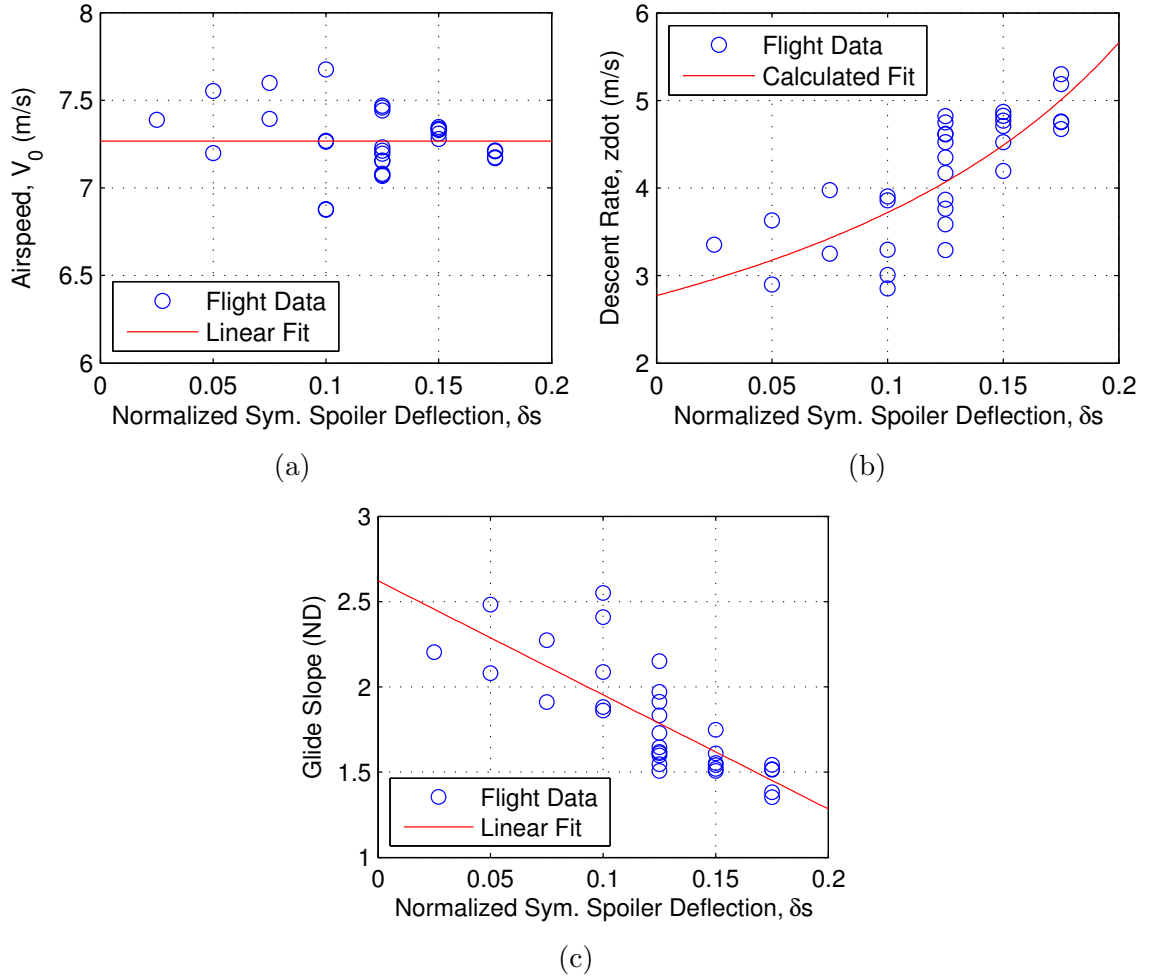


Figure 3.11: Steady-state flight characteristics versus normalized symmetric spoiler deflection δ_s including: (a) airspeed, (b) descent rate, and (c) glide slope.

in which the maximum longitudinal control authority of the upper surface spoiler mechanism is capable of reducing the test vehicle glide slope by over 40% from nearly 2.6 to less than 1.5.

3.3.4 Aerodynamics Summary

Using the estimated steady-state flight characteristics of the test vehicle discussed previously, a full set of aerodynamic coefficients were computed enabling accurate trajectory simulation in response to various symmetric and asymmetric upper surface spoiler openings. For completeness, Table 3.1 details all geometric and mass properties of the small scale test vehicle. Table 3.2 provides values for all aerodynamic coefficients used within the parafoil and payload dynamic model described in Chapter II.

Table 3.1: Test vehicle geometric and mass properties.

Parameter	Value	Units
Canopy Span, b	160.0	cm
Canopy Chord, c	61.0	cm
Canopy Planform Area, S_c	0.98	m ²
Nominal Incidence Angle, Γ	-10.0	deg
Payload Area, S_p	0.01	m ²
Total Weight, m	2.27	kg
Wing Loading, m/S_c	2.32 [0.47]	kg/m ² [lb/ft ²]
Inertia, I_{xx}	1.68	kg-m ²
Inertia, I_{yy}	0.80	kg-m ²
Inertia, I_{zz}	0.32	kg-m ²
Inertia, I_{xz}	0.09	kg-m ²
Apparent Mass, A	0.05	kg
Apparent Mass, B	0.35	kg
Apparent Mass, C	1.85	kg
Apparent Inertia, P	0.07	kg-m ²
Apparent Inertia, Q	0.06	kg-m ²
Apparent Inertia, R	0.05	kg-m ²

Table 3.2: Test vehicle aerodynamic coefficient summary.

Coefficient	Value	Coefficient	Value
C_{L0}	0.0	C_{lp}	-0.1
$C_{L\alpha}$	2.91	C_{lr}	0.0
$C_{L\alpha^3}$	-6.31	$C_{l\delta a}$	0.0
$C_{L\delta s}$	-1.83	C_{mq}	-2.5
C_{D0}	0.22	C_{np}	0.0
$C_{D\alpha^2}$	0.13	C_{nr}	-0.11
$C_{D\delta s}$	0.22	$C_{n\beta}$	0.02
$C_{Y\beta}$	-0.1	$C_{n\delta a}$	0.014
$C_{D,p}$	0.5		

Additionally, Figures 3.12 and 3.13 show the estimated lift and drag coefficient curves, respectively, of the test vehicle for several different values of symmetric spoiler deflection. Note C_{L0} with no symmetric spoiler opening ($\delta s = 0$) was fixed at zero for convenience. Also, lift and drag coefficients shown in Figures 3.12 and 3.13 represent values for the entire 3D parafoil wing and are based on actual flight data of the test vehicle.

An extremely important feature of each curve shown in Figures 3.12 and 3.13 that is unique to the upper surface canopy spoiler mechanism is the relative change or shifting of the curve with respect to increasing symmetric spoiler deflection. It must be noted that with increasing symmetric spoiler deflection ($\delta s > 0$), the entire lift coefficient curve is simply shifted down while the drag coefficient curve is shifted up. These changes in vehicle lift and drag are consistent with typical aerodynamic spoilers on the wings of conventional aircraft where actuation of the spoilers results in both decreased lift and increased in drag. In fact, this effect is somewhat opposite that associated with symmetric brake deflection on parafoil aircraft using conventional trailing edge brakes for control where increasing symmetric brake deflection subsequently causes an increase in both lift and drag.

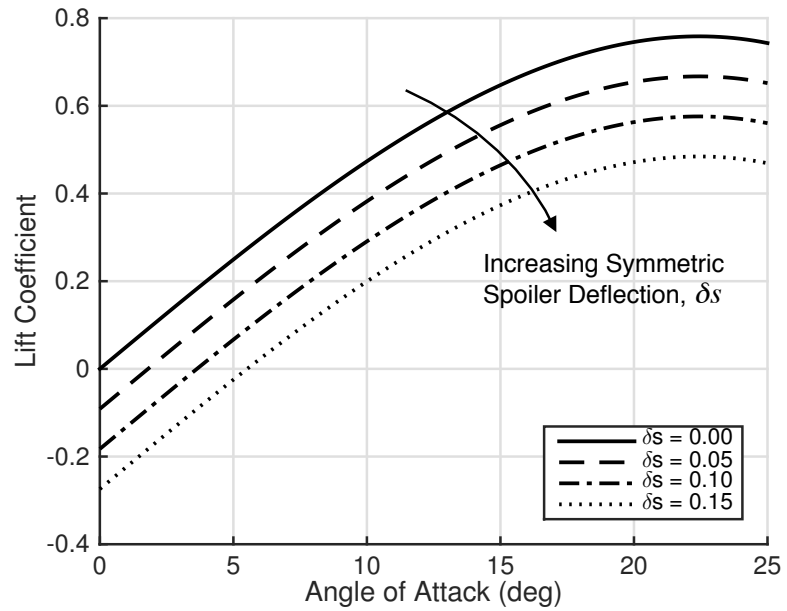


Figure 3.12: Test vehicle lift coefficient versus angle of attack for several different values of symmetric spoiler deflection.

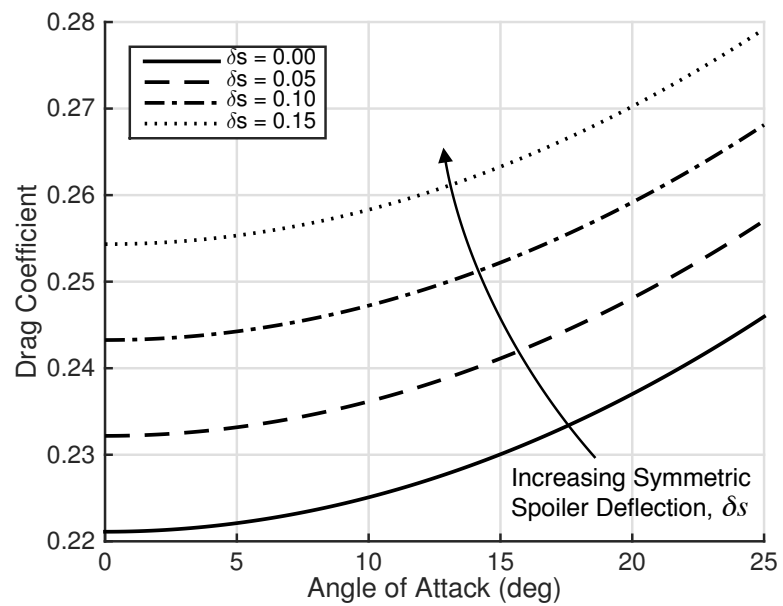


Figure 3.13: Test vehicle drag coefficient versus angle of attack for several different values of symmetric spoiler deflection.

CHAPTER IV

GUIDANCE, NAVIGATION, AND CONTROL

ALGORITHM

The guidance, navigation, and control (GN&C) algorithm is responsible for path planning, estimating relevant system states and atmospheric conditions, and determining the necessary system inputs to track the desired trajectory. The following sections address each of these tasks individually and describe the logic used during all autonomous flights presented within this paper. Note the basic algorithm presented here shares many of the same features with state-of-the-art autonomously guided systems discussed in literature. Where applicable, additional discussion has been included detailing the implementation of lateral and longitudinal control using upper surface canopy spoilers.

4.1 Guidance

The guidance algorithm employed here consists of a T-style approach and is divided into 4 separate phases – initialization, loiter, final approach, and terminal guidance. In order to simplify the required calculations, all path planning is performed within the wind fixed or wind relative reference frame (denoted with subscript WF) shown in Figure 4.1. Derivation of the wind fixed reference frame, originally introduced by Goodrick, Pearson, and Murphy [55] and later by Jann [23], consists of a translation based on the integral of the wind profile and vehicle sink rate followed by a rotation from the inertial frame such that the \vec{I}_{WF} axis points directly downwind. Although wind profile and sink rate may vary with altitude and control inputs, the transformation from the inertial frame to the wind fixed frame can be simplified by assuming

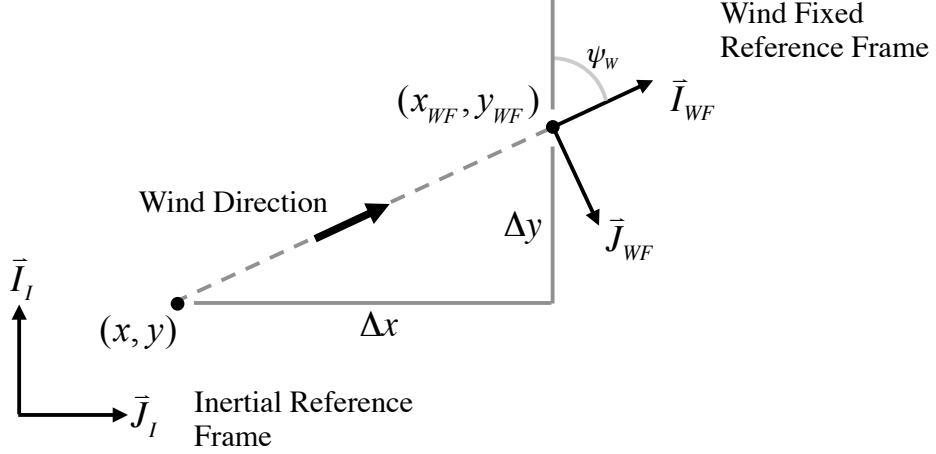


Figure 4.1: Wind fixed reference frame.

the parafoil sink rate as constant and using the current wind estimate. Accordingly, equations (4.1) – (4.3) detail the proposed simplifications and calculations required for transformation from inertial to wind fixed coordinates. Note that (x, y) are the current vehicle coordinates relative to the inertial frame, (x_{WF}, y_{WF}) are the transformed wind fixed coordinates, T_{rem} is an estimate of the time remaining in flight, $(V_{W,x}, V_{W,y})$ are the estimated wind vector components along the north and east directions, and ψ_W is the estimated wind vector direction. Vertical winds are not considered in the computation of the wind fixed frame.

$$T_{rem} = \frac{h}{\dot{z}} \quad (4.1)$$

$$\begin{Bmatrix} x_{WF} \\ y_{WF} \end{Bmatrix} = \begin{bmatrix} \cos(\psi_W) & \sin(\psi_W) \\ -\sin(\psi_W) & \cos(\psi_W) \end{bmatrix} \begin{Bmatrix} x + T_{rem}V_{W,x} \\ y + T_{rem}V_{W,y} \end{Bmatrix} \quad (4.2)$$

$$\psi_W = \tan^{-1} \frac{V_{W,y}}{V_{W,x}} \quad (4.3)$$

4.1.1 Initialization

The objective of the initialization phase is to estimate wind magnitude, wind direction, and vehicle airspeed in order to properly initialize the navigation filter used throughout the remainder of the flight. During initialization, a constant asymmetric spoiler input is commanded allowing the system to fly at least one complete circle. Typical turn rates commanded during initialization are between 10-15 deg/s. Using the resulting GPS velocity measurements, the task of estimating the horizontal wind components and system airspeed can be cast as a linear regression problem assuming each wind component and the vehicle airspeed are constant throughout the entire open-loop turn. Further detail regarding the solution of the linear regression problem can be found in [19].

4.1.2 Loiter

The loiter or energy management phase of the descent begins immediately following initialization and consists of a series of maneuvers intended to systematically reduce the excess altitude of the system before landing. The loiter strategy employed here is similar to that found in [23] where an alternating sequence of trajectories are generated between two fixed waypoints. Each waypoint is located on either end of a T-shaped pattern whose geometry remains stationary with respect to the wind fixed frame. Use of a T-shaped pattern ensures that each loiter waypoint is located downwind of the intended target in order to facilitate an upwind landing. Recall the axes of the wind fixed frame are always rotated to coincide with the estimated wind direction. A graphical illustration of the T-shaped loiter pattern is shown in Figure 4.2.

Figure 4.2 also presents an example trajectory between subsequent loiter waypoints. Here, Dubins paths [?] are used for trajectory planning consisting of two constant radius arcs joined by a single straight line segment. Arc radius, denoted R ,

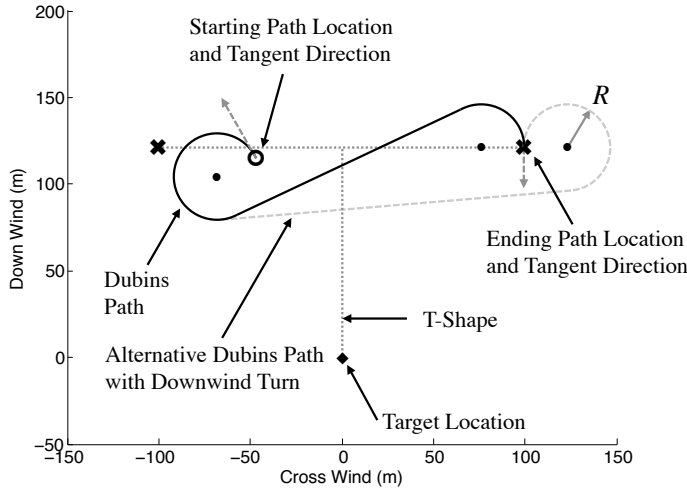


Figure 4.2: T-shaped loiter pattern relative to the wind fixed frame.

is dependent on both the forward airspeed and maximum turn rate of the vehicle and is left as an input parameter to the GN&C algorithm. As an illustrative example, the arc radius in Figure 4.2 was chosen as 25 m. Location of the loiter waypoints are also parameterized according to arc radius where each loiter target was located a distance $5R$ downwind of the intended target and offset a distance of $4R$ in the crosswind direction. Aside from the fixed arc radius, additional constraints for each Dubins path include fixed initial and final vehicle positions and tangent directions. Also, the direction of the first turn is set to equal that of the second turn from the previously computed path except for the case immediately following initialization where the direction of the first turn is arbitrary. The second turn is then chosen according to the minimum distance path satisfying all constraints. Although each turn is often opposite in direction resulting in a continuous figure eight pattern between each waypoint, this is not strictly enforced such that trajectories with initial and final turns in the same direction are also admissible.

During loiter, altitude required to reach the target from the current vehicle position is continuously computed each update cycle using equations (4.4) and (4.5). The instantaneous distance to the target, denoted L , is defined by the arc length with

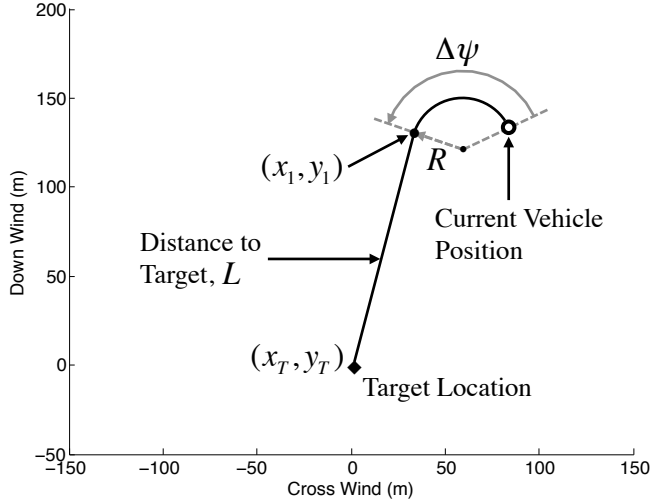


Figure 4.3: Instantaneous distance to target.

radius R required to turn from the current heading to point directly at the target and the straight line segment between the end of this turn and the target. Figure 4.3 provides a graphical depiction of the instantaneous distance from the target.

$$L = |\Delta\psi|R + \sqrt{(x_1 - x_T)^2 + (y_1 - y_T)^2} \quad (4.4)$$

$$h_{req} = L \frac{\dot{z}}{\hat{V}_0} \quad (4.5)$$

In equation (4.4), $\Delta\psi$ represents the change in vehicle heading necessary to point directly at the target, (x_1, y_1) are the end point coordinates of the circular arc, and (x_T, y_T) are the target coordinates. This distance then converted into the required height using equation (4.5) where \dot{z} and \hat{V}_0 represent the measured descent rate and estimated horizontal projection of vehicle airspeed, respectively. Once the current vehicle altitude drops below h_{req} , the guidance algorithm switches from loiter to final approach.

4.1.3 Final Approach

A two-stage final approach technique is employed where the parafoil and payload system initially begins tracking to an offset target following loiter before transitioning to the actual desired impact point. This technique facilitates landing of the vehicle pointing into the estimated wind vector by forcing the system to fly along the vertical stem of the T-shaped pattern. The offset target is located directly downwind of the actual target at an altitude intersecting the average glide path of the system where the average glide path is defined as the value centered within the longitudinal control range of the vehicle. Accordingly, any perturbation from the average glide path ensures that sufficient longitudinal control authority remains to bring the system back to the intended trajectory necessary to intersect the target. In the case where upper surface spoilers are used only for lateral steering and not active longitudinal control, the height of the offset target is lowered and coincident with the maximum glide path of the vehicle. Figure 4.4 provides an illustration of the longitudinal control strategy employed during final approach and terminal guidance.

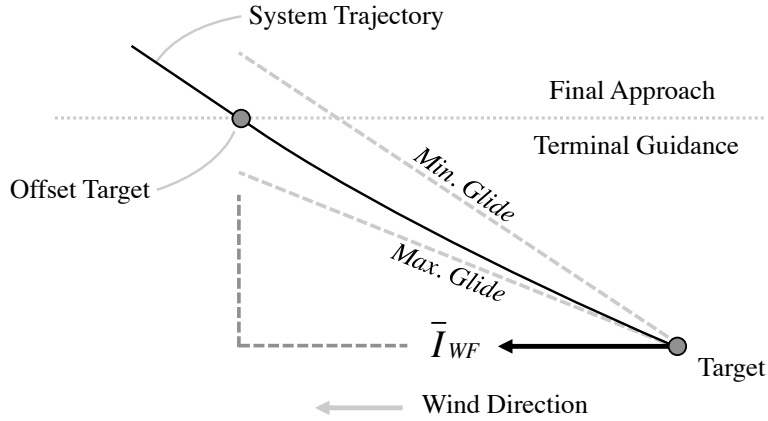


Figure 4.4: Terminal guidance strategy.

During final approach, the instantaneous distance to the target is continually updated in a manner similar to that employed during loiter. Using this distance estimate combined with altitude feedback, an estimate for the required vehicle glide

path necessary to intersect either the offset target or the actual target (depending on which target the system is tracking to at that time) is obtained. If the system is likely to overshoot the intended target, a proportional control strategy is implemented where the upper surface canopy spoilers are subsequently opened thus temporarily increasing the vehicle sink rate and allowing the system to drop down onto the correct glide path. All distance calculations are performed within the wind fixed reference frame such that the required glide path is relative to the atmosphere. Changes in wind direction near ground level are also included as the orientation of the wind fixed frame adjusts to coincide with the estimated wind direction.

4.1.4 Terminal Guidance

The guidance logic transitions from final approach to terminal guidance at the instant the altitude of the vehicle drops below the height of the offset target. Recall that the offset target is located directly downwind of the desired impact point at an altitude slightly higher than the nominal glide of the vehicle. The idea behind this technique is that if the vehicle reaches the offset target at the correct altitude, the remaining portion of the descent will focus primarily on traversing the stem of the T-shaped pattern while maintaining the proper heading and glide path necessary to intersect the target. In some ways, this technique is analogous to that of an instrument landing system (ILS) for fixed-wing aircraft. If terminal guidance is entered either above the minimum glide path or below the maximum glide path, the vehicle will inevitably overshoot or land short of the intended target, respectively. In this case, the guidance logic will simply saturate the symmetric spoiler control while simultaneously keeping the vehicle pointed either at the target or directly upwind of the target in an effort to minimize miss distance.

Just before ground impact, the vehicle executes a landing maneuver intended to minimize the kinetic energy of the system. In systems utilizing conventional trailing

edge brakes for control, this is typically accomplished by applying full symmetric brake just before touchdown. However, for the small-scale test vehicle using upper surface canopy spoilers with no trailing edge control, a third actuator is used to raise the canopy trim angle just before impact by lengthening the leading edge risers. This creates a flaring effect similar to that resulting from full trailing edge brake deflection. For larger autonomous systems, variable canopy incidence angle is not a typical feature, and a separate mechanism is required for kinetic energy reduction during landing.

4.2 Navigation

Following the open-loop initialization maneuver, the navigation algorithm is tasked with continually updating estimates of vehicle position, velocity, heading, heading rate, and atmospheric winds based on available sensory information. The estimation process uses two variants of the discrete Kalman filter, namely a standard Kalman filter for estimating vehicle position and velocity, and an extended Kalman filter for estimating vehicle heading, heading rate, and atmospheric winds [56].

In the interest of brevity, only state propagation and update equations for north position and velocity, denoted x_k and \dot{x}_k , are shown below noting that an identical representation is used for both east and vertical components of position and velocity. Accordingly, equation (4.6) shows the state propagation equation where the superscripts $(-)$ and $(+)$ represent pre and post update values, respectively

$$\begin{Bmatrix} x_{k+1}^- \\ \dot{x}_{k+1}^- \end{Bmatrix} = [\mathbf{A}] \begin{Bmatrix} x_k^+ \\ \dot{x}_k^+ \end{Bmatrix}, \quad [\mathbf{A}] = \begin{bmatrix} 1 & \Delta t \\ 0 & 1 \end{bmatrix} \quad (4.6)$$

Error covariance propagation, Kalman gain computation, and error covariance update equations are shown below

$$[\mathbf{P}_{k+1}^-] = [\mathbf{A}] [\mathbf{P}_k^+] [\mathbf{A}]^T + [\mathbf{Q}] \quad (4.7)$$

$$[\mathbf{K}_{k+1}] = [\mathbf{P}_{k+1}^-]([\mathbf{P}_{k+1}^-] + [\mathbf{R}])^{-1} \quad (4.8)$$

$$[\mathbf{P}_{k+1}^+] = ([\mathbf{P}_{k+1}^-]^{-1} + [\mathbf{R}]^{-1})^{-1} \quad (4.9)$$

where $[\mathbf{K}_{k+1}]$ represents the new Kalman gain matrix and $[\mathbf{Q}]$ and $[\mathbf{R}]$ denote the process and measurement noise covariance matrices, respectively, shown below in equation (4.10). Note process and measurement noise are assumed to be white, zero-mean Gaussian sequences. Also, measurement noise is assumed uncorrelated with process disturbance. Parameters used to define the process and measurement noise variance are listed in Table 4.1.

$$[\mathbf{Q}] = \begin{bmatrix} 0 & 0 \\ 0 & q_{\dot{X}} \end{bmatrix}, \quad [\mathbf{R}] = \begin{bmatrix} \sigma_X^2 & 0 \\ 0 & \sigma_{\dot{X}}^2 \end{bmatrix} \quad (4.10)$$

Table 4.1: Error parameters for position and velocity estimator.

	$q_{\dot{X}}$ (m/s) ²	σ_X (m)	$\sigma_{\dot{X}}$ (m/s)
North, East Position and Velocity	2.0	2.0	0.2
Vertical Position and Velocity	1.0	3.0	0.5

Lastly, equation (4.11) details the state update expression where x_{k+1}^* and \dot{x}_{k+1}^* denote GPS measurements of the current vehicle north position and velocity, respectively.

$$\begin{Bmatrix} x_{k+1}^+ \\ \dot{x}_{k+1}^+ \end{Bmatrix} = \begin{Bmatrix} x_{k+1}^- \\ \dot{x}_{k+1}^- \end{Bmatrix} + [\mathbf{K}_{k+1}] \begin{Bmatrix} x_{k+1}^* - x_{k+1}^- \\ \dot{x}_{k+1}^* - \dot{x}_{k+1}^- \end{Bmatrix} \quad (4.11)$$

Note that decomposition of the measured vehicle ground speed vector, denoted V_{GPS} in Figure 4.5, into the horizontal projections of vehicle airspeed, V_0 , and atmospheric wind, V_W , is not unique. Solution of the vector diagram shown in Figure 4.5 requires the assumption that airspeed is constant throughout the entire flight to formulate a more tractable problem. In this case, airspeed is assumed constant and

equal to the value computed following the open-loop initialization maneuver. Additionally, solution of the vector diagram does not yield an estimate of the parafoil heading angle, ψ , directly, but rather the azimuthal angle, χ_0 . However, the system sideslip angle, β , is typically small for parafoil and payload aircraft in which case the azimuthal angle is assumed to be equal to the actual heading angle.

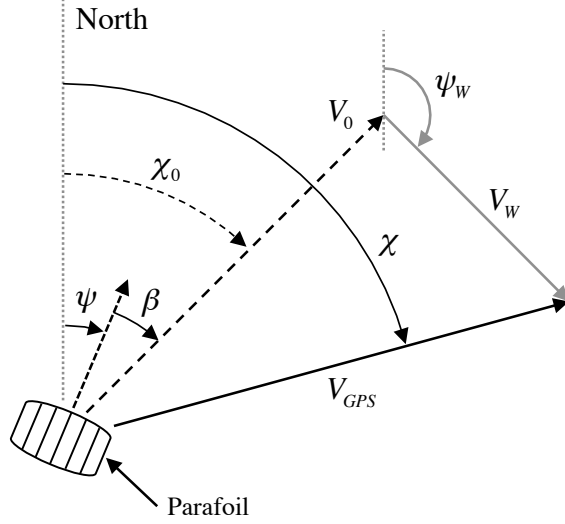


Figure 4.5: Parafoil ground track velocity decomposition.

For the heading, heading rate, and wind estimator, the plant dynamics and measurement equation are shown below. Four filter states are used, namely north and east wind components, denoted V_{WX} and V_{WY} , respectively, vehicle heading angle ψ , and vehicle heading rate $\dot{\psi}$.

$$\mathbf{x}_{k+1} = \mathbf{f}(\mathbf{x}_k) + \mathbf{w}_k \quad (4.12)$$

$$\mathbf{x}_{k+1} = \begin{Bmatrix} V_{WX,k+1} \\ V_{WY,k+1} \\ \psi_{k+1} \\ \dot{\psi}_{k+1} \end{Bmatrix}, \quad \mathbf{f}(\mathbf{x}_k) = \begin{Bmatrix} V_{WX,k} \\ V_{WY,k} \\ \psi_k + \dot{\psi}_k \Delta t \\ \dot{\psi}_k \end{Bmatrix}, \quad \mathbf{w}_k = \begin{Bmatrix} w_{V_{WX},k} \\ w_{V_{WY},k} \\ 0 \\ w_{\dot{\psi},k} \end{Bmatrix} \quad (4.13)$$

$$\mathbf{z}_k = \mathbf{h}(\mathbf{x}_k) + \mathbf{n}_k \quad (4.14)$$

$$\mathbf{z}_k = \begin{Bmatrix} \dot{x}_k^* \\ \dot{y}_k^* \end{Bmatrix}, \quad \mathbf{h}(\mathbf{x}_k) = \begin{Bmatrix} V_0 \cos(\psi_k) + V_{WX,k} \\ V_0 \sin(\psi_k) + V_{WY,k} \end{Bmatrix}, \quad \mathbf{n}_k = \begin{Bmatrix} n_{\dot{x},k} \\ n_{\dot{y},k} \end{Bmatrix} \quad (4.15)$$

Note \dot{x}_k^* and \dot{y}_k^* are the north and east velocities of the vehicle resulting from the standard Kalman filter. Also \mathbf{w}_k and \mathbf{n}_k represent the process and measurement noise vectors, respectively. Again, process and measurement noise are assumed to be white, zero-mean Gaussian sequences with no correlation between measurement and process disturbances.

Similar to the standard Kalman filter for position and velocity estimation, the following five equations comprise the discrete extended Kalman filter

$$\mathbf{x}_{k+1}^- = \mathbf{f}(\mathbf{x}_k^+) \quad (4.16)$$

$$[\mathbf{P}_{k+1}^-] = [\mathbf{F}] [\mathbf{P}_k^+] [\mathbf{F}]^T + [\mathbf{Q}] \quad (4.17)$$

$$[\mathbf{K}_{k+1}] = [\mathbf{P}_{k+1}^-] [\mathbf{H}_{k+1}]^T ([\mathbf{H}_{k+1}] [\mathbf{P}_{k+1}^-] [\mathbf{H}_{k+1}]^T + [\mathbf{R}])^{-1} \quad (4.18)$$

$$\mathbf{x}_{k+1}^+ = \mathbf{x}_{k+1}^- + [\mathbf{K}_{k+1}] \{ \mathbf{z}_{k+1} - \mathbf{h}(\mathbf{x}_{k+1}^-) \} \quad (4.19)$$

$$[\mathbf{P}_{k+1}^+] = ([\mathbf{I}] - [\mathbf{K}_{k+1}] [\mathbf{H}_{k+1}]) [\mathbf{P}_{k+1}^-] \quad (4.20)$$

where $[\mathbf{F}]$ and $[\mathbf{H}_{k+1}]$ are the state transition and observation matrices computed according to the following Jacobians shown in equations (4.21) and (4.22).

$$[\mathbf{F}] = \frac{\partial \mathbf{f}}{\partial \mathbf{x}} = \begin{bmatrix} 1 & 0 & 0 & 0 \\ 0 & 1 & 0 & 0 \\ 0 & 0 & 1 & \Delta t \\ 0 & 0 & 0 & 1 \end{bmatrix} \quad (4.21)$$

$$[\mathbf{H}_{k+1}] = \left. \frac{\partial \mathbf{h}}{\partial \mathbf{x}} \right|_{\mathbf{x}_{k+1}^-} = \begin{bmatrix} 1 & 0 & -V_0 \sin(\psi_{k+1}^-) & 0 \\ 0 & 1 & V_0 \cos(\psi_{k+1}^-) & 0 \end{bmatrix} \quad (4.22)$$

Process and measurement noise covariance matrices are provided below in equation (4.23). Additionally, Table 4.2 lists the error parameters used in the extended Kalman filter.

$$[\mathbf{Q}] = \begin{bmatrix} q_{VW} & 0 & 0 & 0 \\ 0 & q_{VW} & 0 & 0 \\ 0 & 0 & 0 & 0 \\ 0 & 0 & 0 & q_{\dot{\psi}} \end{bmatrix}, \quad [\mathbf{R}] = \begin{bmatrix} \sigma_V^2 & 0 \\ 0 & \sigma_V^2 \end{bmatrix} \quad (4.23)$$

Table 4.2: Error parameters for heading, heading rate, and wind estimator [57].

Error Parameter	Value	Units
q_{VW}	0.01	ft^2/s^2
$q_{\dot{\psi}}$	0.02	rad^2/s^2
σ_V	2.0	m/s

4.3 Control

The parafoil and payload system is controlled via opening and closing the upper surface bleed air spoilers. Based on the current waypoint target supplied by the guidance algorithm and the estimated vehicle location within the wind fixed reference frame, a commanded heading angle ψ_c is computed and subsequently passed to a proportional-integral (PI) controller in order to track the desired heading. The proportional component is nonlinear such that control effort resulting from small errors in system heading is reduced. Comparing the commanded heading angle with the

estimated vehicle heading angle from navigation, denoted $\hat{\psi}_{nav}$, a commanded turn rate, $\dot{\psi}_c$, is computed using equations (4.24) and (4.25).

$$\Delta\psi_{ratio} = \frac{\dot{\psi}_c - \hat{\psi}_{nav}}{\Delta\psi_{max}} \quad (4.24)$$

$$\dot{\psi}_c = \begin{cases} \dot{\psi}_{max}, & \text{if } \Delta\psi_{ratio} \geq 1 \\ -\dot{\psi}_{max}, & \text{if } \Delta\psi_{ratio} \leq -1 \\ \dot{\psi}_{max}\Delta\psi_{ratio}\sqrt{|\Delta\psi_{ratio}|}, & \text{else} \end{cases} \quad (4.25)$$

Here $\Delta\psi_{max}$ is the maximum difference between the commanded and estimated vehicle heading after which saturation occurs and $\dot{\psi}_{max}$ is the maximum allowable turn rate in either direction. From this commanded turn rate, the required asymmetric spoiler deflection is determined according to equation (4.26) where F is the known vehicle turn rate mapping determined through prior system identification. Lastly, δa_{bias} is the integral component computed from the difference between the commanded and estimated vehicle heading rates multiplied by the integral gain, K_I . The summation over the index i shown in equation (4.27) represents each GNC update in which the vehicle is operating under closed-loop tracking control following completion of the initialization phase.

$$\delta a = F(\dot{\psi}_c) + \delta a_{bias}, \quad \delta a \in [-1, 1] \quad (4.26)$$

$$\delta a_{bias} = K_I \sum_i [\dot{\psi}_c(i) - \hat{\psi}_{nav}(i)], \quad i = 1, \dots, N \quad (4.27)$$

Individual left and right spoiler deflections, denoted δl and δr , respectively, are subsequently computed according to equation (4.28) where $\delta l, \delta r \in [0, 1]$.

$$\delta l = \begin{cases} |\delta a| & \text{if } \delta a < 0 \\ 0 & \text{if } \delta a \geq 0 \end{cases}, \quad \delta r = \begin{cases} 0 & \text{if } \delta a < 0 \\ \delta a & \text{if } \delta a \geq 0 \end{cases} \quad (4.28)$$

In addition to lateral turning control, longitudinal control is computed exclusively during the last two phases of flight, namely final approach and terminal guidance. As previously mentioned, a proportional longitudinal control strategy is used during final approach and terminal guidance in which the system attempts to maintain its average glide path necessary to intersect the intended target. Accordingly, equation (4.29) is used to compute commanded glide slope, denoted GS_c , where GS_c is confined within the interval $[GS_{min}, GS_{max}]$.

$$GS_c = \begin{cases} GS_{min}, & \text{if } \frac{L}{h} \leq GS_{min} \\ GS_{avg} + K_{GS}(\frac{L}{h} - GS_{avg}), & \text{if } GS_{min} < \frac{L}{h} < GS_{max} \\ GS_{max}, & \text{if } \frac{L}{h} \geq GS_{max} \end{cases} \quad (4.29)$$

In equation (4.29), GS_{max} , GS_{min} , and GS_{avg} correspond to the maximum, minimum, and average values of system glide slope, L is the instantaneous distance from the target, h is the current vehicle altitude, and K_{GS} is the glide slope proportional gain. Asymmetric spoiler input (δa) and symmetric spoiler input (δs) are computed according to the known glide slope and turn rate mapping, denoted as the function H , shown in equation (4.30). In practice, this mapping is often implemented as a simple 2D table lookup based on previous flight data and system identification.

$$\delta a, \delta s = H(GS_c, \dot{\psi}_c), \quad \delta a \in [-1, 1], \quad \delta s \in [0, 1] \quad (4.30)$$

Left and right spoiler deflections are subsequently computed as follows.

$$\delta l = \begin{cases} |\delta a| + \delta s & \delta a < 0 \\ \delta s & \delta a \geq 0 \end{cases}, \quad \delta r = \begin{cases} \delta s & \delta a < 0 \\ \delta a + \delta s & \delta a \geq 0 \end{cases} \quad (4.31)$$

4.4 Example Autonomous Flight

A simulated autonomous flight trajectory is shown below to illustrate various aspects of the onboard GN&C algorithm as well as providing a detailed look at the entire parafoil and payload simulation framework. The trajectory begins from an altitude of 500 m above ground level. Atmospheric conditions are set relatively benign with an average wind speed of approximately 2 m/s blowing north and a standard deviation of the vertical direction gust component within the Dryden turbulence model of 0.2 m/s. Total miss distance is recorded at 3.2 m.

Figures 4.6 and 4.7 show the example trajectory with respect to the inertial and wind fixed reference frames, respectively. The flight begins at a point located 200 m south of the target where the system immediately enters the initialization phase consisting of a steady right turn. Note the presence of the atmospheric wind causing the system to drift downwind throughout the turn. Next, the GN&C algorithm immediately transitions to loiter where two ends of the figure eight pattern are completed before initiating final approach. As seen in Figure 4.6, each successive turn within the figure eight loiter pattern is performed further downwind. However, this inherent wind drift is effectively eliminated with respect to the wind fixed frame shown in Figure 4.7 where each end of the figure eight pattern is located at approximately the same

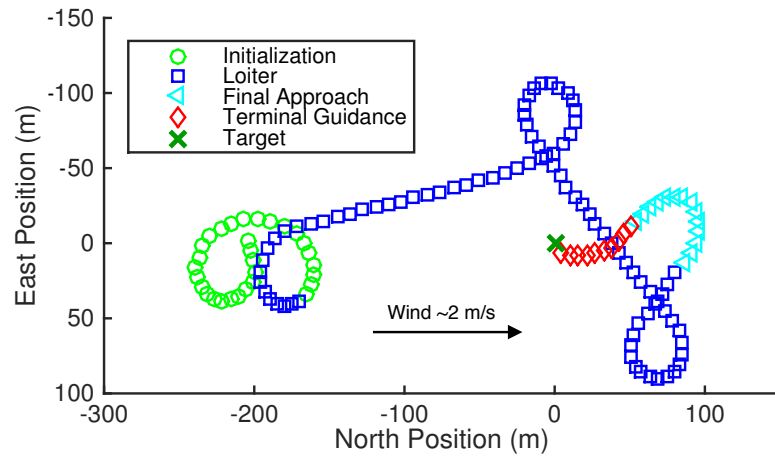


Figure 4.6: Inertial frame trajectory for example simulated autonomous flight.

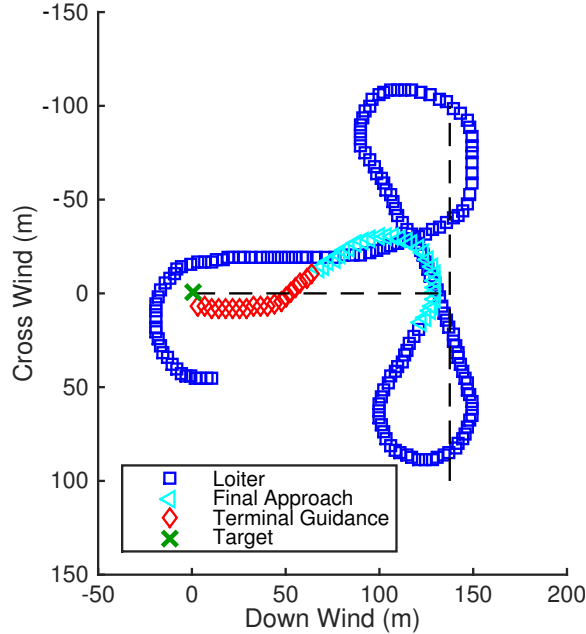


Figure 4.7: Wind fixed frame trajectory for example simulated autonomous flight.

distance downwind of the target according to the geometry of the T-shape denoted by the dashed black lines. By definition, computation of the wind fixed reference frame naturally compensates for any expected drift due to atmospheric winds such that all guidance and path planning calculations are performed using a consistent set of homing targets. Transition transition from loiter to final approach occurs at a point near the intersection of the horizontal and vertical sections of the T-shape after which the system immediately executes a 180 deg turn back to the target. Upon reaching the approach target altitude, the system transitions to the final guidance phase, denoted terminal guidance, and continues tracking upwind toward the target until landing.

Figures 4.8 and 4.9 show both the simulated winds and heading angle and heading rate tracking for the example autonomous flight. Note that only north and east wind components are estimated and used by the onboard GN&C algorithm. Vertical winds, although present in simulation, are not estimated during flight. Lastly, heading angle and heading rate tracking are very accurate indicating excellent lateral steering control of the vehicle.

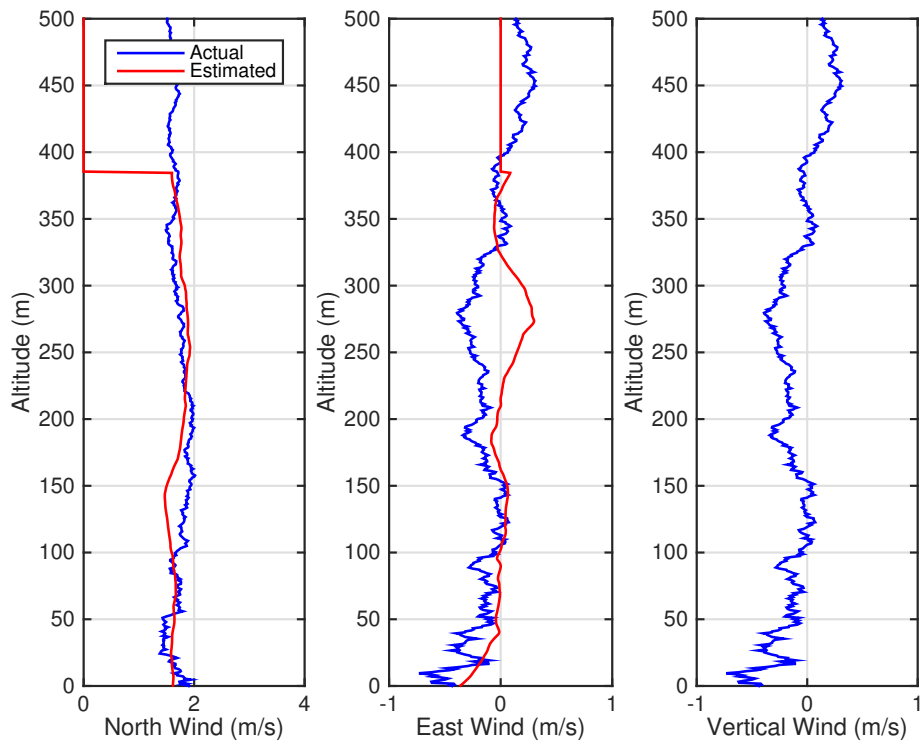


Figure 4.8: Actual and estimated winds for example simulated autonomous flight.

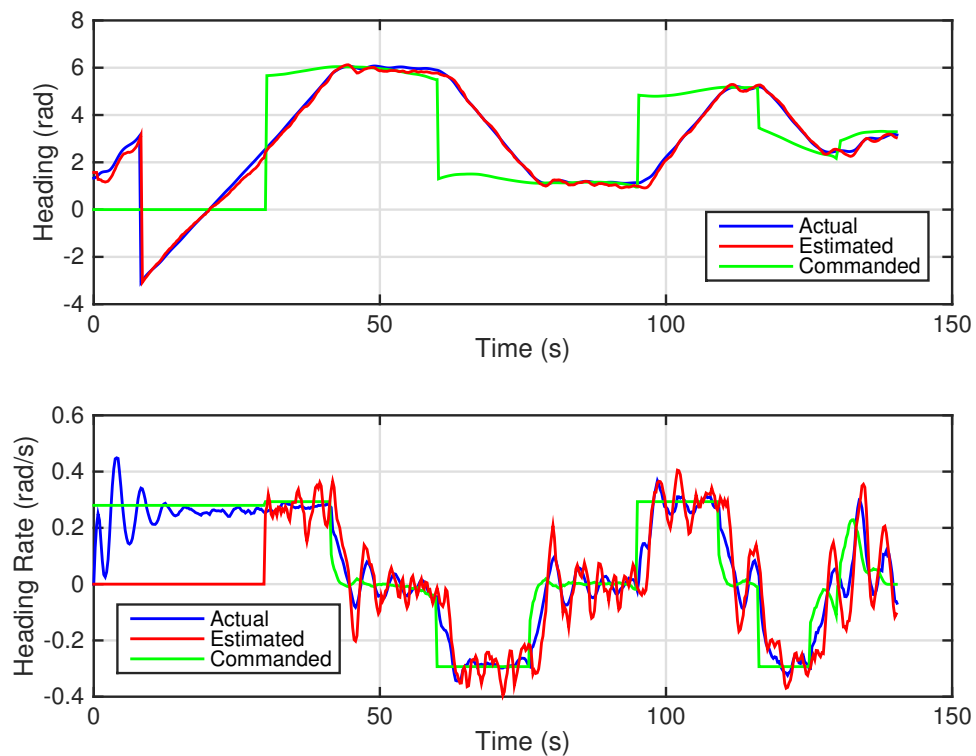


Figure 4.9: Heading angle and heading rate estimates and tracking.

CHAPTER V

AUTONOMOUS LANDING PERFORMANCE

This chapter examines the autonomous landing capability of the small scale parafoil and payload test vehicle using upper surface canopy spoilers exclusively for control. Aggregate landing accuracy statistics are computed in both simulation and through a series of autonomous flight experiments. All landing accuracy results are presented in terms mean miss distances and 50% and 90% circular error probable (CEP) distances which represent the radius of the circle, centered at the target, encompassing 50% and 90% of all recorded impact points. Specifically, Section 5.1 considers the autonomous landing accuracy of the small scale test vehicle using upper surface canopy spoilers for lateral steering control only, while Section 5.2 leverages the added longitudinal control authority of the upper surface canopy spoiler mechanism in a combined lateral and longitudinal control scheme. Lastly, Section 5.3 provides a summary of the simulated and experimental landing accuracy results as well as a comparison with previous work using a similar small scale parafoil and payload test vehicle equipped with trailing edge brakes and variable incidence angle for both lateral and longitudinal control.

5.1 Lateral Control Only

Using the parafoil and payload system dynamic model presented in Chapter II, a set of Monte Carlo simulations are conducted over a variety of atmospheric conditions to explore the performance of the small scale test vehicle equipped with upper surface canopy spoilers. In total, 250 simulated landings, each from 450 m altitude, were performed where the mean wind speed was varied uniformly from 0 – 6 m/s and the turbulence level was set to 0.65 m/s. Note turbulence level is defined as the

standard deviation of the vertical wind component within the Dryden turbulence model. Uncertainty in the assumed control mapping was also included to capture the effects of variability in vehicle response between subsequent flights — a problem commonly encountered with airdrop systems. In this case, the assumed turn rate mapping was simply scaled using a constant gain and shifted to create a nonzero turn rate bias. Also, several initial conditions including vehicle north and east position and initial heading angle were varied to simulate uncertainty in the “release point” of the test vehicle. In practice, the small scale test vehicle is manually piloted to some desired altitude and offset before initiating autonomous flight based on the pilot’s judgement of the current wind magnitude and direction. As a result, variability in vehicle position is necessarily included to mimic this behavior and is represented as some perturbation ($\Delta x, \Delta y$) from the origin of the wind fixed frame. Table 5.1 details the variation in all parameters used within the Monte Carlo simulation. Note that

Table 5.1: Monte Carlo simulation parameters.

Variable Description	Symbol	Value	Units
Mean North Wind	$\bar{V}_{W,x}$	unif(0, 6)	m/s
Mean East Wind	$\bar{V}_{W,y}$	0	m/s
Mean Vertical Wind	$\bar{V}_{W,z}$	0	m/s
Turbulence Level	σ_W	0.65	m/s
Turn Rate Gain	—	unif(0.8, 1.2)	—
Turn Rate Bias	—	unif(-0.06, 0.06)	rad/s
I.C.	x_0	$(z_0/w_0)\bar{V}_{W,x} + \text{unif}(0, \Delta x)$	m
I.C.	y_0	unif(0, Δy)	m
I.C.	z_0	-450	m
I.C.	ϕ_0	0	rad
I.C.	θ_0	0	rad
I.C.	ψ_0	unif(0, 2π)	rad
I.C.	u_0	7.35	m/s
I.C.	v_0	0	m/s
I.C.	w_0	3.7	m/s
I.C.	p_0	0	rad/s
I.C.	q_0	0	rad/s
I.C.	r_0	0	rad/s

Δx and Δy were set to 150 m each to ensure that all flights received an equal chance of reaching the target area. Maximum mean wind speed was set to 6 m/s, slightly less than the nominal forward airspeed of the vehicle. Mean wind direction was also fixed due north for simplicity. Lastly, all onboard GN&C calculations were performed at 4 Hz to match that of the test vehicle microprocessor and sensing suite.

Figure 5.1 shows the resulting landing dispersion for the 250 simulated landings. Impact coordinates for each landing are determined from the simulated GPS measurement at the time the vehicle touches down in order to compare with actual flight experiments. Also, landing errors are transformed into a down wind and cross wind frame based on the estimated wind direction from the GN&C algorithm at the time of impact. Note positive down wind values represent landings that are short of the intended target and vice versa. Miss distances in terms of 50% and 90% CEP are calculated to be 21.5 m and 55.7 m, respectively. Mean miss distance is also calculated at 28.1 m.

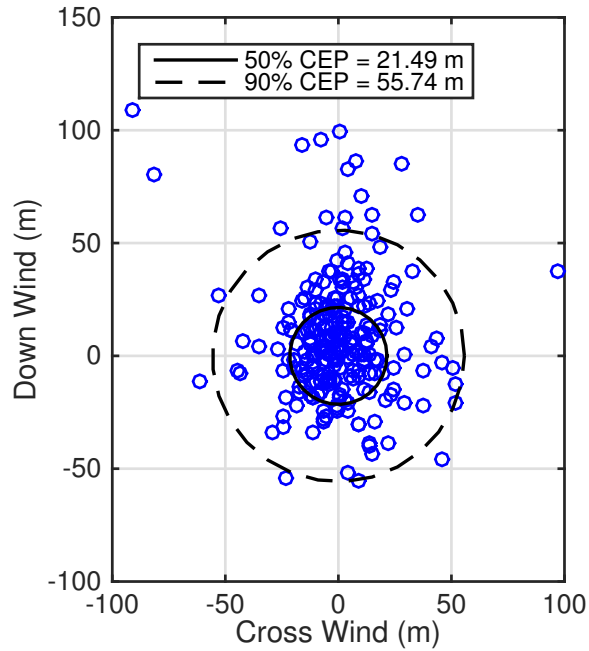


Figure 5.1: Landing dispersion for 250 simulated autonomous landings using upper surface canopy spoilers for lateral steering only.

In addition to the dispersion simulation, Figure 5.2 shows the predicted accuracy of the test vehicle as a function of atmospheric turbulence level for several different mean wind speeds including 0, 2, 5, and 8 m/s. For each mean wind speed, 100 autonomous landing were completed for six different turbulence levels ranging from 0.0 m/s to 1.0 m/s in increments of 0.2 m/s for a total of 2400 autonomous landings. Note uncertainty in all other parameters, excluding mean wind speed and turbulence level, were kept the same as listed in Table 5.1. Although the resulting trends are quite typical of most autonomous airdrop system, this data serves as a benchmark for the expected performance of the test vehicle and further supports the notion that upper surface spoilers are a viable control mechanism for autonomous parafoil aircraft. As expected, landing accuracy predictions are highly dependent on atmospheric turbulence level where nearly a four fold increase in mean miss distance is observed between relatively calm ($\sigma_W \leq 0.2$ m/s) and extremely gusty conditions ($\sigma_W \geq 1.0$ m/s). As an illustrative example, two different wind profiles are shown in Figure 5.3

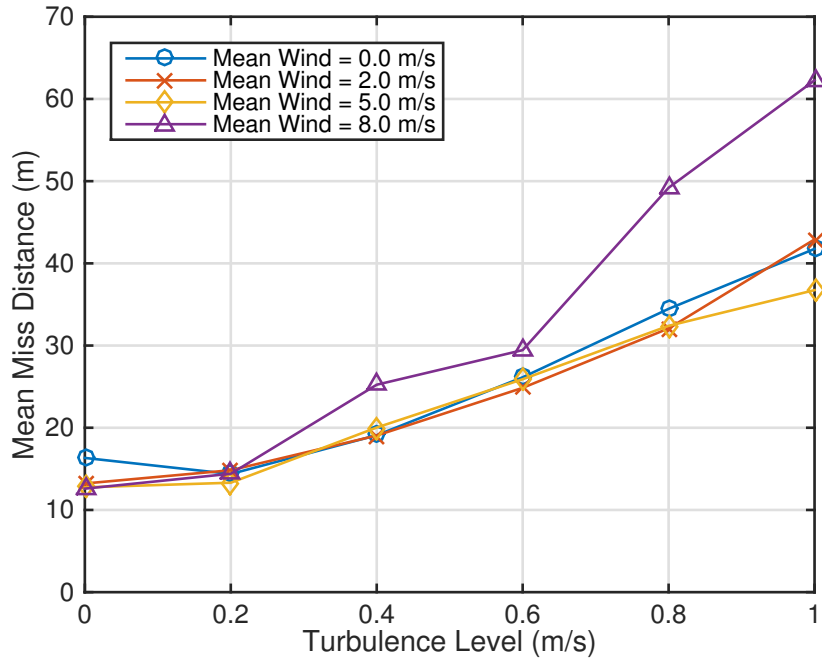


Figure 5.2: Simulated mean landing accuracy vs. mean wind speed for several different levels of turbulence (lateral steering control only).

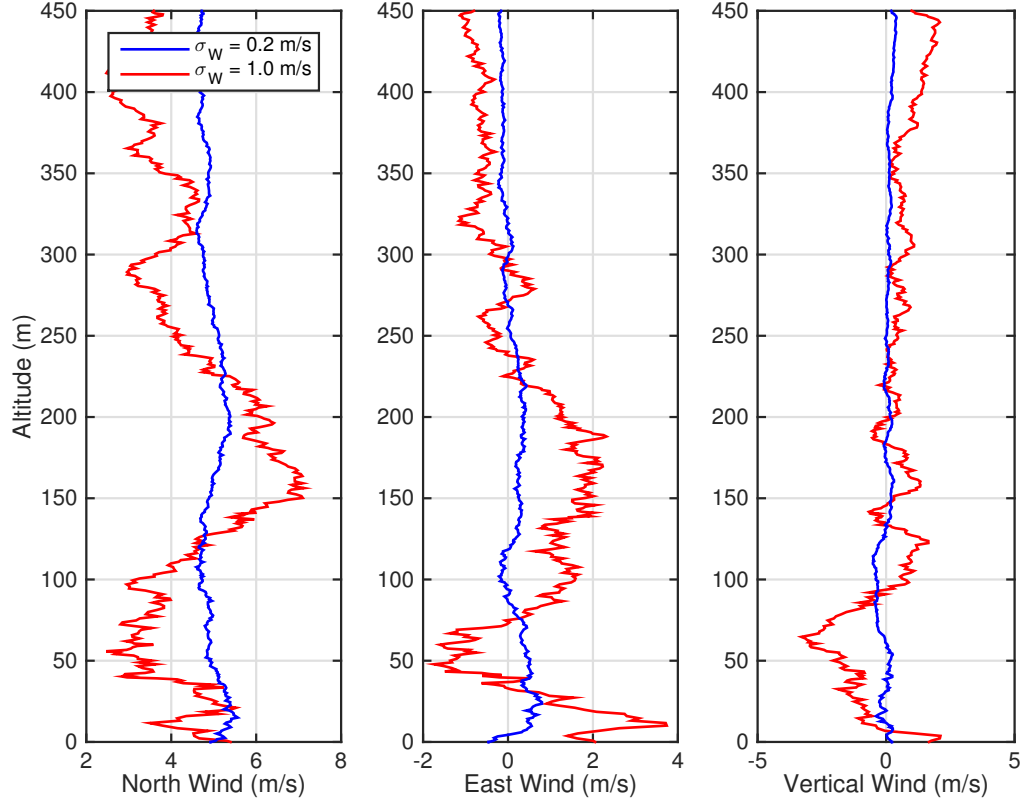


Figure 5.3: Example wind profiles for two different turbulence levels.

where each profile was generated using an identical random number sequence. The only difference between each case is the associated turbulence level where the blue lines are representative of relatively calm winds ($\sigma_W = 0.2 \text{ m/s}$) and the red lines depict extremely turbulent conditions ($\sigma_W = 1.0 \text{ m/s}$) with significant variations in wind speeds especially nearest ground level. Note the mean wind speed in each case was set to 5 m/s blowing north. These types of highly volatile atmospheric conditions pose an extreme challenge for any GN&C algorithm to overcome in order to maintain accuracy during landing.

One additional point of interest regarding Figure 5.2 is the fact that little variation exists in the predicted miss distance with increasing turbulence for mean wind speeds of 5 m/s or less. Although this result is somewhat counterintuitive, it is easily understood when considering the fact that all guidance and path planning is performed within a wind fixed reference frame and that the nominal flight speed of the

test vehicle is approximately 7.3 m/s — at least 40% higher than each of the lower three mean winds speeds considered. As long as the initial starting point of the flight places the vehicle within range of the intended target given the direction and speed of the wind, the actual value of the mean wind is irrelevant. In fact, even for the case in Figure 5.2 where the mean wind speed is set to 8 m/s, clearly exceeding the maximum flight speed of the vehicle, the predicted landing accuracy of the vehicle under mild conditions ($\sigma_W \leq 0.2$ m/s) is still quite close to that for all other wind speeds considered. As the turbulence level increases and the atmospheric winds begin to change significantly due to the increasing intensity of gusts, the vehicle location within the wind fixed frame is subsequently updated to reflect the updated wind estimates computed from the navigation filter. If the airspeed of the vehicle exceeds that of the mean wind and sufficient altitude margin exists, the vehicle will compensate for such changes and attempt to maintain a similar level of accuracy regardless of what the actual wind speed is. However, if the mean wind speed exceeds the flight speed of the vehicle, any unexpected change in the assumed wind is likely to place the vehicle too far down wind such that it is unable to reach the target. This effect is clearly seen in Figure 5.2 for $\sigma_W \geq 0.8$ m/s.

In an effort to validate the simulation results discussed previously, 31 autonomous flights using the small scale flight test vehicle shown in Figure 3.1 were performed — 22 with Canopy 1 and 9 with Canopy 2. The landing dispersion for all 31 flights is shown in Figure 5.4. Note that reported impact points are determined from the onboard GPS relative to the target coordinates at the instant the system touches down and have been similarly rotated to a down wind and cross wind frame based on the estimated wind direction at the time of landing. Miss statistics include 50% and 90% CEP values of 25.6 m and 51.0 m, respectively, and a mean miss distance of 27.9 m. Note a significant portion of flights using Canopy 1 overshot the intended target by at least 25 m. This result is likely the result of wind shears and other varying

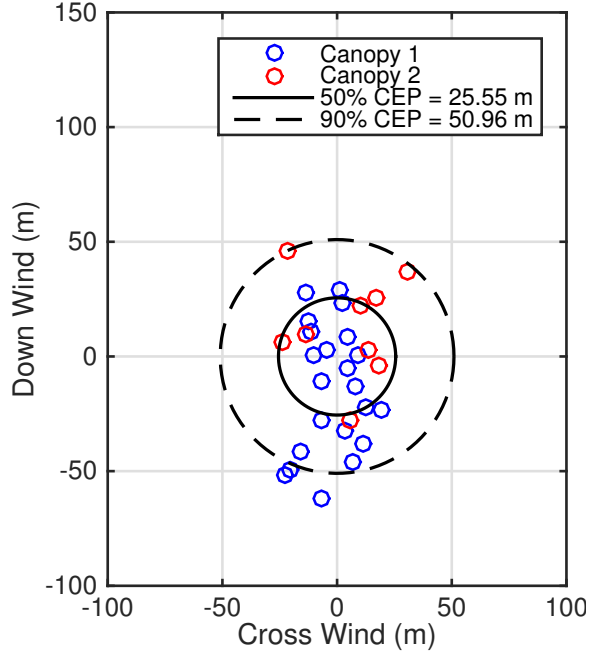


Figure 5.4: Landing dispersion for 31 autonomous flights using upper surface canopy spoilers for lateral steering only.

atmospheric conditions present during the days in which those particular flights were conducted and should not be misinterpreted as any significant finding.

It must be noted that the experimental landing accuracies agree very well with those predicted from simulation suggesting a high degree of confidence in the test vehicle dynamic model. Additionally, landing performance of the test vehicle equipped with either Canopy 1 or Canopy 2 is very similar regardless of the difference in turn rate response with asymmetric spoiler actuation. Such similarity in performance between canopies is expected given the known mapping between asymmetric control inputs and effective turn rate.

5.2 Combined Lateral and Longitudinal Control

With a clear understanding of the expected landing accuracy of the test vehicle using upper surface canopy spoilers for lateral steering only, a specialized control logic is now investigated aimed at leveraging the added longitudinal control authority of upper surface spoilers in a combined lateral and longitudinal control scheme. Here, upper surface spoilers are actuated both asymmetrically for lateral steering and symmetrically about the canopy centerline to actively control the glide ratio of the vehicle and compensate for any errors in approach trajectory. Accordingly, active longitudinal control of the vehicle is only applicable during the last two phases of the onboard GN&C algorithm, namely final approach and terminal guidance, where maintaining the proper glide path necessary to intersect the desired target is critically important for precise landing. Initialization and loiter phases remain unchanged except the altitude of the offset target has been raised slightly in order to intersect the average glide path of the test vehicle as opposed to the nominal or maximum glide with all spoilers closed. As noted previously, an approach trajectory coincident with the average glide path of the vehicle is desired such that sufficient longitudinal control authority exists to either increase or decrease the glide path of the vehicle as needed via symmetric actuation of the upper surface spoilers. Refer to Figure 4.4 in Section 4.1.4 for a graphical depiction of this terminal guidance strategy.

Similar to the lateral control only case, a second series of Monte Carlo simulations are performed consisting of 250 autonomous landings using the combined lateral and longitudinal control logic. Again, mean wind speed was varied uniformly from 0 – 6 m/s while the turbulence level was held constant at 0.65 m/s. Figure 5.5 compares the simulated landing dispersion for both the lateral control only case discussed previously and the combined lateral and longitudinal control scheme. Impact point errors are again computed from the simulated GPS measurements and presented in a down wind and cross wind reference frame based on the estimated ground wind direction at the

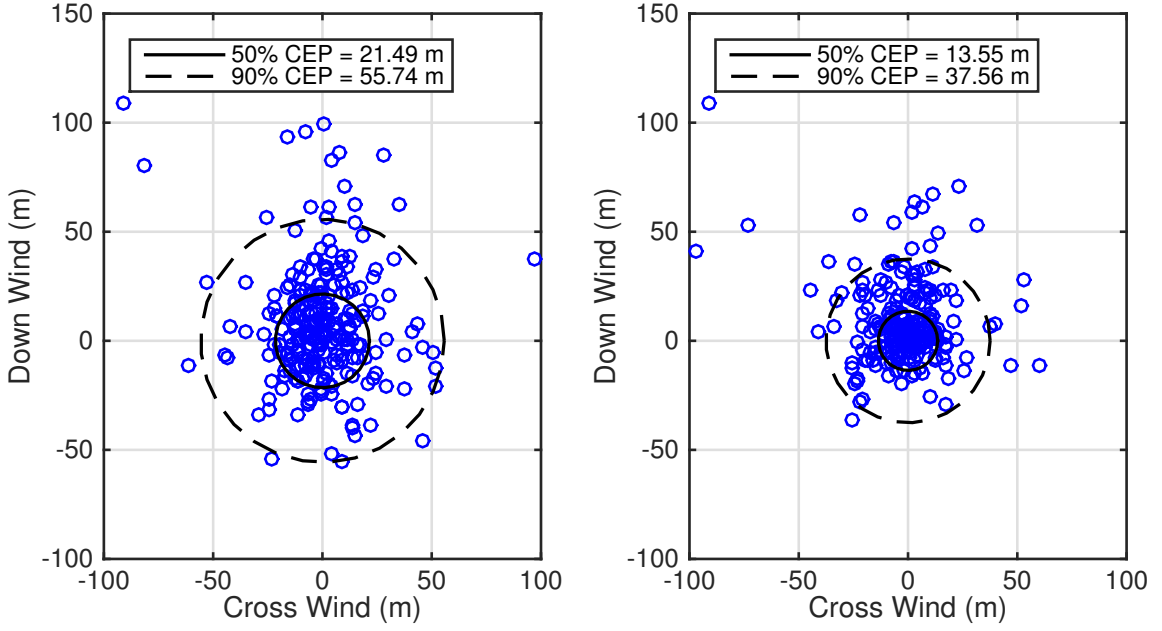


Figure 5.5: Simulated landing dispersion for (left) lateral only control and (right) combined lateral and longitudinal control.

instant the vehicle lands. Miss distances in terms of 50% and 90% CEP are recorded as 13.6 m and 37.6 m, respectively, using the combined control logic resulting in a 37% reduction in 50% CEP and a 33% reduction in 90% CEP. Mean miss distance was also computed at 19.5 m.

To further detail the unique terminal guidance strategy with the combined lateral and longitudinal control logic, Figure 5.6 shows both vehicle altitude and normalized control inputs as a function of instantaneous distance from the target for an example simulated flight. Note the dashed black lines represent the maximum and minimum glide path of the vehicle extending from the target, i.e. glide ratios of approximately 2.5 and 1.5, respectively. As seen in Figure 5.6, the vehicle is initially too high as it approaches the target given its current glide rate. As expected, the onboard control logic recognizes this situation and subsequently opens the upper surface canopy spoilers via increased symmetric control between 60 m and 110 m from the target causing the vehicle to temporarily increase its vertical descent rate and effectively lowering the glide ratio of the system. As a result, the vehicle subsequently “drops” onto the

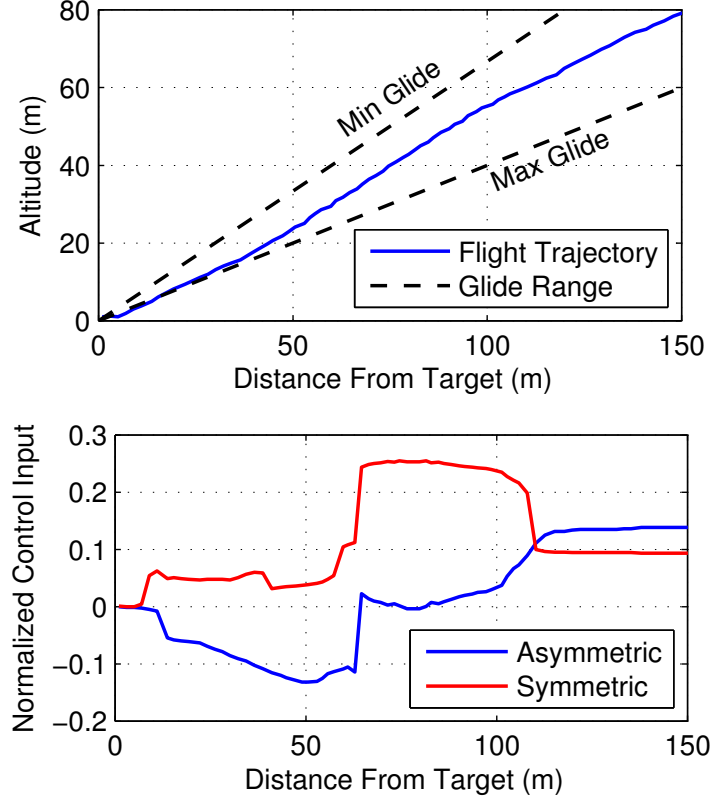


Figure 5.6: Altitude (top) and normalized control input (bottom) versus instantaneous distance from the target for example autonomous flight trajectory.

correct glide path and maintains this trajectory necessary to intersect the target until landing.

Figure 5.7 compares the mean landing accuracy using both lateral control only and combined lateral and longitudinal control with increasing turbulence level at four different mean wind speeds including 0, 2, 5, and 8 m/s. Again, each circular marker represents a series of 100 autonomous landings with uncertainty in all parameters, excluding mean wind speed and turbulence level, set according to Table 5.1. In the first three cases where the mean wind speed is less than the nominal flight speed of the vehicle, the combined lateral and longitudinal control logic is quite effective in reducing mean miss distances by as much as 25% in zero mean wind conditions. Also it appears that in all four cases, the combined lateral and longitudinal control is more effective in reducing impact point errors under higher levels of turbulence.

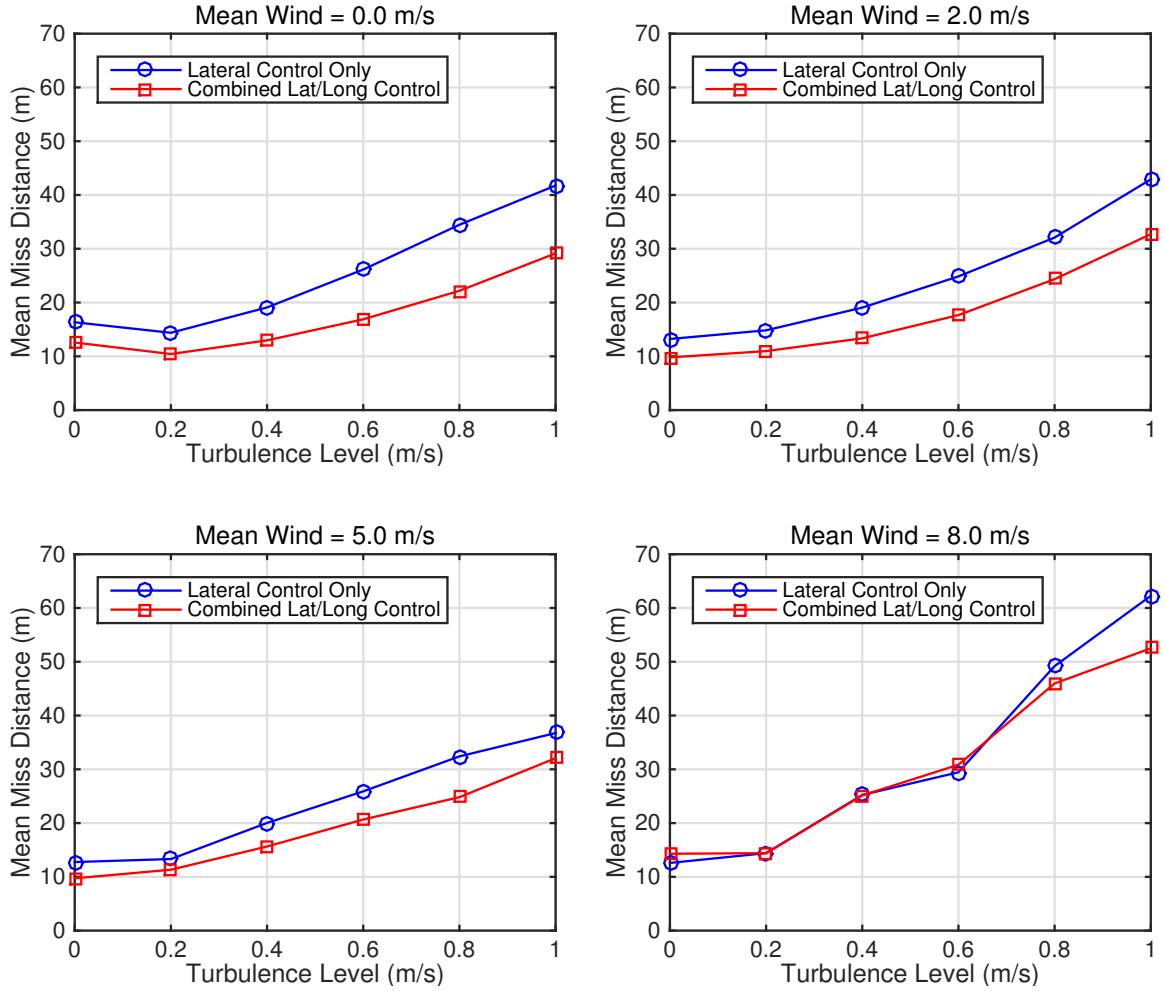


Figure 5.7: Landing accuracy comparison between lateral only control and combined lateral and longitudinal control vs. turbulence for different values of mean wind.

Additionally, the relative improvement in mean miss distance when using the combined control logic is diminishing slightly with increasing mean wind speeds to the point where no apparent benefit is evident at 8 m/s except for the most turbulent conditions. This result is more easily explained when considering that longitudinal control using upper surface canopy spoilers is intended to compensate for errors in approach trajectory resulting from wind gusts and other outside disturbances. In relatively low turbulence, steady wind conditions, there are fewer disturbances for the longitudinal controller to compensate for resulting in a marginal improvement in landing accuracy over lateral steering only. In highly turbulent conditions, the

advantage of longitudinal control via upper surface spoilers is much more significant given the presence of higher intensity winds gusts and other unexpected disturbances. Lastly, the most significant reduction in mean miss distance occurs in relatively gusty conditions with near zero mean wind. These conditions are often referred to as “light and variable” winds in which the wind direction is constantly changing. Under these conditions, the combined control logic is most effective in compensating for approach errors given its added longitudinal control authority and significant margin in vehicle airspeed relative to wind speed. In conditions with higher wind speeds, the wind direction is more consistent.

In addition to the simulation results using the combined lateral and longitudinal control logic, a total of 70 autonomous landings were recorded over four days of testing in Eloy, Arizona (February 17-20, 2014) under a variety of wind conditions. Figure 5.8 illustrates flight operations in Eloy, AZ where two parafoil and payload systems are shown in the foreground next to the target immediately following landing. Note the operator vehicle and ground station location are also visible in the background. For each autonomous flight, total miss distance was calculated based on the



Figure 5.8: Flight testing operations in Eloy, AZ.

GPS location of the vehicle immediately following impact. Figure 5.9 presents both the landing dispersion for all 70 autonomous flights using Canopy 2 exclusively and a comparison of landing error with mean wind speed estimated over the entire flight. Note mean wind speeds range from relatively calm conditions up to speeds approaching the nominal airspeed of the vehicle. Values for the 50% and 90% CEP regions are calculated to be 13.2 m and 28.8 m, respectively. Mean miss distance is 15.7 m. Accordingly, flight tests results indicate excellent performance of the test vehicle using the combined lateral and longitudinal control logic with nearly an equivalent 50% CEP distance predicted from simulation and a 48% reduction in 50% CEP when compared to previous flight tests using lateral steering only. Additionally, the majority of misses greater than 20 m occurred during flights with relatively low mean winds (~ 2 m/s) characteristic of “light and variable” conditions in which the wind direction is constantly changing.

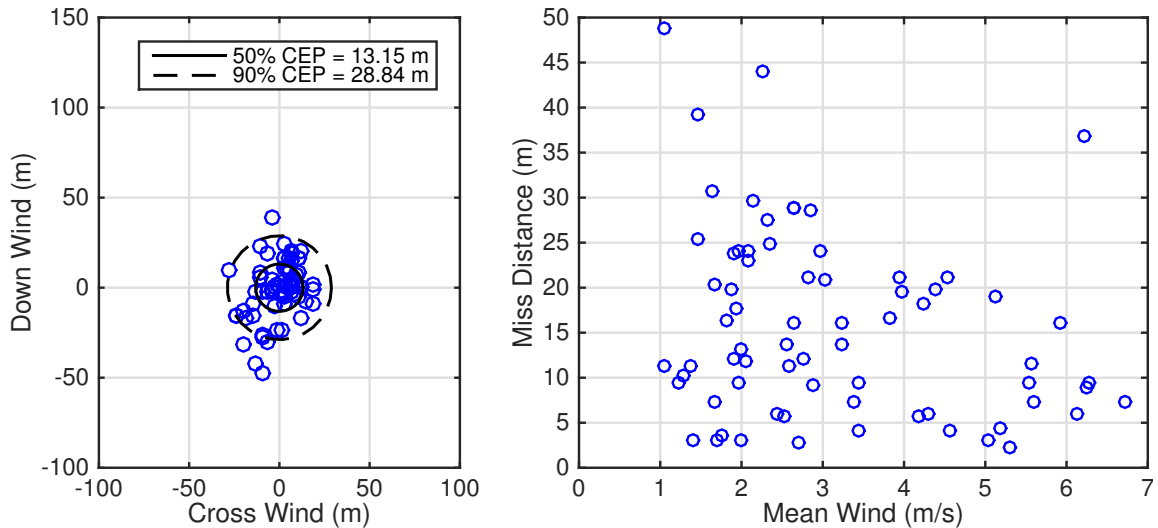


Figure 5.9: Experimental landing dispersion (left) and calculated miss distance versus estimated mean wind speed (right) for 70 autonomous flight tests using upper surface canopy spoilers for combined lateral and longitudinal control.

5.3 Summary and Comparison with Conventional Control Mechanisms

As shown from the simulation and experimental landing accuracy results, it is clear that upper surface canopy spoilers are a viable control mechanism for both lateral only and combined lateral and longitudinal control of autonomous parafoil aircraft. Table 5.2 summarized the simulation and experimental landing accuracy results of the small scale test vehicle using upper surface canopy spoilers exclusively for control. Note simulation and experimental 50% CEP values are nearly identical for the combined lateral and longitudinal control indicating excellent model agreement with the physical test vehicle. Experimental accuracies are slightly higher than predicted from simulation for the lateral only case mainly due to the limited number of experimental flight and the difficult atmospheric conditions experienced during testing. In either case, a significant improvement in 50% CEP is evident (37% simulated, 48% experimental) demonstrating the capability of the autonomous system to leverage the added longitudinal control authority from the upper surface spoilers in order to compensate for disturbances and maintain accurate landing.

Table 5.2: Simulation and experimental landing accuracy statistics.

Metric Description	50% CEP (m)	90% CEP (m)	Reduction in 50% CEP
Simulation — Lateral Only (250 Landings)	21.5	55.7	—
Simulation — Combined Lat/Long (250 Landings)	13.6	37.6	37%
Flight Tests — Lateral Only (31 Landings)	25.6	51.0	—
Flight Tests — Combined Lat/Long (70 Landings)	13.2	28.8	48%

Although upper surface canopy spoilers are clearly an effective mechanism for longitudinal control of parafoil aircraft, other techniques exist for improving accuracy via

longitudinal control, including symmetric trailing edge brake deflection for airspeed control and variable canopy incidence angle control. Ward and Costello have shown through extensive simulation and experimental flight testing with a similar small scale parafoil and payload test vehicle that similar improvements in landing accuracy using longitudinal control are possible. Table 5.3 compares the landing performance using upper surface canopy spoilers with conventional trailing edge deflection and variable canopy incidence angle control found in [32].

Table 5.3: Comparison of landing accuracies using upper surface canopy spoilers with conventional control mechanisms.

Metric Description	50% CEP (m)	Mean Miss (m)	Reduction in 50% CEP
<i>Upper Surface Spoilers:</i>			
Simulation — Lateral Only	21.5	28.1	—
Simulation — Combined Lat/Long	13.6	19.5	37%
Flight Tests — Lateral Only	25.6	27.9	—
Flight Tests — Combined Lat/Long	13.2	15.7	48%
<i>T.E. Brakes / Var. Incidence [32]:</i>			
Simulation — Lateral Only	19.1	27.2	—
Simulation — Combined Lat/Long	12.3	15.5	36%
Flight Tests — Lateral Only	20.1	26.2	—
Flight Tests — Combined Lat/Long	10.9	14.7	46%

As shown above, the performance improvement using upper surface canopy spoilers for both lateral and longitudinal control is nearly identical to that using conventional trailing edge brakes and variable incidence angle control. However, the important point to take away from the data shown in Table 5.3 is the similar level of performance gained considering the simplicity and inherent advantages associated with spoiler based control, such as lower actuator loads and line deflection requirements and reduced canopy rigging complexity. In practice, implementation of variable canopy incidence (i.e. trim) angle control is nontrivial and requires an additional actuator and significantly complicates the parachute rigging and packing process for large scale autonomous systems. Added cost, size, and weight of the additional hardware

required for variable incidence angle control are some of the main reasons why this is not the norm for all autonomous parafoil aircraft. Accordingly, the following chapters aim to provide a practical path forward for integrating upper surface spoilers into large scale parafoil aircraft that breaks the paradigm of conventional payload borne actuation through the development of a novel in-canopy spoiler actuation system.

CHAPTER VI

IN-CANOPY BLEED AIR ACTUATION SYSTEM

To this point, all of the results presented in this dissertation have focused on simulation and flight testing of small scale parafoil and payload aircraft. More specifically, actuation of the upper surface bleed air control mechanism was performed using two independent actuators mounted on the payload of the vehicle with a network of control lines connecting each actuator to the upper surface bleed air openings. Additionally, opening of the upper surface spoilers was limited to two distinct groups of several spoilers on either side of the canopy centerline operating in tandem as left and right spoilers. Although this technique has proven effective as evidenced in Chapter V, the upper surface spoiler mechanism is in no way restricted to operate within this conventional paradigm of payload borne actuation. Accordingly, the following sections detail the design and development of a novel in-canopy wireless bleed air actuation system in which specialized winch actuators mounted entirely within the parafoil canopy itself are used to open and close the upper surface spoilers via a unique internal rigging structure.

Although the concept of in-canopy bleed air actuation is independent of vehicle size and weight, all remaining work presented in this dissertation focuses on design and development of a complete in-canopy actuation system suitable for large scale parafoil aircraft with a total rigged weight of 376 lbs. Additionally, all flight testing was performed in conjunction with the Natick Soldier Research Development and Engineering Center (NSRDEC) Airdrop Technology team from June 2014 to March 2015 in Eloy, Arizona.

6.1 Benefits of In-Canopy Bleed Air Actuation

Modern autonomous airdrop systems are designed to mimic that of human skydivers and parachutists in not only their decision making ability and path planning strategies but also in their physical construction. Much like human pilots that use only their arms (and, in some cases, their feet) for steering while suspended from the parafoil canopy rigging, large scale autonomous systems feature a central autonomous guidance unit (AGU) containing all of the required sensory and computational hardware, actuators, and batteries necessary for executing autonomous flight. Figure 6.1 provides a front view illustration of a large scale fully autonomous parafoil aircraft during flight.

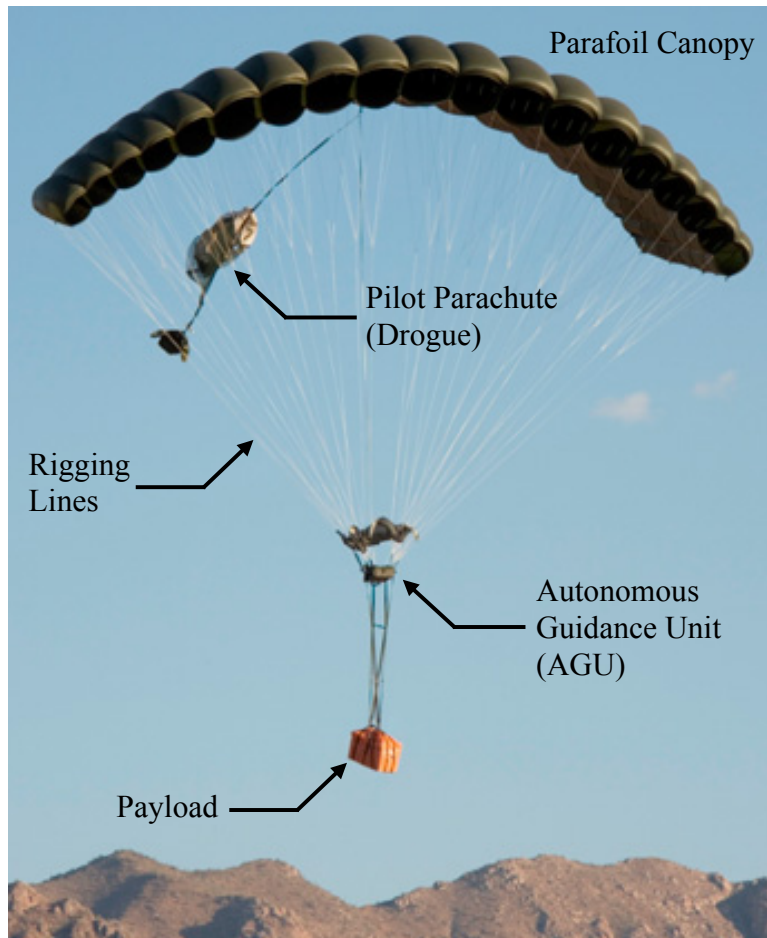


Figure 6.1: Large scale autonomous parafoil and payload system in flight (front view). [12]

Similar to human pilots, the AGU is located below the parafoil canopy and serves to steer the vehicle during flight by operating one or more electric winch actuators connected to several control lines attached to various points on the parafoil canopy surface. All previous realizations of bleed air control mechanisms include several control lines that run from each bleed air opening down through the lower surface of the parafoil canopy before joining and connecting to one or more winch actuators located on the payload or within the system AGU. This configuration is shown in Figure 6.2. In practice, this actuation strategy is similar to that of conventional trailing edge brake deflection and most compatible with existing airdrop hardware where control line attachment points are simply moved from the canopy trailing edge to the upper surface bleed air opening.

However, autonomous systems are in no way restricted to operate within these physical constraints. In terms of currently fielded systems, a large portion of size,

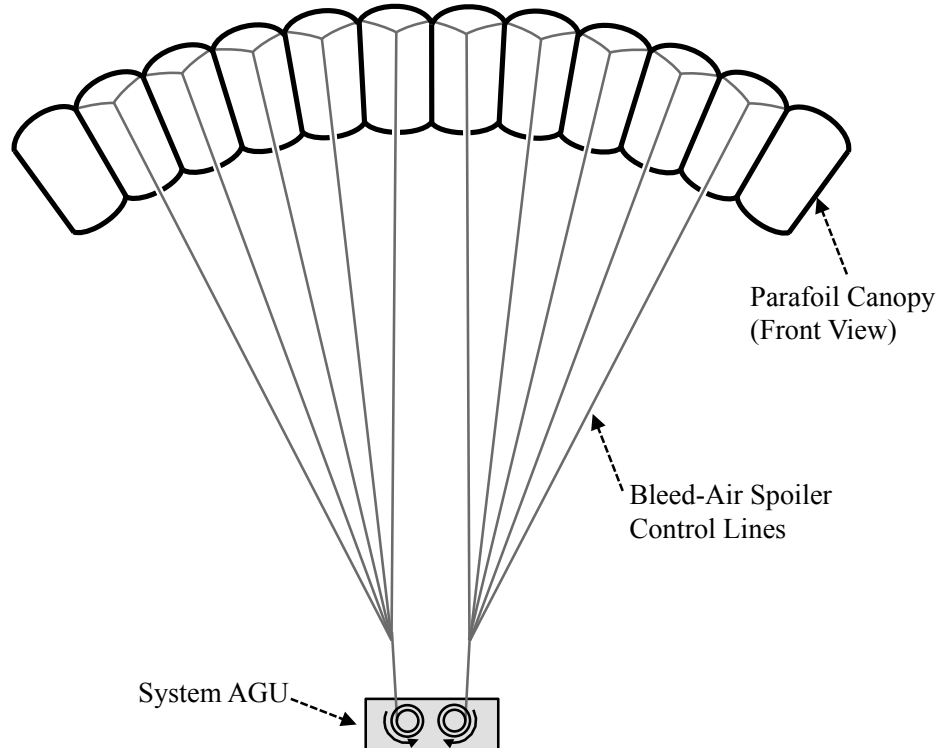


Figure 6.2: Canopy front view showing spoiler actuation from system AGU.

weight, and cost of the AGU is dedicated to electric winch actuators and batteries in order to meet the significant torque and power requirements needed to deform large portions of the canopy trailing edge for control. However, one unique feature of bleed air control is that it requires considerably less actuation force to open the upper surface vents. This comes in large part due to the fact that only small portions of the upper canopy surface are deformed during opening of the bleed air vents. As a result, significant savings in size, weight, and cost of the actuators are possible through the use of upper surface canopy spoilers. Moreover, given the significant reduction in force needed to open the upper surface vents, elimination of the AGU altogether in favor of much smaller actuators mounted entirely within the canopy is now possible.

The idea of transitioning from a more conventional payload borne actuation scheme to one utilizing several smaller actuators mounted entirely within the parafoil canopy is completely uncharted territory for autonomously guided parafoil and payload aircraft. However, several unique advantages to this concept of in-canopy bleed air actuation are worth mentioning. First, without the need for a complicated network of control lines extending from the AGU to various points on the canopy surface, the packing and rigging procedure for such systems is greatly simplified. Although the general responsibility of packing each canopy for a safe and reliable opening is largely unchanged, the extra time and effort spent ensuring that all control lines are clear and free of all possible obstructions during opening is significantly reduced noting that each in-canopy actuator is completely contained within its own cell and essentially isolated from all other parts of the system. Also, the risk of snagging or tangling control lines as the system tumbles during opening is much lower for similar reasons. Second, increased vehicle control authority and improved landing accuracy through lateral and longitudinal control is no longer dependent on the added cost, complexity, and weight associated with more conventional mechanisms (e.g. variable

canopy incidence angle control). As shown previously, upper surface canopy spoilers provide excellent lateral and longitudinal control through both asymmetric and symmetric opening providing a much more practical and efficient mechanism for improving landing accuracy. Any weight savings in the physical control mechanism are put directly into increasing the total payload capacity of the system. Finally, each in-canopy actuator can be individually opened or closed providing an increased number of control channels to the onboard guidance algorithm as opposed to conventional two channel approaches. Additionally, an increased level of robustness to actuator failure exists in systems employing multiple in-canopy actuators for control. In this case, loss of one or more actuators may degrade turning performance in one direction but does not necessarily prevent turning in that direction all together.

6.2 In-Canopy Hardware Description

The following sections discuss the design and development of an in-canopy bleed air actuation system. Mounting and rigging considerations of the actuator within the parafoil canopy and an overview of the actuator itself and associated hardware is described. Development of the payload communication relay box and ground station user interface necessary to control each actuator is also presented.

6.2.1 Actuator Mounting and Rigging

In order to relocate the winch actuators from the AGU to within the parafoil canopy, two primary issues must be addressed including where to position the actuators within the canopy and how to route the control lines in order to achieve the required vertical displacement of the upper surface bleed air opening. Figure 6.3 illustrates the selected configuration where the in-canopy actuator is secured to the parafoil canopy at the intersection of the structural rib and lower canopy surface at the point where the rigging line attachment point is located. Note those areas on the lower surface nearest rigging line attachment points are considered hard points within the canopy and

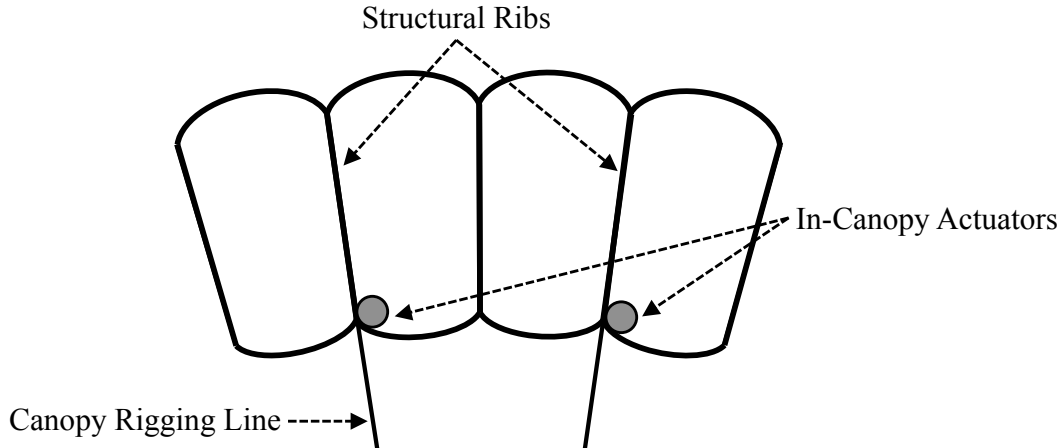


Figure 6.3: In-canopy actuator mounting configuration (front view).

provide the most rigid foundation for securing hardware.

Control lines are routed by first exiting the actuator and running directly up to the bleed air slit where it passes through a small ring attached to the leading edge side of the opening before running back down and terminating at the intersection between the adjacent structural rib and lower surface. As the actuator reels in line, the ring attached to the bleed air opening is subsequently pulled downward as the tension in the control line increases. Similarly, as the actuator releases or reels out control line, the internal pressure within the cell and spanwise tension in the canopy forces the bleed air opening closed thus sealing off any further airflow to the outside. This configuration is further detailed in Figure 6.4.

One advantage to routing the control lines in this configuration is that line tension is distributed equally between adjacent structural ribs minimizing any deformation of the lower surface; however, more line is displaced in this configuration in order to achieve the same vertical movement of the bleed air opening than by simply pulling down from a single control line. Adjacent cells can also be actuated using only one in-canopy actuator fitted with two control lines as shown in Figure 6.4. In this case, a single hole in the structural rib nearest the in-canopy actuator is added allowing the

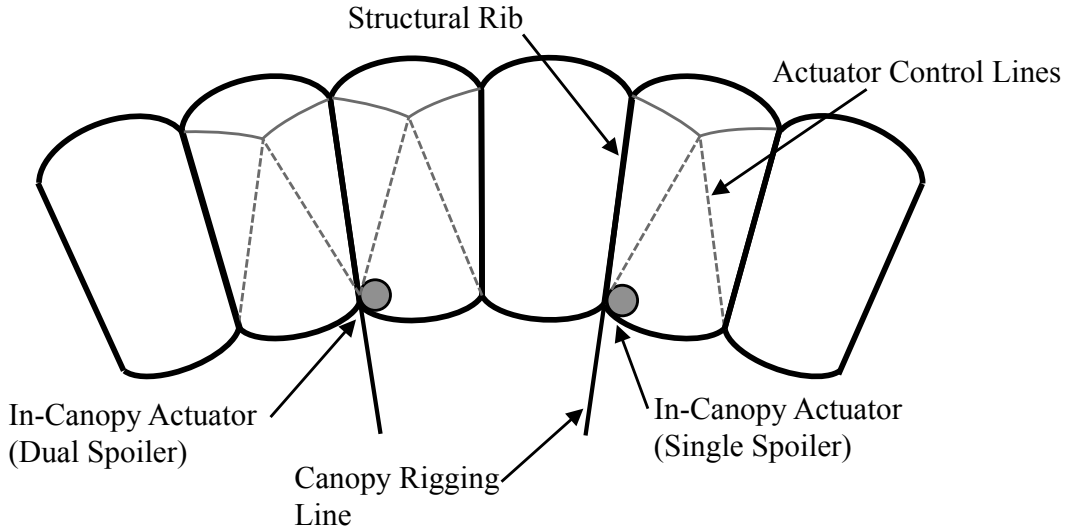


Figure 6.4: In-canopy actuator control line routing for signal spoiler and dual spoiler configurations.

second control line to pass through to the adjacent cell. Dual spoiler configurations are beneficial for canopies with equal cell sizes across the entire span in that it reduces the number of required in-canopy actuators by a factor of two.

6.2.2 Detailed Actuator Design

The key component of the in-canopy actuation system is the servo winch actuator itself. Designed for robust operation with minimal size and weight, the in-canopy actuator is comprised of a single cylindrical tube housing all internal components including a brushed DC gear motor, control line spool and bearing, battery pack, wireless transceiver, and motor driver electronics. In order to minimize the overall footprint of each actuator, all components are designed to be mounted within a thick walled cylindrical tube. Rounded end caps are also added to minimize the possibility of sharp edges tearing through the canopy fabric during packing or opening of the parachute. An exploded view of the prototype in-canopy actuator is shown in Figure 6.5.

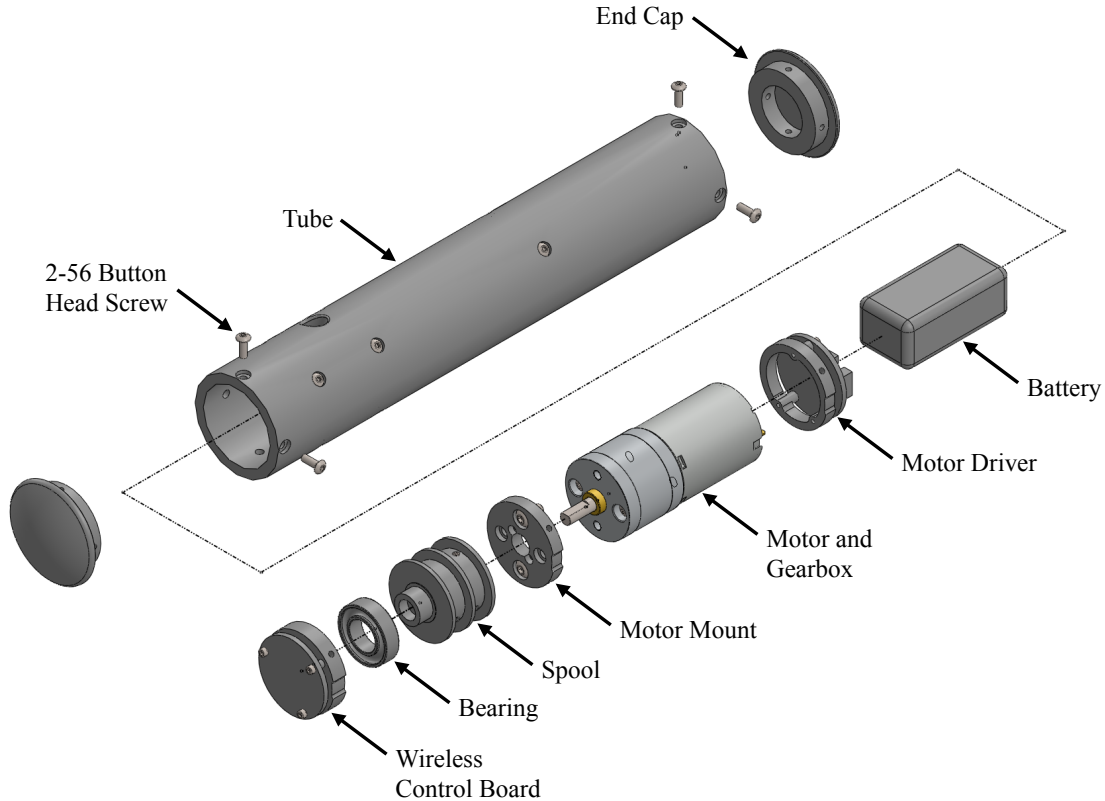


Figure 6.5: In-canopy actuator exploded component view.

The outer tube and nearly all of the internal components within the actuator, excluding motor, gearbox, and necessary electronics, are machined from Delrin[®] (acetal polymer) for high strength with minimal weight. The overall size of the in-canopy actuator is 7.25 inches in length with an outside diameter of 1.25 inches. The total weight is 8.0 oz. Small fasteners oriented along the radial direction of the outer tube are used to secure the internal components and end caps in place. All external screws are button head type with counter-bored holes to ensure a flush fit with the outer surface of the actuator body. Six larger fasteners are used to secure the actuator inside the canopy – three through the structural rib and three through the lower canopy surface. To reinforce the actuator attachment point within the canopy, a small section of high strength fabric is first sewn in place followed by six #0 grommets. Figure 6.6 shows the in-canopy actuator installed within an MC-4/5 canopy prior to packing.



Figure 6.6: In-canopy actuator mounted within MC-4/5 parachute prior to flight test.

The actuator spool is constructed from ABS plastic using a rapid prototyping machine and features two independent tracks, each with an inner diameter of 0.75 inches, enabling actuation of either one or two bleed air spoilers at once. Additionally, a single ball bearing is added to the end of the spool opposite the motor for support preventing the motor gearbox from binding under load. Absolute positioning of the motor spool relative to the actuator housing is achieved using a non-contact, digital magnetic encoder (Avago AEAT-6600-T16) and a small diametrically polarized Neodymium-Iron-Boron (NdFeB) magnet embedded in the end of the spool nearest the bearing. As the spool rotates, the change in orientation of the magnetic field is sensed by the encoder chip and subsequently converted to an equivalent change in angular position.

Two different brushed DC gearmotors, each shown in Figure 6.7, were tested and used within the in-canopy actuator. Catalog specifications of each motor are listed in Table 6.1. Initially the smaller 12 mm diameter motors were used in all flight tests from June 2014 through November 2014. However, these motors were found to repeatedly fail during use from either over temperature or broken gear teeth and were later replaced in January 2015 with the larger 25 mm diameters motors to improve actuator reliability and performance.

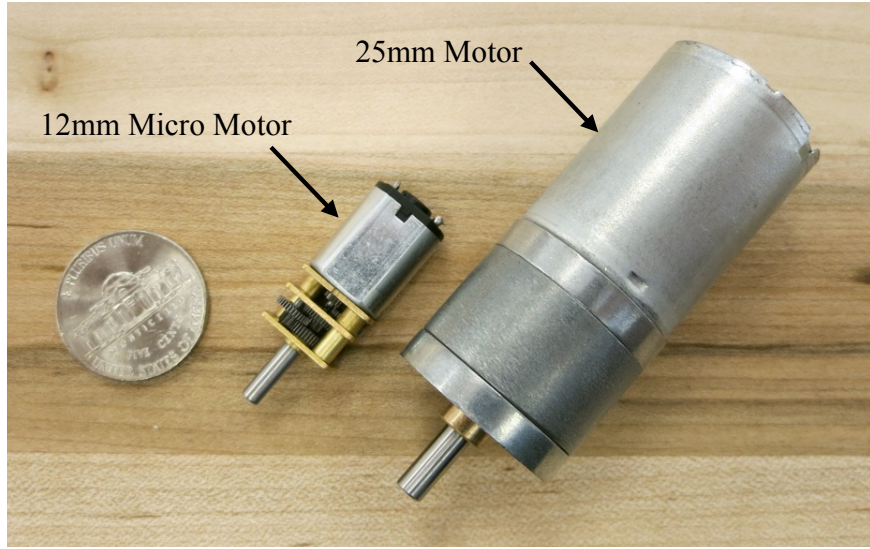


Figure 6.7: In-canopy actuator motor comparison.

Table 6.1: In-canopy actuator motor catalog specifications.

	12 mm Micro Motor 1	12 mm Micro Motor 2	25 mm Motor
Gearbox Ratio	250:1	298:1	99:1
Stall Torque @ 6V (oz-in)	60	70	160
Stall Current @ 6V (amp)	1.6	1.6	6.0
Free Run Speed (RPM)	120	100	100
Body Diameter (mm)	12	12	12
Overall Length (mm)	24	24	54
Weight (oz)	0.34	0.34	3.2

Although the larger 25 mm motors are more than 10 times the weight of the 12 mm micro motors, the measured performance of each motor in terms of free run speed and stall torque are very similar at relatively low values of motor winding current. Figure 6.8 shows the results of a series of bench tests where motor stall torque is measured as a function of winding current. Note for winding currents less than 1.2 amps, the measured stall torque from each motor is nearly identical. However, significantly diminishing returns in stall torque with increasing winding current beyond 1.2 amps are noted for the 12 mm motor. Not directly indicated in Figure 6.8, winding current in excess of 1.2 amps quickly exceeds the maximum

allowable temperature rise in the 12 mm motors resulting in permanent damage. Alternatively, the 25 mm motor is significantly larger and capable of delivering nearly 100 oz-in of torque at 3 amps with minimal change in winding temperature. As a result, the added weight from the 25 mm motor is deemed acceptable given the increased torque, current capacity, and gearbox rigidity.

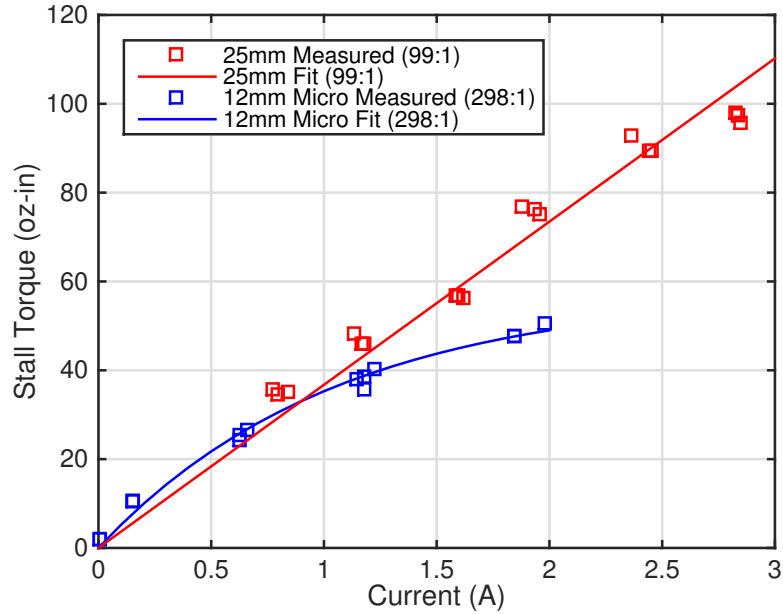


Figure 6.8: Motor torque vs. winding current.

Motor control and wireless communication electronics inside the actuator are distributed across two custom printed circuit boards (PCB) and connected via a short 6-conductor jumper wire. Each circular PCB, shown in Figure 6.9, is 1 inch in diameter with surface mount components on either side. The microprocessor selected for the in-canopy actuator is a Texas Instruments 16-bit MSP430F5510 featuring dedicated hardware peripherals including 10-bit analog to digital conversion, I²C and SPI communication, and PWM generation. Low power wireless communication is enabled using a Nordic nRF24L01+ 2.4 GHz wireless transceiver. Given the space constraints within the actuator body, a basic quarter-wave wire monopole antenna with micro coaxial connection is used providing up to 50 feet of consistent communication range. The motor driver used to control the speed and direction of the actuator motor is a

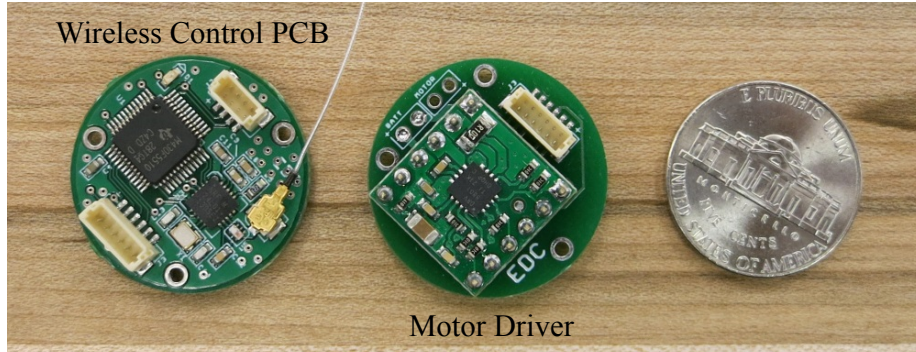


Figure 6.9: In-canopy actuator electronics.

Texas Instruments DRV8801 capable of switching up to 2.8 amps. Electrical power for the in-canopy actuator is provided from a 2-cell, 7.4 V lithium-polymer (LiPo) battery. Total capacity of the battery is 350 mAh or 2.59 Watt-hours.

6.2.3 Payload Relay Box and Ground Station Interface

Although each in-canopy actuator is equipped with a low-power wireless communication interface, individual deflection commands originate from a central transmitter attached to the system AGU. More specifically, this transmitter, termed the payload relay box, serves to relay spoiler deflection commands either computed locally or received from the ground station graphical user interface (GUI) to each individual actuator installed within the parafoil canopy. Housed inside the payload relay box are a microprocessor, GPS receiver and antenna, barometric pressure sensor, and two separate wireless communication interfaces. The first wireless interface is a 900 MHz XTend long range transceiver from Digi International for sending and receiving data from the ground station GUI. The second is a Nordic nRF24L01+ 2.4 GHz wireless transceiver enabling bi-directional communication with each individual in-canopy actuator. Non-volatile data storage including a 32Mbit EEPROM and micro SD card are included for logging data and storage of system configuration parameters. Figure 6.10 shows the payload relay box internal components and a picture of the system attached to the side of an MC-4/5 AGU prior to flight testing.



Figure 6.10: Payload relay box internal components (left) and mounted on MC-4/5 AGU (right) prior to test flight.

During flight, the 2.4 GHz wireless link between the payload relay box and each individual actuator serves to create a simple ad-hoc point-to-multipoint communication network. In order to avoid network data collisions and to prevent each actuator from operating on separate channels, each Nordic transceiver is configured with a 5-byte unique identifier or network address. Additionally, each Nordic transceiver provides the ability to enable automatic transmission retries and packet acknowledgments to further improve network communication robustness where acknowledgment packets contain up to 32 bytes of user-defined data instead of the traditional 1-byte ACK (NACK) response frame. The communication protocol adopted for transferring data between the payload relay box and each in-canopy actuator consists of two basic messages – (1) commanded spoiler deflections sent from the payload relay box to each in-canopy actuator and (2) the associated acknowledgement response frame containing 14 bytes of actuator telemetry data (i.e. actuator battery voltage, motor winding current, spool position, etc.). Although not strictly necessary, inclusion of actuator telemetry data with each acknowledgment frame provides a convenient method of analyzing actuator performance and debugging. Figure 6.11 provides an overview of the wireless network topology for an example parafoil system.

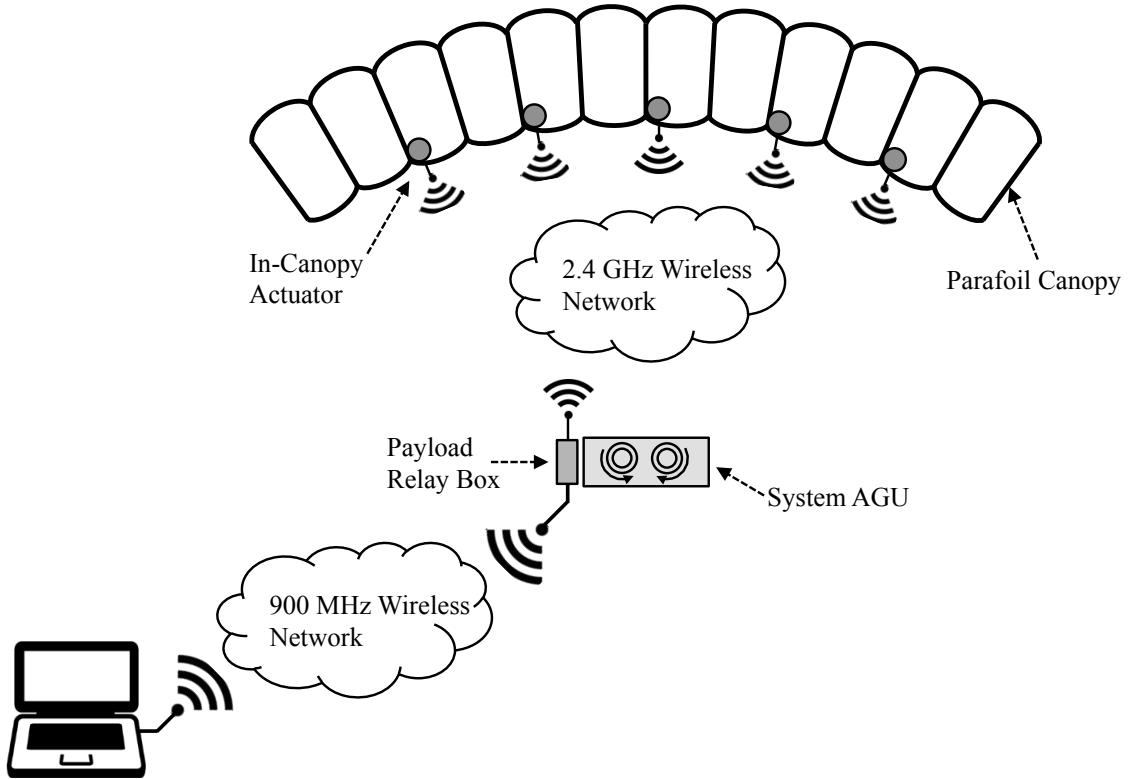


Figure 6.11: In-canopy actuation system wireless network topology.

The ground station GUI is designed to provide the user with a real-time view of the payload relay box telemetry data (GPS coordinates, altitude, ground speed, etc.) and a snapshot of the current state of all connected in-canopy actuators (battery voltage, motor current, spool position, etc.). During flight, the payload relay box microprocessor samples all sensors and gathers the latest data received from each in-canopy actuator and then broadcasts this information to the ground station interface in the form of a 1 Hz ping using the long range 900 MHz transceiver. Under manual operation, spoiler deflection commands specified by the user are sent to the payload relay box and subsequently retransmitted to each in-canopy actuator. The payload box can also be configured for fully autonomous operation where all spoiler deflection commands are computed locally via the internal microprocessor and sensing suite. Transitioning between manual or autonomous flight is controlled from the ground

station GUI and can be changed at any point during flight. Figures 6.12 – 6.14 provide screen capture images of each of the three tabs of the ground station GUI including Flight Control, Controller Gains, and Navigation/Guidance.

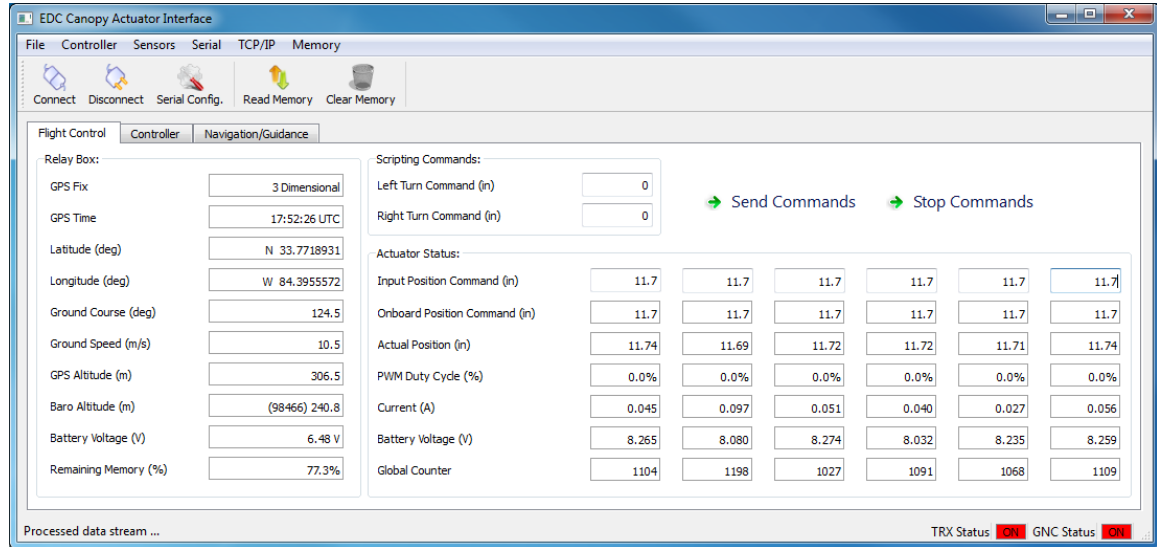


Figure 6.12: Flight control tab of ground station graphical user interface (GUI).

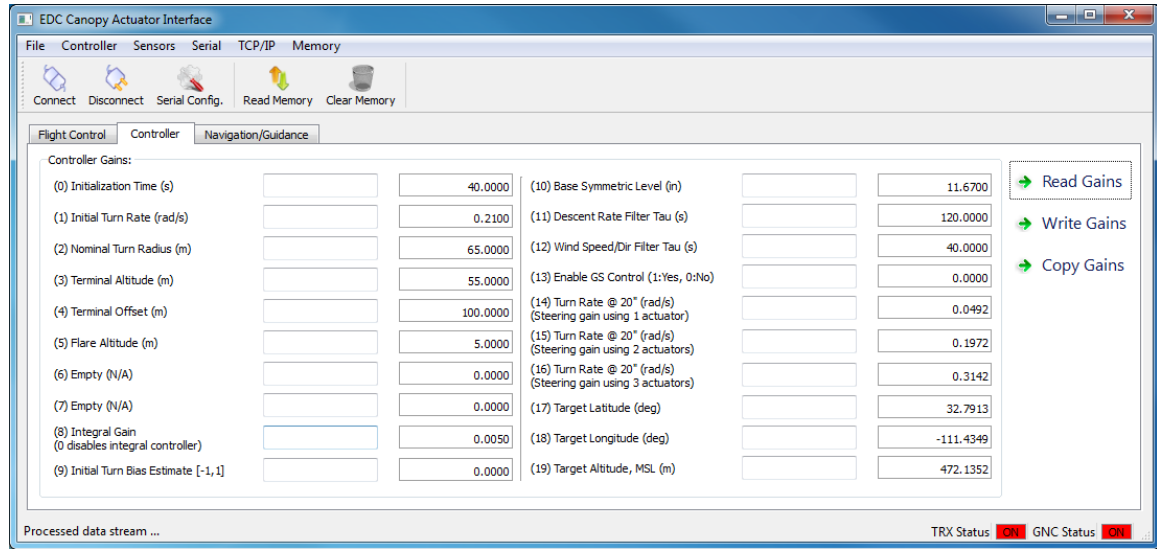


Figure 6.13: Controller gains tab of ground station graphical user interface (GUI).

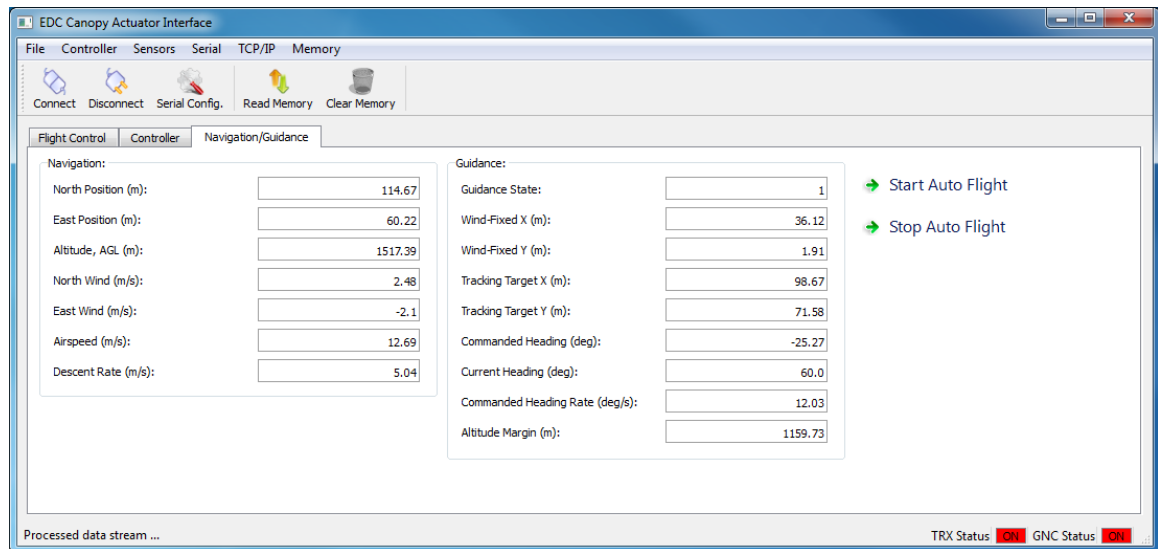


Figure 6.14: Navigation/Guidance tab of ground station graphical user interface (GUI).

CHAPTER VII

FLIGHT TESTING OF IN-CANOPY HARDWARE

In this chapter, a description of the large scale parafoil and payload aircraft used for all flight testing of the in-canopy bleed air actuation system is presented as well as a brief overview of the flight testing procedure and protocols associated with large scale autonomous aircraft. Additionally, steady-state lateral and longitudinal response of the vehicle to different combinations of spoiler openings is presented enabling both refinement of the parafoil and payload dynamic model and subsequent evaluation of the predicted autonomous landing performance using the in-canopy actuation system. In flight measurements of actuation force for different amounts of upper surface bleed air vent deflection are also documented. Lastly, a simple approach for estimating the maximum expected in-canopy actuator loads given basic aerodynamic and geometric information of the canopy is presented.

7.1 Vehicle Overview and Flight Testing Protocol

The MC-4/5 parachute shown in Figure 7.1 is most notably a personnel parachute with a total surface area of 370 ft^2 . Total weight of the autonomous system including parachute, AGU, payload, and all in-canopy hardware is 376 lb resulting in a wing loading of just over $1.0 \text{ lb}/\text{ft}^2$. Note the AGU alone weighs 35 lb [58] while all in-canopy hardware including six actuators and the payload relay box weighs just under 4 lb — a reduction in total weight of the actuation hardware by nearly 10 times over conventional trailing edge control. Also shown in Figure 7.1 is a view from inside one of the canopy cells during flight captured using a remote video camera system. The inset image in Figure 7.1 depicts the in-canopy actuator mounting and control line rigging near maximum deflection of the upper surface spoiler opening.

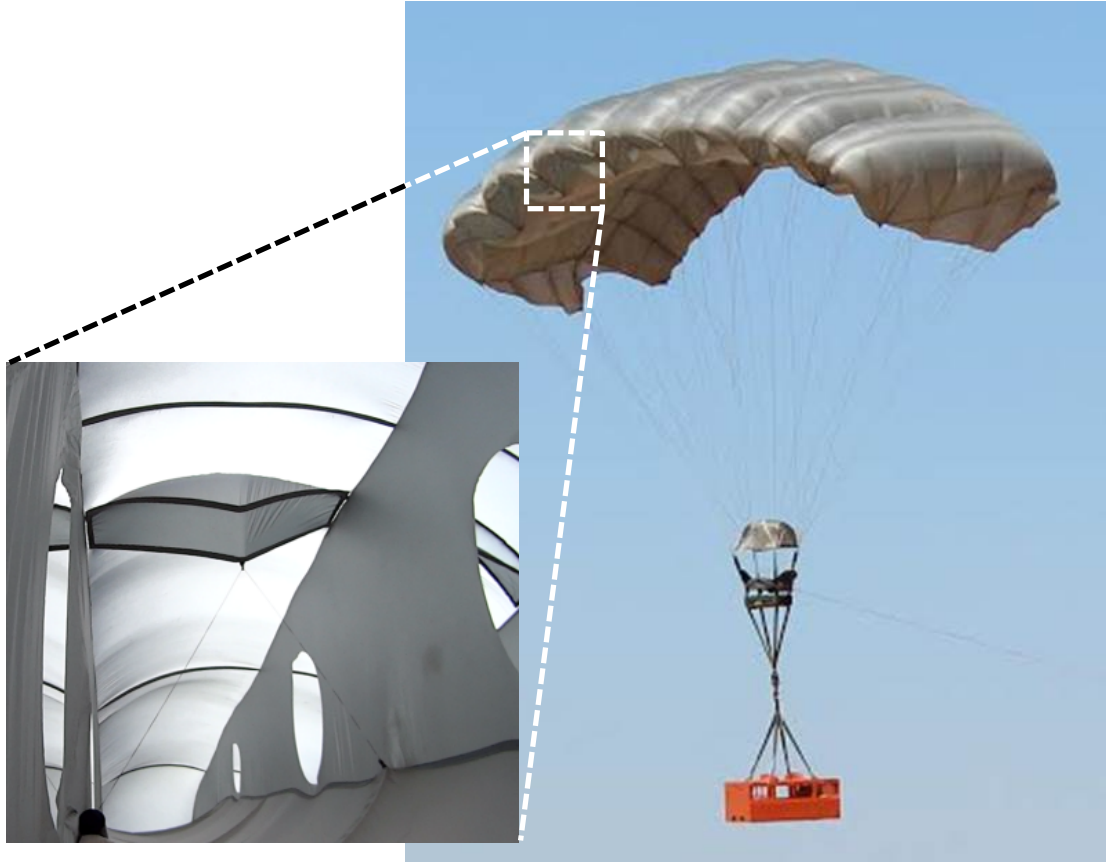


Figure 7.1: MC-4/5 parafoil canopy in flight and internal view of in-canopy actuator.

In total, six in-canopy actuators are integrated into the MC-4/5 canopy as shown in Figure 7.2 providing the capability to actuate at most 10 upper surface spoiler openings. The shaded gray regions seen in Figure 7.2 indicate those cells with upper surface spoiler openings. Note the two outer actuators are configured to open only one bleed air vent in order to prevent the outer cells on either wingtip from collapsing during flight. The other four actuators in the center of the canopy are configured for dual spoiler operation.

The flight testing protocol for the MC-4/5 system using in-canopy actuators is largely identical to that for any autonomous parafoil aircraft in that the canopy is first packed and later secured to the proper weight payload before being loaded onto the aircraft. However, all in-canopy actuators and associated control lines must be secured within the canopy and powered prior to packing of the parachute. Once powered, the

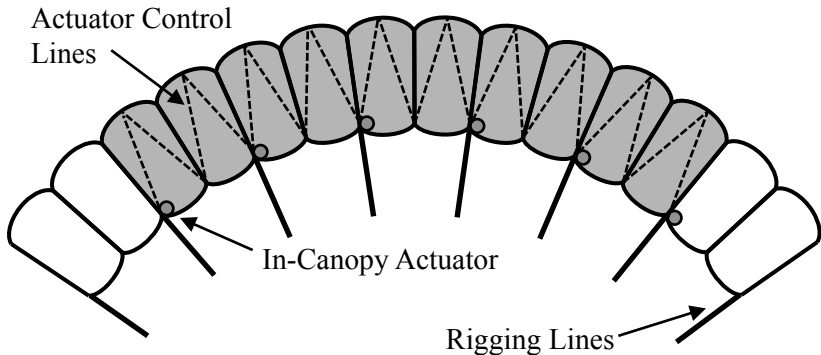


Figure 7.2: MC-4/5 in-canopy actuator configuration (canopy front view).

in-canopy actuators automatically enter a low power idle state in order to conserve battery capacity. Upon exiting the parent aircraft, the parachute is allowed to fully inflate while the AGU completes its standard initialization. Following initialization, the AGU flight software is then transitioned to manual control with zero deflection of the trailing edge. At this point, the system is under complete control from the in-canopy actuators and capable of executing manual scripts via the ground station GUI or fully autonomous flight using the payload relay box microprocessor and internal sensing suite. It must be noted that all trailing edge brake control lines were left in place for safety thus maintaining the ability to fly the system autonomously or from manual control using the AGU.

During this low power idle state, all actuators are designed to periodically activate the 2.4 GHz wireless transceiver for a short time (~ 300 ms) in order to detect incoming deflection commands from the payload relay box. Actual time between listening for incoming data is approximately 3 s for a total period of 0.303 Hz. If any deflection commands are successfully received before the 300 ms sampling window expires, the actuator immediately resumes normal operation and the motor and spool are subsequently moved to the commanded position. Otherwise, all components remain in low power idle state and the cycle is continuously repeated. Additionally, if wireless communication from the payload relay box stops for more than 10 seconds, each actuator

immediately returns to this low power idle state keeping the motor and spool at the last commanded position. Note all in-canopy actuators are capable of being powered and packed within the parachute several days prior to use.

7.2 Control Authority Using In-Canopy Hardware

Initial flight testing of the in-canopy bleed air spoiler actuation system began in June 2014 in Eloy, Arizona, with the goal of verifying not only the actuator mounting design and survivability of all associated hardware, but also the ad-hoc wireless communication scheme between the ground station GUI, payload relay box, and each individual in-canopy actuator. As of March 2015, over 30 flight tests have been conducted using the in-canopy bleed air actuation system with excellent results. Each subsequent test has continued to advance the performance and robustness of the in-canopy hardware with the ultimate goal of developing a reliable and effective alternative to bleed air control using payload centric actuators.

One prerequisite to properly identifying vehicle flight characteristics is accurate knowledge of the expected range of travel for each spoiler opening using the in-canopy actuators. Often the inflated geometry of a parachute varies significantly from the “cut” patterns used during its construction making it considerably difficult to identify the proper control line length. Accordingly, Figure 7.3 shows several frames taken from the remote video footage from inside one of the MC-4/5 cells during flight where the spool deflection of the in-canopy actuator is slowly incremented from 4 inches to 14 inches in order to pinpoint the exact control line length with zero slack. Note 61 inches of control line extends from the actuator body at zero deflection where each increment shown in Figure 7.3 represents the linear distance of control line taken up (i.e. shortened) by the actuator. At approximately 7 inches deflection (54 inches of control line extended from the actuator), the control line is taut with no visual indication the upper surface bleed air vent is open. For deflections beyond 7 inches,

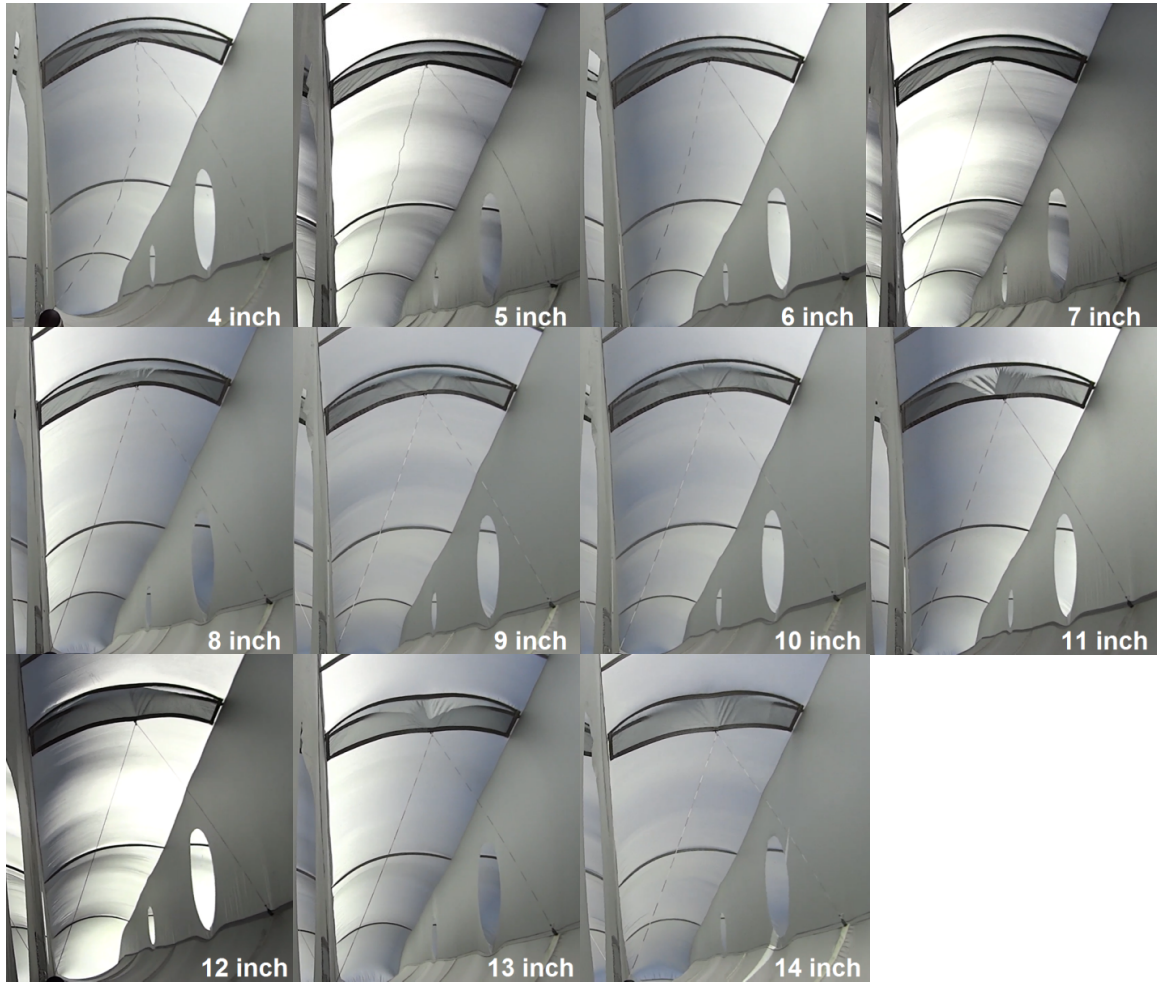


Figure 7.3: MC-4/5 control line slack measurement.

the upper surface vent is clearly deforming under the increased control line tension allowing the internal ram air from within the cell to begin flowing to the outside of the canopy.

Additionally, it must be noted that all deflection values from this point onward refer exclusively to vertical displacement of the upper surface opening as opposed to linear control line displacements measured at the actuator. Note zero vertical deflection represents the fully closed configuration with positive deflection values corresponding to increased opening of the upper surface vent. This convention is illustrated in Figure 7.4 where Δh represents the vertical displacement of the upper surface bleed air vent from its fully closed position. Equations (7.1) – (7.3) detail the conversion from

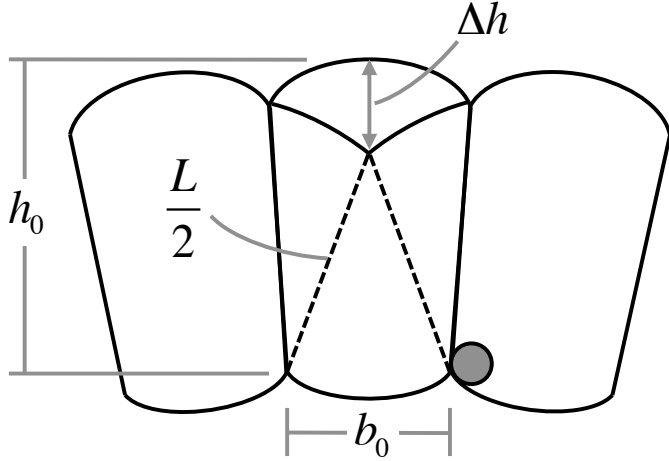


Figure 7.4: MC-4/5 inflated cell measurements.

linear control line displacements measured at the actuator to vertical displacement of bleed air vent Δh

$$\Delta h = h_0 - 0.5\sqrt{(L)^2 - (b_0)^2} \quad (7.1)$$

$$h_0 = 0.5\sqrt{(L_0 - x_0)^2 - (b_0)^2} \quad (7.2)$$

$$L = (L_0 - x_0) - x \quad (7.3)$$

where h_0 and b_0 are the inflated MC-4/5 cell height and width, respectively, L_0 is the nominal control line length of 61 inches, x_0 is the estimated zero slack actuator deflection of 7 inches, and x is the additional actuator deflection beyond the zero slack point. In practice, all data is logged according to the measured linear displacement of the actuator spool and later post-processed to an equivalent vertical displacement of the upper surface bleed air vent.

7.2.1 Lateral Control Authority

A series of system identification flights are performed with the MC-4/5 system in an effort to quantify the lateral turning performance using in-canopy bleed air actuators. For each test flight, several different combinations of asymmetric spoiler openings are commanded and held constant allowing the vehicle to complete at least one full turn for accurate wind estimation. Figure 7.5 shows the estimated vehicle turn rate as a function of vertical displacement of the upper surface vent for three different asymmetric spoiler configurations. Each asymmetric configuration is further detailed in Figure 7.6. Note the one shaded blue cell corresponds to using only the furthest outboard in-canopy actuator for steering where the resulting turn rates and linear fit line are also shown in blue in Figure 7.5. Similarly, the three shaded red cells correspond to using two outboard in-canopy actuators while the five shaded gray cells correspond to using all three actuators on one side of the canopy centerline.

Maximum turn rate is approximately 18 deg/s using three in-canopy actuators and well above the typical turn rate limits of ± 15 deg/s for autonomous flight. Note that

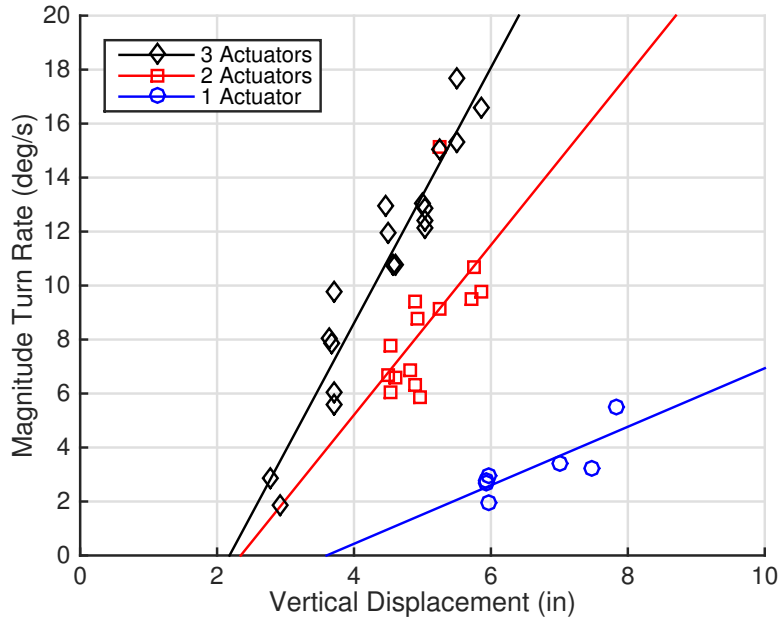


Figure 7.5: MC-4/5 turn rate during flight test using in-canopy actuators.

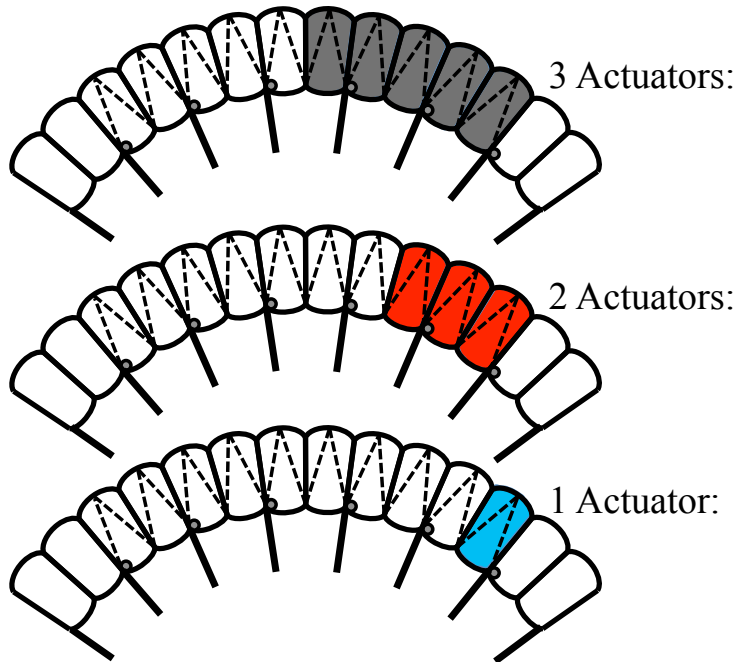


Figure 7.6: Asymmetric spoiler configurations during MC-4/5 flight test.

measured vehicle turn rates are very linear and symmetric with respect to both left and right turns such that all data shown in Figure 7.5 is simply turn rate magnitude. As expected, vehicle turn rate also decreases when actuating fewer bleed air openings with an equivalent vertical displacement. Lastly, a significant deadband exists in the vehicle turn rate response where just over 2 inches of vertical displacement is needed before any measurable turn rate is detected. Existence of this turn rate deadband is likely the result of small displacements separating only the sealing flap from the canopy upper surface without actually opening the bleed air slit. Consequently, vertical displacements beyond 2 inches are needed before the upper surface vent actually opens creating a path for high pressure air to exit the cell. Aside from steady-state turn rate response, transient turn rate dynamics using upper surface spoilers were observed to be relatively quick (i.e. time constants on the order of several seconds or less) and largely equivalent to that using conventional trailing edge brakes. Additionally, no instabilities were observed during test flights including excitation of the vehicle dutch roll mode.

7.2.2 Longitudinal Control Authority

For each steady-state turn rate shown in Figure 7.5, an associated horizontal airspeed, descent rate, and glide ratio is computed and subsequently shown in Figure 7.7. Note all velocity values are scaled to their indicated (i.e. sea-level) equivalent. In contrast with the steady-state longitudinal response data shown for the small scale parafoil and payload test vehicle, all data in Figure 7.7 is presented as a function of measured vehicle turn rate as opposed to symmetric spoiler deflection providing a common metric for comparison regardless of the asymmetric spoiler configuration used throughout the turn. It must be noted that only periods of constant asymmetric

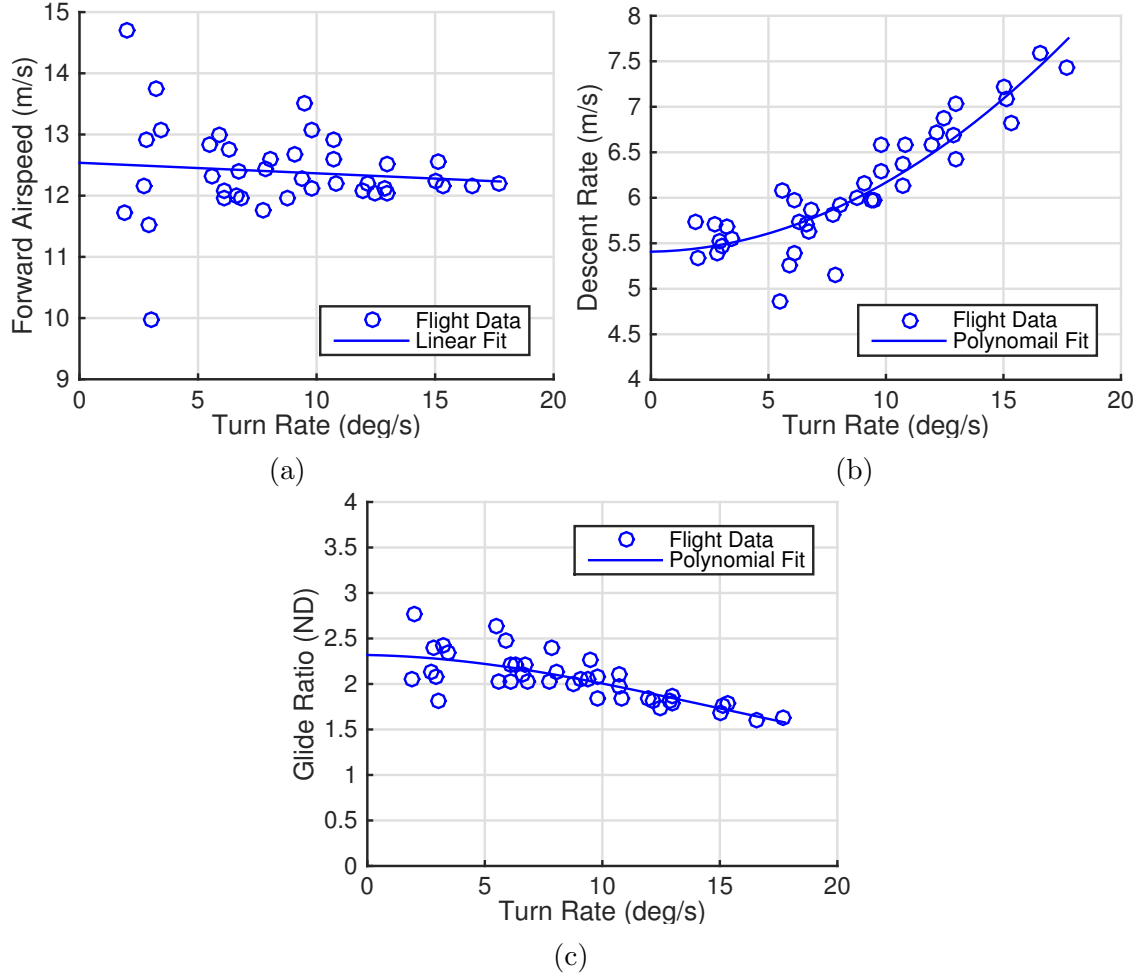


Figure 7.7: MC-4/5 steady-state flight characteristics using in-canopy bleed air actuators versus turn rate including: (a) airspeed, (b) descent rate, and (c) glide ratio.

spoiler openings are used for all MC-4/5 system identification testing in order to improve wind and airspeed estimation. Accordingly, Figure 7.7a shows the increased uncertainty in airspeed estimates for relatively low turn rates or nearly straight flight where data spanning only a limited range of heading angles is captured. This increased uncertainty is characterized by significantly higher variation in estimated forward airspeed from the expected linear fit.

As shown in Figure 7.7b, significant variation in vehicle descent rate is observed with increasing turn rate ranging from a nominal value of 5.5 m/s to nearly 8 m/s at 18 deg/s turn rate. Note the maximum asymmetric spoiler configuration of the MC-4/5 using in-canopy actuators (i.e. \sim 18 deg/s) involves opening only half of the total number of bleed air spoiler openings. As a result, even higher changes in descent and glide slope are expected when all 10 upper surface bleed air vents are symmetrically opened. Nevertheless, Figure 7.7c shows nearly a 35% decrease in vehicle glide slope during turning flight indicating significant lateral and longitudinal control authority of the vehicle. Although additional system identification flights are needed to fully quantify the transient vehicle response to symmetric spoiler opening, the observed vehicle dynamics are again relatively quick with no observed instabilities or apparent excitation of the phugoid or short period mode.

7.3 In-Canopy Bleed Air Actuation Force Study

As previously discussed, reduced actuator loads inherent to the upper surface bleed air spoiler control mechanism are fundamental to the idea of in-canopy actuation. However, accurate knowledge of the maximum expected actuation loads during flight is needed to properly size the in-canopy actuators for any arbitrary canopy. If the in-canopy actuators are undersized and unable to fully open the upper surface bleed air opening, lateral and longitudinal control of the vehicle is severely compromised thus sacrificing landing accuracy. However, if the in-canopy actuators are oversized

for their application, the structural integrity of the canopy is significantly at risk in addition to unnecessary weight, size, and cost of the actuation hardware.

For each flight with the MC-4/5 system using in-canopy actuators, motor current and position from each individual actuator is logged in order to reconstruct the relationship between actuator torque and vertical displacement of the upper surface bleed air opening. Noting the torque-current relationship from previous bench testing of the actuator motors shown in Figure 6.8 and the inflated cell measurements of the MC-4/5 canopy shown in Figure 7.4, Figure 7.8 shows the resulting vertical actuation force as a function of vertical displacement of the upper surface bleed air opening. Note the values of vertical actuation force shown in Figure 7.8 represent the combined vertical component of the actuation force acting at the center of the bleed air opening and not the control line tension itself.

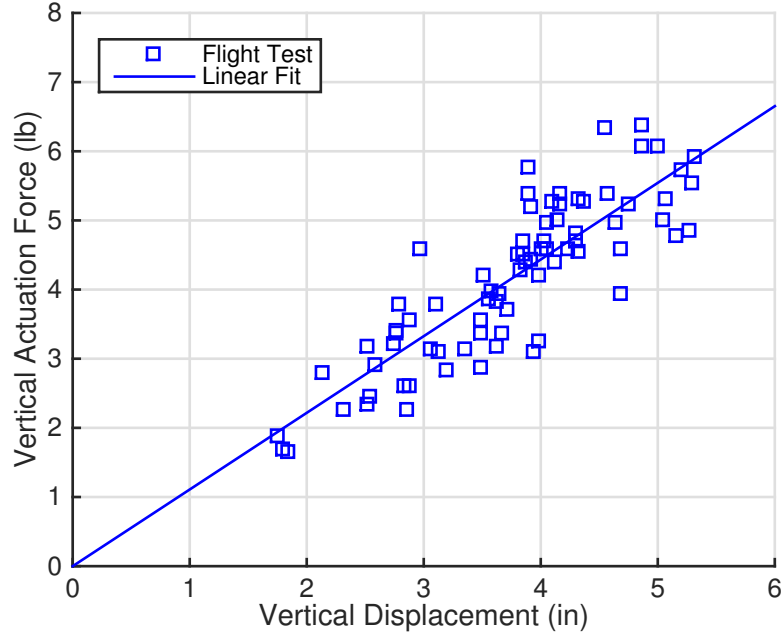


Figure 7.8: Vertical actuation force vs. vertical displacement of the upper surface spoiler opening using in-canopy actuators.

As shown in Figure 7.8, vertical actuation force is approximately linear with vertical displacement of the bleed air opening. Although these measurements are valid only for this specific vent geometry, it is interesting to note that actuation of the upper

surface spoiler is analogous to that of an equivalent linear spring constant where the actuator works against the pressure differential between the internal ram air within the canopy cell and the airflow across the upper surface. Note the equivalent spring constant K_{eq} is computed as 1.109 lb/in resulting in a maximum vertical actuation force of 6.65 lb at 6 inches vertical deflection.

With a good understanding of the maximum vertical actuation force observed during flight, a simple expression relating this maximum force to basic aerodynamic and geometric properties of the canopy is derived. First, careful observation of the in-canopy video footage showing the upper surface bleed air spoiler during opening suggests the shape of the displaced canopy surface area closely approximates that of a semicircle with diameter equal to the canopy individual cell width at maximum opening. This concept of displaced surface area is further depicted in Figure 7.9. Accordingly, a simple force balance is performed in which the maximum actuator load is computed as the product of the maximum displaced surface area and the estimated pressure differential across the upper surface bleed air opening. Although accurate estimation of the pressures on either side of the bleed air spoiler during opening is an extremely complex fluid dynamics problem, three very basic assumptions are employed including (1) internal and external pressures are constant across the entire

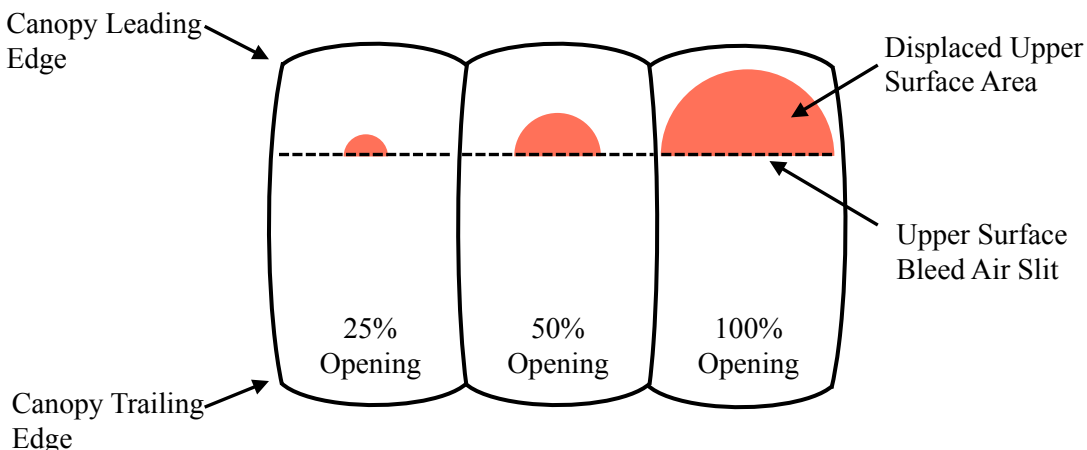


Figure 7.9: MC-4/5 turn rate during flight test using in-canopy actuators.

displaced canopy area, (2) internal pressure within the canopy is uniformly equal to the stagnation pressure given the expected airspeed of the system and (3) external pressure at the chordwise location of the bleed air opening ($0.25c$) is represented by some unknown pressure coefficient denoted C_p . Accordingly, the following equations provide a simple derivation of the expression predicting maximum vertical actuation force.

$$F_{max} = A_{max}\Delta P \quad (7.4)$$

$$= \frac{\pi}{8}b_0^2 \left[\left(P_\infty + \frac{1}{2}\rho V_\infty^2 \right) - \left(P_\infty + C_p \frac{1}{2}\rho V_\infty^2 \right) \right] \quad (7.5)$$

$$= \frac{\pi}{16}b_0^2\rho V_\infty^2 (1 - C_p) \quad (7.6)$$

Note the estimated airspeed and canopy cell width of the MC-4/5, denoted V_∞ and b_0 , respectively, are 13.66 m/s and 22.5 inches (57.15 cm). By solving equation (7.6) for the unknown pressure coefficient, a value of C_p equal to -1.02 is computed with F_{max} equal to 6.65 lb (29.58 N). Note a value of -1.02 is very reasonable given the typical pressure distribution across similar airfoil cross-sections (Clark-YM-15, NACA 4412, etc.). Although additional flight testing is needed to validate the above expression, equation (7.6) provides a very basic formula for quantifying the maximum expected vertical actuation force required to fully open the upper surface bleed air spoiler for any arbitrary canopy given expected flight speed and individual cell width.

CHAPTER VIII

IN-CANOPY AUTONOMOUS LANDING PERFORMANCE

In this chapter, autonomous landing performance of a large scale parafoil and payload aircraft equipped with in-canopy bleed air actuators is investigated in both simulation and experimental flight tests. First, Section 8.1 describes two changes to the parafoil and payload dynamic model enabling accurate representation of the aerodynamics associated with opening and closing each upper surface bleed air vent and the in-canopy actuator motor dynamics under load. Next, Section 8.2 discusses lateral steering and longitudinal control strategies using in-canopy actuators including specific details regarding the estimated range of turn rate and glide slope control for the MC-4/5 system. Section 8.3 presents autonomous landing accuracy statistics for the MC-4/5 system using in-canopy actuators from a series of Monte Carlo simulations in a variety of atmospheric conditions. Lastly, Section 8.4 details several fully autonomous flight tests of the MC-4/5 system using in-canopy actuators from canopy opening to ground impact with excellent results.

8.1 Simulation Model Modifications

Although the basic 6 DOF equations of motion are identical to those presented in Chapter II, several changes to the aerodynamic coefficients are needed to accurately model the response of the MC-4/5 to various combinations of symmetric and asymmetric spoiler openings. Also, a detailed actuator model is added to increase model fidelity based on in-flight measurements of the required actuation force and the measured performance of the in-canopy actuator motors.

8.1.1 Canopy Aerodynamics

Similar to the small scale parafoil and payload system dynamic model, control inputs are realized through two different terms, namely asymmetric spoiler deflection δa where $\delta a \in [-1, 1]$, and symmetric spoiler deflection δs where $\delta s \in [0, 1]$. However, computation of both δa and δs is now different where instead of left and right spoiler deflections, denoted δl and δr , six individual inputs are used representative of the six individual in-canopy actuator deflections. Consequently, each in-canopy actuator deflection is denoted as δi_j where $\delta i_j \in [0, 1]$ and $j = 1, \dots, 6$. Note $j = 1$ corresponds to the in-canopy actuator located furthest outboard on the left wingtip with increasing subscripts moving across the canopy span toward the right wingtip. Figure 8.1 further details the location and naming convention for each in-canopy actuator.

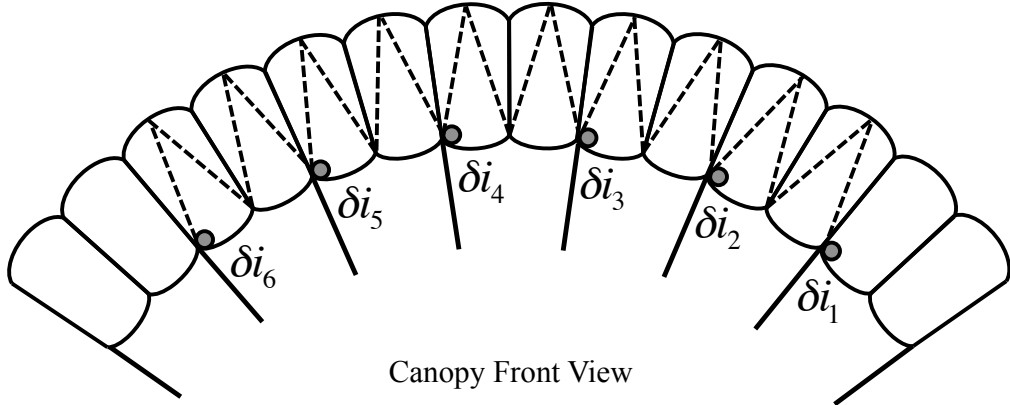


Figure 8.1: MC-4/5 in-canopy actuator location and naming convention.

As shown in Figure 7.5, the sensitivity of the MC-4/5 turn rate response to varying levels of asymmetric spoiler deflection is dependent on both the number of spoilers used during the turn and the effective moment arm or spanwise location of each open spoiler relative to the canopy centerline. Accordingly, equation (8.1) is used to compute total asymmetric spoiler deflection δa from a total of N individual in-canopy actuator deflections. Note that the total number of in-canopy actuators is assumed to be an even number.

$$\delta a = \sum_{j=1}^{N/2} \eta_j (\delta i_{N+1-j} - \delta i_j), \quad \sum_{j=1}^{N/2} \eta_j = 1.0 \quad (8.1)$$

For the MC-4/5 system using a total of six in-canopy actuators, the scaling coefficients η_1 , η_2 , and η_3 denote the relative contribution of the outboard, middle, and inboard actuators, respectively, to the overall asymmetric spoiler input. Additionally, the summation of all scaling coefficients is equal to 1.0 such that δa is restricted within its non-dimensional range of $[-1, 1]$. In order to match flight test data, values for η_1 , η_2 , and η_3 are chosen as 0.14, 0.50, and 0.36, respectively.

Total symmetric spoiler input, denoted δs , is similarly computed where the number of upper surface spoiler vents connected to each in-canopy actuator are used as weighting factors for each of the in-canopy actuator deflections. Here, the furthest outboard actuators on both wingtips are assumed to open only one vent while all others open two vents as shown in Figure 8.1. Again, δs is restricted within its non-dimensional range of $[0, 1]$ as shown below.

$$\delta s = \frac{1}{2(N-1)} \sum_{j=1}^{N-1} (\delta i_j + \delta i_{j+1}) \quad (8.2)$$

Using a procedure identical that employed for the small scale test vehicle and the modified expressions for asymmetric and symmetric control inputs shown in equations (8.1) and (8.2), a complete set of aerodynamic coefficients for the MC-4/5 system using in-canopy actuators is derived such that simulated vehicle response closely matches that observed in flight tests. A tabulated summary of all mass and geometric properties of the MC-4/5 system used within the simulation model is shown in Table 8.1. Additionally, Table 8.2 lists the values estimated for all MC-4/5 aerodynamic coefficients.

Table 8.1: MC-4/5 system geometric and mass properties.

Parameter	Value	Units
Canopy Span, b	8.69	m
Canopy Chord, c	3.96	m
Canopy Planform Area, S_c	34.4	m^2
Nominal Incidence Angle, Γ	-10.0	deg
Payload Area, S_p	0.5	m^2
Total Weight, m	170.6	kg
Wing Loading, m/S_c	4.96 [1.02]	kg/m^2 [lb/ft^2]
Inertia, I_{xx}	220.0	$\text{kg}\cdot\text{m}^2$
Inertia, I_{yy}	43.0	$\text{kg}\cdot\text{m}^2$
Inertia, I_{zz}	244.0	$\text{kg}\cdot\text{m}^2$
Inertia, I_{xz}	0.0	$\text{kg}\cdot\text{m}^2$
Apparent Mass, A	10.0	kg
Apparent Mass, B	30.0	kg
Apparent Mass, C	100.0	kg
Apparent Inertia, P	105.0	$\text{kg}\cdot\text{m}^2$
Apparent Inertia, Q	156.0	$\text{kg}\cdot\text{m}^2$
Apparent Inertia, R	42.0	$\text{kg}\cdot\text{m}^2$

Table 8.2: MC-4/5 system aerodynamic coefficient summary.

Coefficient	Value	Coefficient	Value
C_{L0}	0.0	C_{lp}	0.0
$C_{L\alpha}$	2.03	C_{lr}	-0.25
$C_{L\alpha^3}$	-5.55	$C_{l\delta a}$	0.0
$C_{L\delta s}$	-0.17	C_{mq}	-1.0
C_{D0}	0.16	C_{np}	-0.1
$C_{D\alpha^2}$	0.10	C_{nr}	-0.18
$C_{D\delta s}$	0.077	$C_{n\beta}$	0.0
$C_{Y\beta}$	-1.0	$C_{n\delta a}$	0.023
$C_{D,p}$	0.5		

A comparison of the dynamic model turn rate response with MC-4/5 flight test data is shown in Figure 8.2. Again, three different data sets are presented in which 1, 2, and 3 outboard actuators are used simultaneously throughout the turn. Note steady-state vehicle turn rate is determined numerically by integrating the dynamic

model forward in time until trim with zero atmospheric wind, constant (sea-level) air density, and constant control inputs. Vertical deflection of the upper surface spoilers have also been normalized over their effective range to both eliminate the existence of any steering deadband and limit the maximum opening of the upper surface spoilers. For the MC-4/5 system, $\delta_i = 0$ corresponds to a vertical displacement of 2.18 inches while maximum opening ($\delta_i = 1.0$) corresponds to a vertical displacement of 6.0 inches leading to a maximum turn rate of nearly ± 18 deg/s. As shown in Figure 8.2, the simulation model closely matches the turn rate response observed in flight tests indicating good model agreement.

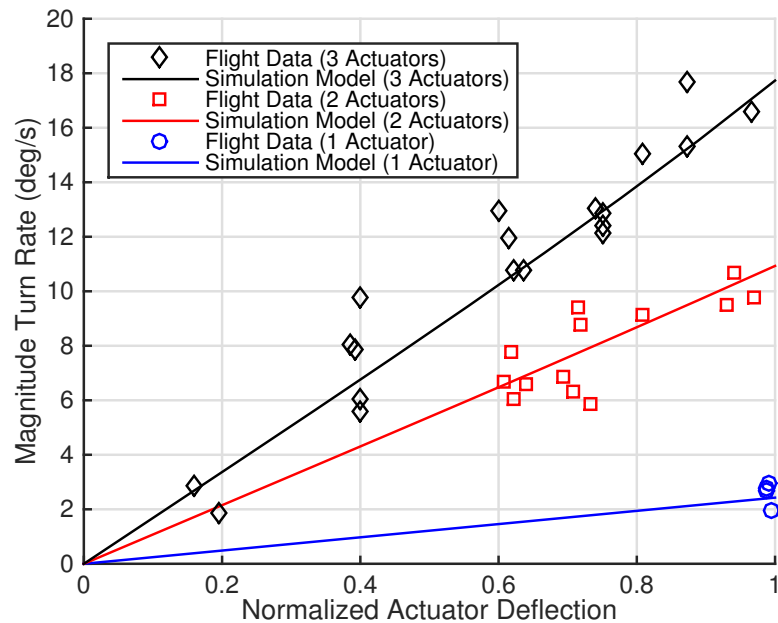


Figure 8.2: Comparison of MC-4/5 flight data and simulation model turn rate vs. normalized actuator deflection.

In addition to the turn rate response of the MC-4/5 dynamic model, a similar comparison with flight data is shown in Figure 8.3 where steady-state longitudinal characteristics including estimated airspeed, descent, and glide ratio are presented as functions of vehicle turn rate. Again, the simulation model closely matches the observed vehicle response in flight tests and accurately captures the significant increase in vehicle descent rate and decrease in glide ratio with increasing turn rate.

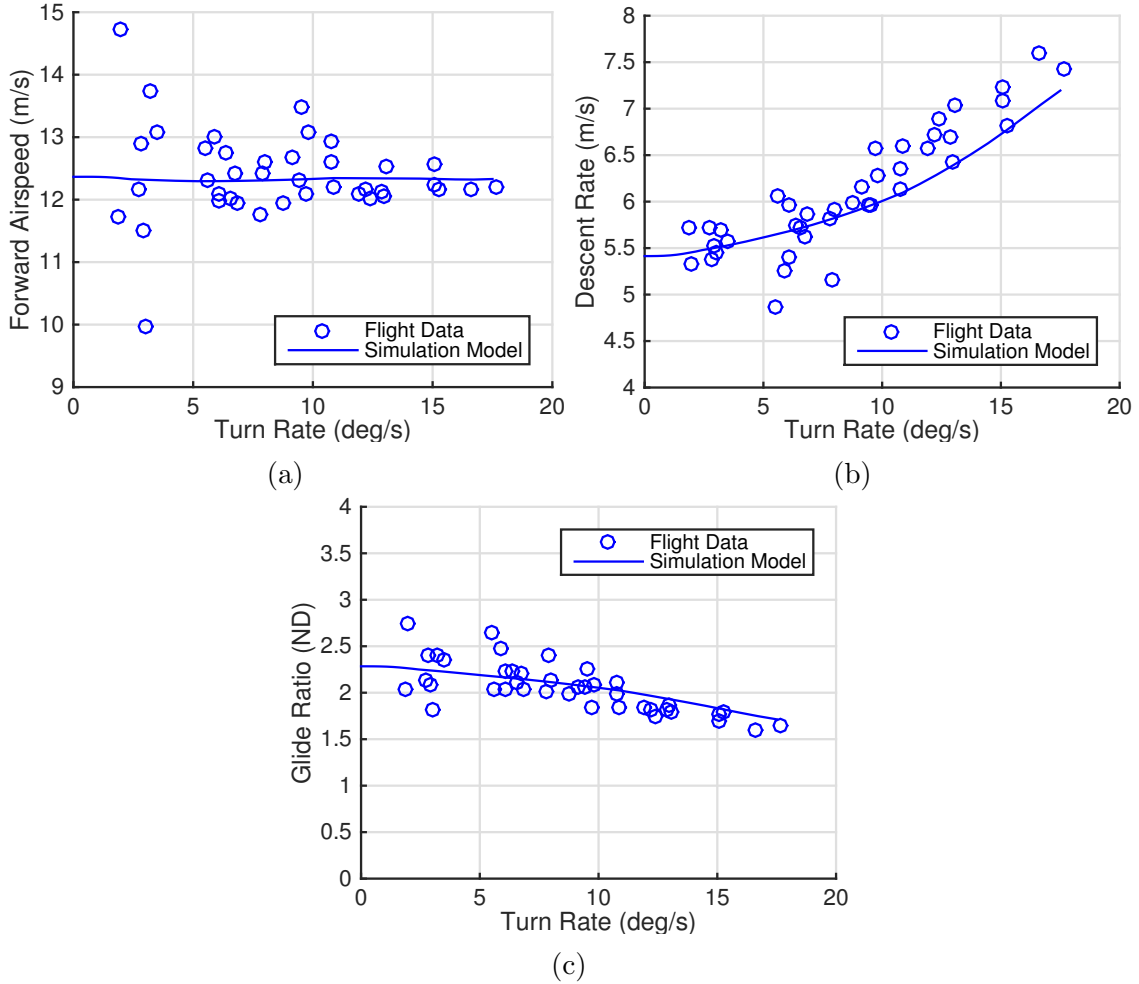


Figure 8.3: Comparison of MC-4/5 flight data and simulation model steady-state flight characteristics using in-canopy bleed air actuators including: (a) airspeed, (b) descent rate, and (c) glide ratio.

8.1.2 Actuator Model

In order to capture the transient dynamics associated with opening and closing the upper surface spoilers, a simple first-order, rate limited dynamic model is developed where the maximum actuation speed is dependent on the required force needed to open the upper surface spoiler. As shown previously, required actuation force is linear with increasing vertical deflection of the upper surface bleed air vent. Consequently, small deflections provide minimal resistance to the in-canopy actuator motor and the resulting actuation speeds are nearly equal to the maximum (i.e. no load) speed of

the actuator. Larger deflections require significantly higher actuation forces leading to much slower actuation speeds due to the increased load on the motor.

Six additional states, denoted $L_j(t)$, are added to the 6 DOF vehicle model representative of the actual control line length extending from each of the six in-canopy actuators where $j = 1, \dots, 6$. At each integration time step, required vertical actuation force, denoted $F_{req,j}$, is computed by multiplying the corresponding vertical displacement of the upper surface spoiler Δh_j with the equivalent spring constant K_{eq} discussed in Section 7.3. An equivalent control line tension, denoted $T_{req,j}$, is then computed using equation (8.4) where h_0 represents the inflated cell height of the MC-4/5 canopy (refer Figure 7.4). Note the required control line tension is doubled for the inner four actuators configured to open two separate upper surface spoilers simultaneously.

$$F_{req,j} = \Delta h_j K_{eq} \quad (8.3)$$

$$T_{req,j} = \begin{cases} \frac{1}{2} F_{req,j} L_j (h_0 - \Delta h_j)^{-1}, & \text{if } j = 2, \dots, 5 \\ \frac{1}{4} F_{req,j} L_j (h_0 - \Delta h_j)^{-1}, & \text{otherwise} \end{cases} \quad (8.4)$$

Using the equivalent control line tension shown above, maximum control line deflection rate $\dot{L}_{max,j}$ for each in-canopy actuator is computed from the in-canopy actuator performance curve as shown in equation (8.5). Here, the actuator performance curve is approximated using a simple linear relationship between the maximum unloaded speed N_{max} of the actuator (i.e. maximum spool rotation rate) and the measured actuator torque at stall τ_{stall} . Note d_s denotes the spool diameter. Additionally, only positive values for maximum control line rates are valid such that any line rate less than or equal to zero indicates the actuator is stalled.

$$\dot{L}_{max,j} = \max \left[\pi d_s \left(N_{max} - \frac{d_s N_{max}}{2 \tau_{stall}} T_{req,j} \right), 0 \right] \quad (8.5)$$

Using this upper limit for control line deflection rate, the actuator equations of motion are calculated as shown below. Note $L_{c,j}$ denotes the commanded control line length.

$$\dot{L}_j = \begin{cases} -\dot{L}_{max,j}, & \text{if } \frac{1}{\alpha} (L_{c,j} - L_j) < -\dot{L}_{max,j} \\ \pi d_s N_{max}, & \text{if } \frac{1}{\alpha} (L_{c,j} - L_j) > \pi d_s N_{max} \\ \frac{1}{\alpha} (L_{c,j} - L_j), & \text{otherwise} \end{cases} \quad (8.6)$$

Three different conditions exist in equation (8.6). The first condition represents the situation where the calculated line rate using a simple first order filter model exceeds the upper limit imposed by the actuator performance curve. Here negative line rates indicate the actuator is reeling in control line and subsequently increasing the upper surface spoiler opening. As a result, the control line rate is simply equal to the maximum line rate given the actuation force required. Alternatively, the second condition represents the case where the in-canopy actuator is closing the upper surface spoiler and the calculated line rate exceeds the maximum unloaded speed of the actuator. Note the maximum unloaded speed of the actuator is used to simulate the effect of the internal pressure within the canopy working with the desired actuation direction rather than against it. Lastly, the third condition represents the case where the calculated line rate is within the specified rate limits. Note the filter constant α is set to match the transient dynamics of the actuator.

In an effort to validate the in-canopy actuator dynamic model, Figure 8.4 compares the simulated response of the in-canopy actuator dynamic model to that observed in flight for a simple step change in commanded control line length. Note Figure 8.4 presents the results in terms of $\Delta L(t)$ such that $\Delta L(t) = L_0 - L(t)$ where L_0 represents

the nominal control line length. Accordingly, the simulated actuator response closely matches that observed during flight indicating a high degree of confidence in both the actuator performance curve and the predicted actuation force required to open the upper surface spoiler. Additionally, Table 8.3 provides a summary of all parameters and their respective values used within the in-canopy actuator dynamic model.

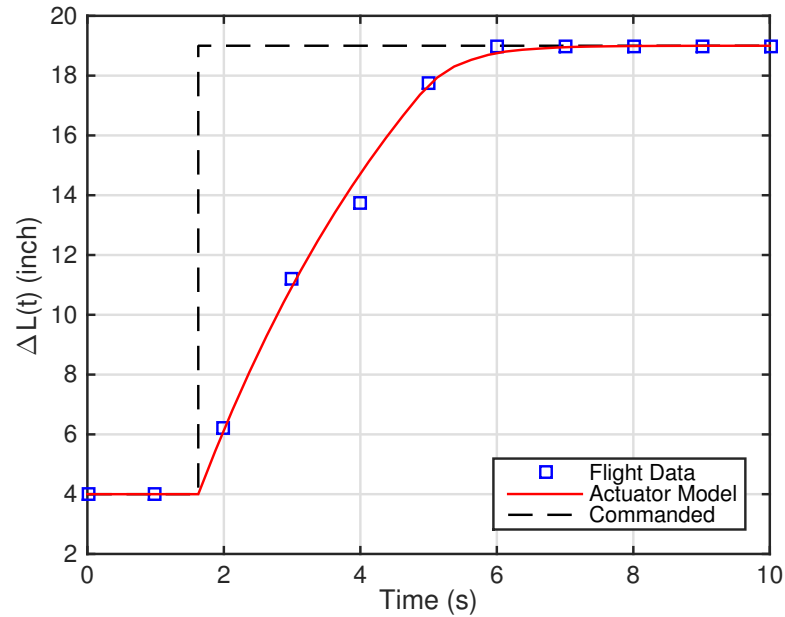


Figure 8.4: Comparison of MC-4/5 in-canopy actuator step response during flight with in-canopy actuator dynamic model.

Table 8.3: MC-4/5 in-canopy actuator model parameters.

Parameter	Value	Units
Equivalent Spring Constant, K_{eq}	1.109	lb/inch
Inflated Cell Height, h_0	28.9	inch
Inflated Cell Width, b_0	20.7	inch
Unloaded Speed, N_{max}	133.0	RPM
Stall Torque, τ_{stall}	60.0	oz-inch
Spool Diameter, d_s	0.75	inch
Filter Constant, α	0.6	—

8.2 In-Canopy Steering and Glide Slope Control

Lateral and longitudinal steering using in-canopy actuators is significantly different from that of conventional two channel systems and requires specification of six unique inputs to achieve the desired vehicle response. Although the general strategy of inverting the known control mapping obtained from prior system identification is largely the same, the actual process for creating these one-to-one mappings for systems using in-canopy actuators is nontrivial. Accordingly, the following sections discuss lateral steering only and combined lateral and longitudinal control mappings for the MC-4/5 system employing six individual in-canopy actuators.

8.2.1 Lateral Steering Only

As shown previously, three different asymmetric spoiler configurations were tested in flight where 1, 2, and 3 outboard actuators were driven simultaneously thus creating the known turn rate response shown in Figure 8.2. Although inversion of any one of the three turn rate response curves is trivial, the more pressing issue is how to properly choose which mapping to use during flight. The most general solution is to simply reduce the mapping to a simple two channel system where three in-canopy actuators on either side of the canopy centerline are driven simultaneously yielding the most lateral control authority of the vehicle. However, this approach is largely inefficient for low turn rates where half of the total upper surface spoilers are only partially opened. Alternatively, the lateral steering controller could actively switch between each of the three mappings depending on the commanded turn rate magnitude such that only those upper surface spoilers nearest the canopy wingtip are used for steering at low to moderate turn rates. This strategy is clearly more efficient given its prioritization of outboard spoilers for low to moderate turn rates; however, a sharp discontinuity exists when switching between turn rate mappings in which two or more actuators are required to move in opposite directions.

In order to eliminate the sharp discontinuity yet preserve the inherent prioritization of an “outboard-in” steering approach, a slightly different turn rate strategy is proposed in Figure 8.5 where the dashed lines represent the additional turn rate achieved with increasing deflection of the second and third in-canopy actuators while keeping any outboard actuators at their maximum opening. More specifically, for turn rates above $\dot{\psi}_1$, the furthest outboard actuator is kept fully open while the next inboard actuator is subsequently opened as needed according to the dashed red line shown in Figure 8.5. Similarly, for turn rates above $\dot{\psi}_2$, the outer two actuators are kept fully open while the furthest inboard actuator is subsequently opened as required to achieve the commanded turn rate.

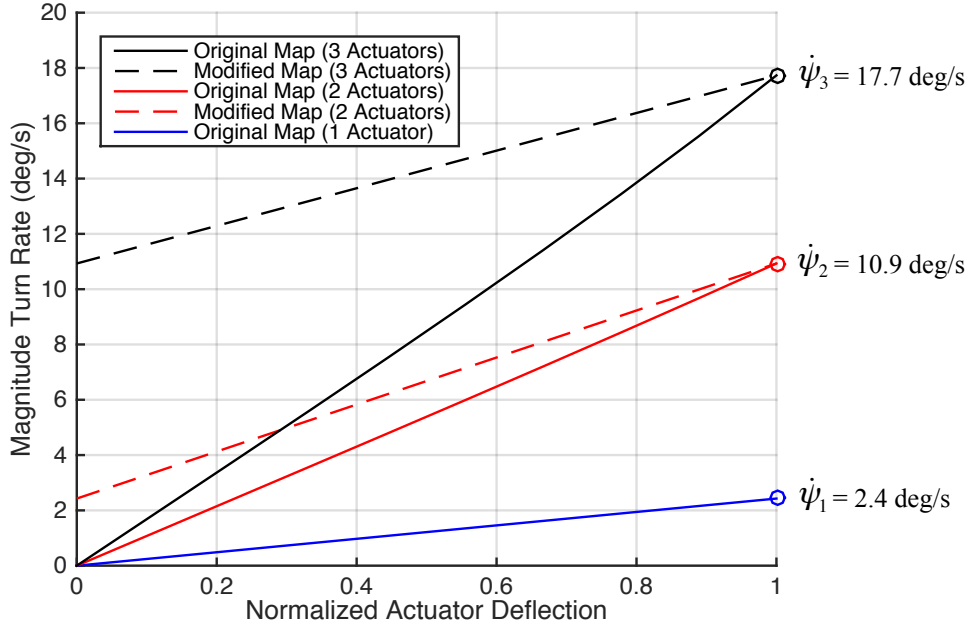


Figure 8.5: MC-4/5 modified turn rate response using in-canopy actuators.

In addition to eliminating any sharp discontinuities and maintaining an “outboard-in” steering strategy, only three unique parameters, namely $\dot{\psi}_1$, $\dot{\psi}_2$, and $\dot{\psi}_3$, are required from system identification in order to fully define the lateral control only turn rate mapping. Note $\dot{\psi}_1$, $\dot{\psi}_2$, and $\dot{\psi}_3$ denote the estimated turn rates at full deflection of 1, 2, and 3 outboard actuators, respectively. Figure 8.6 presents the modified

turn rate mapping used by the onboard GN&C algorithm for lateral steering only. A graphical depiction of the upper surface spoiler opening configuration for two example commanded turn rates is also shown. Note the shading within each canopy cell in Figure 8.6 is proportional to the upper surface spoiler opening where each fully shaded cell represents maximum opening of the upper surface spoiler.

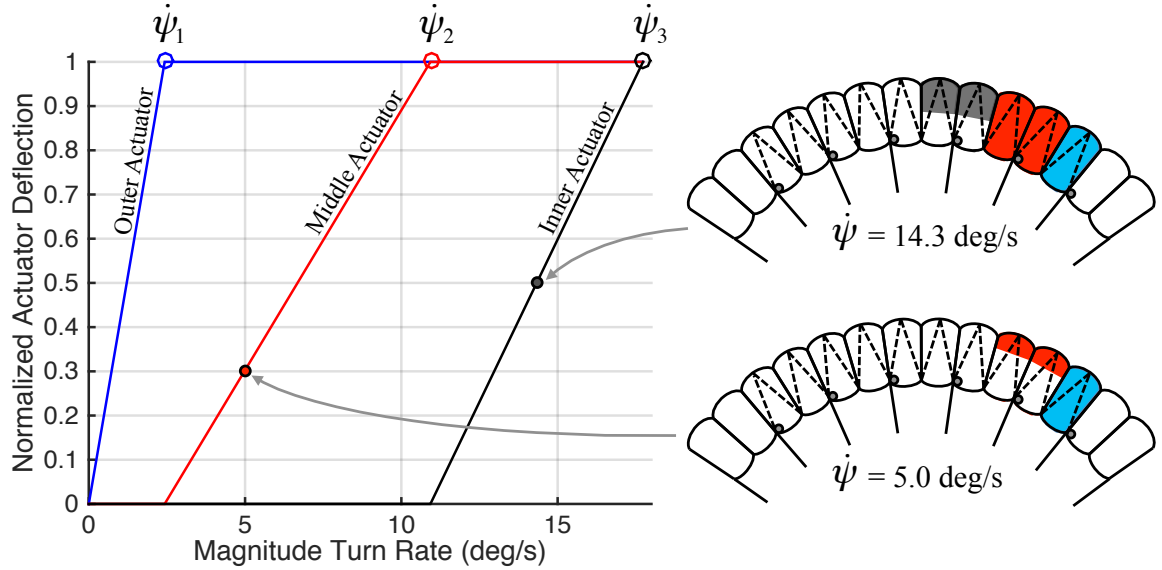


Figure 8.6: MC-4/5 turn rate mapping using in-canopy actuators.

8.2.2 Combined Lateral and Longitudinal Control

Before developing the combined lateral and longitudinal control mapping, an accurate understanding of both lateral and longitudinal vehicle response to different upper surface spoiler openings is required. Consequently, a wide range of both asymmetric and symmetric openings must be investigated in order to fully define the maximum control authority of the vehicle.

In Section 8.1.1, equations (8.1) and (8.2) are defined in order to compute the overall asymmetric and symmetric spoiler deflections, denoted δ_a and δ_s , respectively, given the six individual in-canopy actuator deflections. However, both δ_a and δ_s are not completely independent quantities but rather highly coupled creating a

unique turn rate and glide slope response inherent to the upper surface spoiler control mechanism. Although the term *symmetric* is loosely applied, any asymmetric spoiler deflection also includes some level of nonzero symmetric deflection. Consider the situation shown in Figure 8.7a where the two outboard in-canopy actuators nearest the left wingtip are fully open ($\delta i_1 = \delta i_2 = 1.0$) while all other actuators remain closed. According to equations (8.1) and (8.2), the calculated asymmetric and symmetric spoiler deflection values are 0.64 and 0.30, respectively. However, it must be noted that for the current level of asymmetric spoiler deflection, the computed value of symmetric deflection is not unique and can be increased further by simply opening the inner two actuators equal amounts ($\delta i_3 = \delta i_4 > 0$). This latter configuration is shown in Figure 8.7b where the inner two in-canopy actuators are also fully open ($\delta i_3 = \delta i_4 = 1.0$) in which case the calculated asymmetric and symmetric spoiler deflection values are now 0.64 and 0.70, respectively.

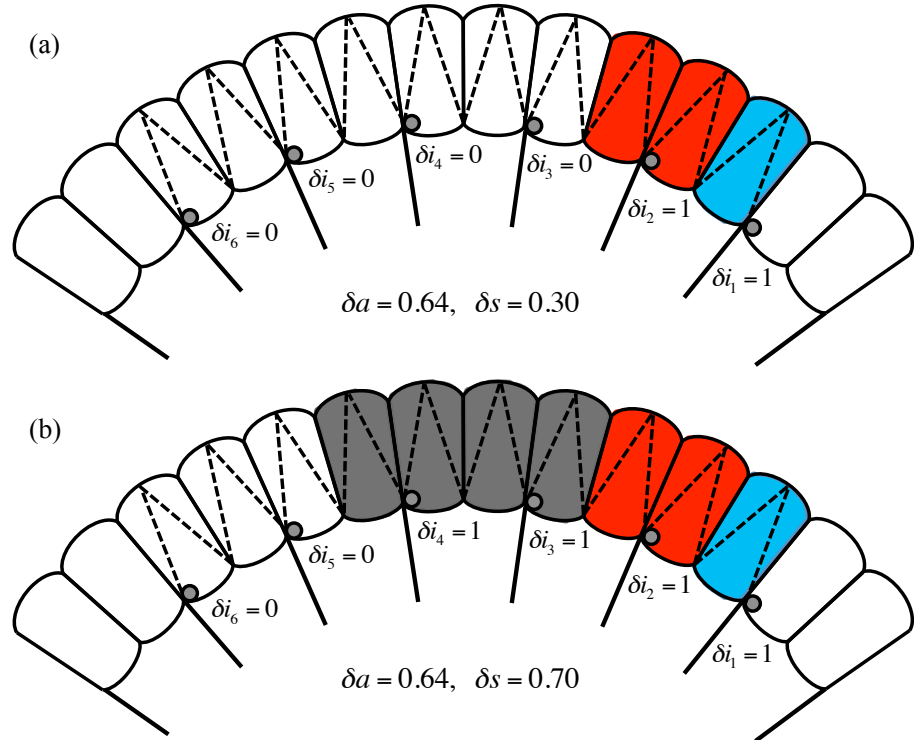


Figure 8.7: MC-4/5 spoiler configuration (front view) with (a) minimum and (b) maximum symmetric deflection, δs , for equivalent asymmetric deflection, δa .

In practice, what this exercise demonstrates is that for nearly any given turn rate (i.e. asymmetric spoiler deflection), a range of feasible glide ratios is achieved by simply varying the overall symmetric spoiler deflection level. In order to better define the process for controlling the vehicle glide ratio given some commanded turn rate and glide ratio computed by the onboard GN&C algorithm, the concept of base spoiler deflection, denoted δb , is introduced where $\delta b \in [0, 1]$. In this context, base spoiler deflection represents some nonzero deflection added to all in-canopy actuators. If the condition exists where one or more in-canopy actuators exceed the maximum allowable opening ($\delta i_j > 1.0$), the overflow amount is simply subtracted from the corresponding actuator mirrored across the canopy centerline in an effort to maintain the same asymmetric opening. For example, consider again the two configurations shown in Figure 8.7. In Figure 8.7a, it is clear that the base spoiler deflection level is zero such that the only deflection of the in-canopy actuators is that required to achieve the desired turn rate. Alternatively, Figure 8.7b demonstrates the extreme case where $\delta b = 1.0$ such that all actuator deflections are increased by a value of 1.0. Accordingly, the excess deflection of the outer two actuators on the left wingtip is simply subtracted from the outer two actuator deflections on the right wingtip resulting in the final configuration shown in Figure 8.7b.

Using this same logic, Figure 8.8 presents the results of a series of virtual system identification flights using the MC-4/5 dynamic model where the resulting steady-state glide ratio is shown as a function of steady-state turn rate at three different base spoiler deflections, namely $\delta b = 0.0, 0.5$, and 1.0 . Note the shaded gray region shown in Figure 8.8 denotes the maximum control authority of the MC-4/5 system given all feasible combinations of asymmetric and symmetric spoiler deflection and forms the basis for the combined lateral and longitudinal control mapping. Given any turn rate and glide ratio commanded by the onboard GN&C algorithm that lies within this shaded region, the required inputs necessary to meet these commanded

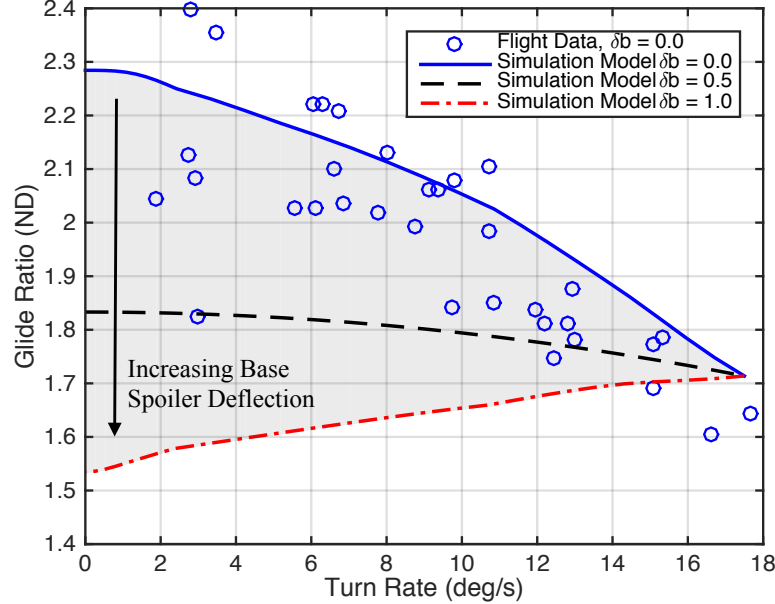


Figure 8.8: Lateral and longitudinal control mapping for the MC-4/5 system using in-canopy actuators.

values are determined according to the known inputs which uniquely define each point within the mapping.

Two additional points must be noted about the turn rate and glide slope mapping shown in Figure 8.8. First, all system identification flights of the MC-4/5 system using in-canopy actuators were at a base spoiler deflection of $\delta b = 0$. Consequently, only the upper limit of the shaded region shown in Figure 8.8 is based on actual flight data while all other points where $\delta b > 0$ are predicted steady-state characteristics determined numerically using the MC-4/5 dynamic simulation model and the newly estimated aerodynamic coefficients. However, the performance of the MC-4/5 simulation model is believed to adequately represent the general trend of the physical system over its entire range of feasible control inputs where any discrepancies that may exist are relatively minor and do not significantly affect the overall result. Second, the range of possible glide ratios significantly decreases as turn rate increases. This result reflects the inherent prioritization of turn rate over glide ratio in that as

more upper surface spoilers are used to achieve higher turn rates, the effect of increasing base spoiler deflection is essentially canceled from the overflow of those spoilers used for lateral steering. If the commanded glide ratio falls outside the predicted range shown in Figure 8.8 for some commanded turn rate (i.e. above or below the gray shaded region), the base spoiler deflection is simply saturated until either the commanded turn rate decreases providing an increased range of feasible glide ratios or the commanded glide ratio returns to a value within range.

8.3 Autonomous Landing Performance in Simulation

Using the updated parafoil and payload system dynamic model, a series of Monte Carlo simulations are conducted over a variety of atmospheric conditions in order to investigate the autonomous landing performance of the MC-4/5 system using in-canopy bleed air actuators for both lateral steering only and combined lateral and longitudinal control. In total, 250 simulated landings were performed for each control strategy. Mean wind speed was varied uniformly from 0 – 10 m/s while turbulence level was fixed at 0.65 m/s. Uncertainty in the assumed control mapping was also included where the assumed turn rate response was both scaled using a constant gain and shifted to create a nonzero turn rate bias. Similar to the small scale test vehicle, several initial conditions including vehicle north and east position and initial heading angle were varied to simulate uncertainty in the release point of the vehicle from the parent aircraft. Note all simulations were conducted from a starting altitude of 3000 m. The GN&C update rate was set to 1 Hz in order to mimic that typically used for large scale parafoil and payload aircraft. Table 8.4 details the variation in all parameters used within the Monte Carlo simulation. Again, mean wind direction was fixed due north for simplicity. Perturbations about the wind fixed frame origin, denoted Δx and Δy , were set to 600 m each to ensure that all flights received an equal chance of reaching the target area.

Table 8.4: MC-4/5 Monte Carlo simulation parameters.

Variable Description	Symbol	Value	Units
Mean North Wind	$\bar{V}_{W,x}$	unif(0, 10)	m/s
Mean East Wind	$\bar{V}_{W,y}$	0	m/s
Mean Vertical Wind	$\bar{V}_{W,z}$	0	m/s
Turbulence Level	σ_W	0.65	m/s
Turn Rate Gain	—	unif(0.8, 1.2)	—
Turn Rate Bias	—	unif(-0.06, 0.06)	rad/s
I.C.	x_0	$(z_0/w_0)\bar{V}_{W,x} + \text{unif}(0, \Delta x)$	m
I.C.	y_0	unif(0, Δy)	m
I.C.	z_0	-3000	m
I.C.	ϕ_0	0	rad
I.C.	θ_0	0	rad
I.C.	ψ_0	unif(0, 2π)	rad
I.C.	u_0	13.5	m/s
I.C.	v_0	0	m/s
I.C.	w_0	6.5	m/s
I.C.	p_0	0	rad/s
I.C.	q_0	0	rad/s
I.C.	r_0	0	rad/s

Figure 8.9 compares the simulated landing dispersion of the MC-4/5 using in-canopy actuators for both lateral steering only and combined lateral and longitudinal control. Again, impact point errors are computed from the simulated GPS measurements at the point of impact and presented in a down wind and cross wind reference frame based on the estimated ground wind direction at the instant the vehicle lands. Miss distances in terms of 50% and 90% CEP for the lateral steering only case are recorded as 25.5 m and 58.9 m, respectively. Mean miss distance is also computed as 29.5 m. As expected, landing accuracy is significantly improved when using the combined lateral and longitudinal control logic where 50% and 90% CEP values are recorded as 16.2 m and 36.7 m, respectively, with a mean miss distance of 19.8 m. Relative performance of the MC-4/5 system indicates a 36% reduction in 50% CEP over lateral steering only. Note this improvement in landing accuracy is nearly identical to that predicted in simulation for the small scale test vehicle.

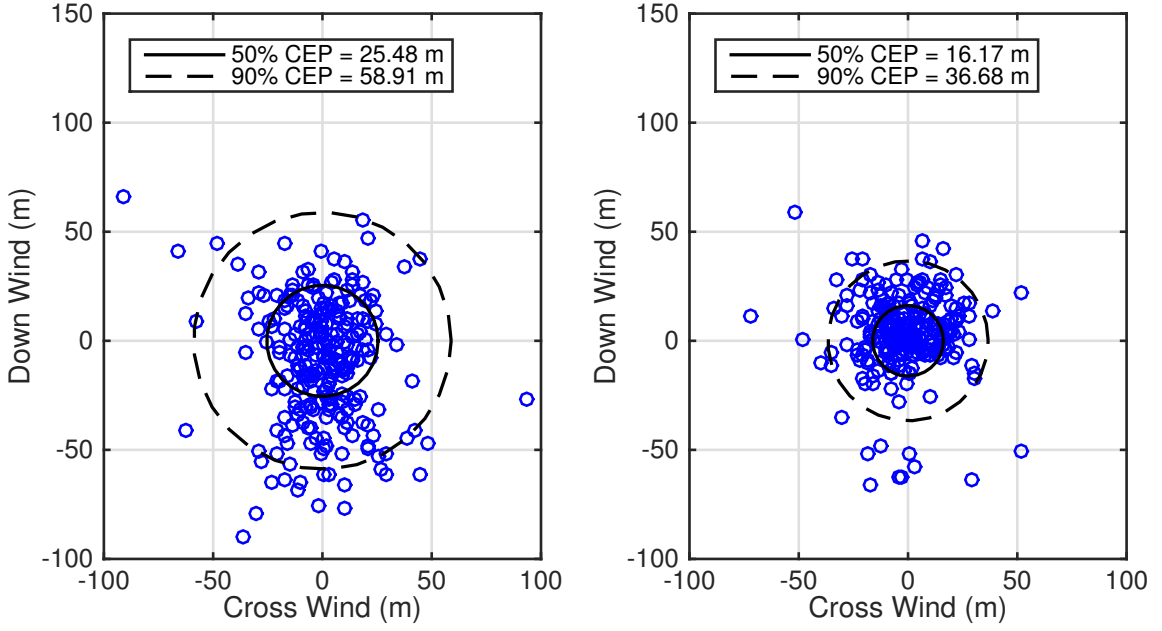


Figure 8.9: Simulated landing dispersion of MC-4/5 system using in-canopy actuators for (left) lateral only control and (right) combined lateral and longitudinal control.

In addition to the simulated landing dispersions shown above, Figure 8.10 compares the mean landing accuracy for both lateral steering control only and combined lateral and longitudinal control with increasing turbulence at four different mean wind speeds, namely 0, 3, 9, and 14 m/s. Note that the nominal forward airspeed of the MC-4/5 system is approximately 12.5 m/s such that the four mean wind speeds considered range from zero up to that exceeding the nominal airspeed of the vehicle. Each marker shown in Figure 8.10 represents a series of 100 autonomous landings with uncertainty in all parameters, excluding mean wind speed and turbulence level, determined according to Table 8.4. In total, 2400 simulations were conducted for both the lateral only and combined lateral and longitudinal control logic cases for a total of 4800 simulated autonomous landings. Similar to the results shown for the small scale test vehicle, the combined lateral and longitudinal control logic is most effective at reducing mean miss distance at low mean wind speeds where the wind direction is constantly changing. These conditions are often referred to as “light and variable” winds and represent some of the more challenging atmospheric conditions

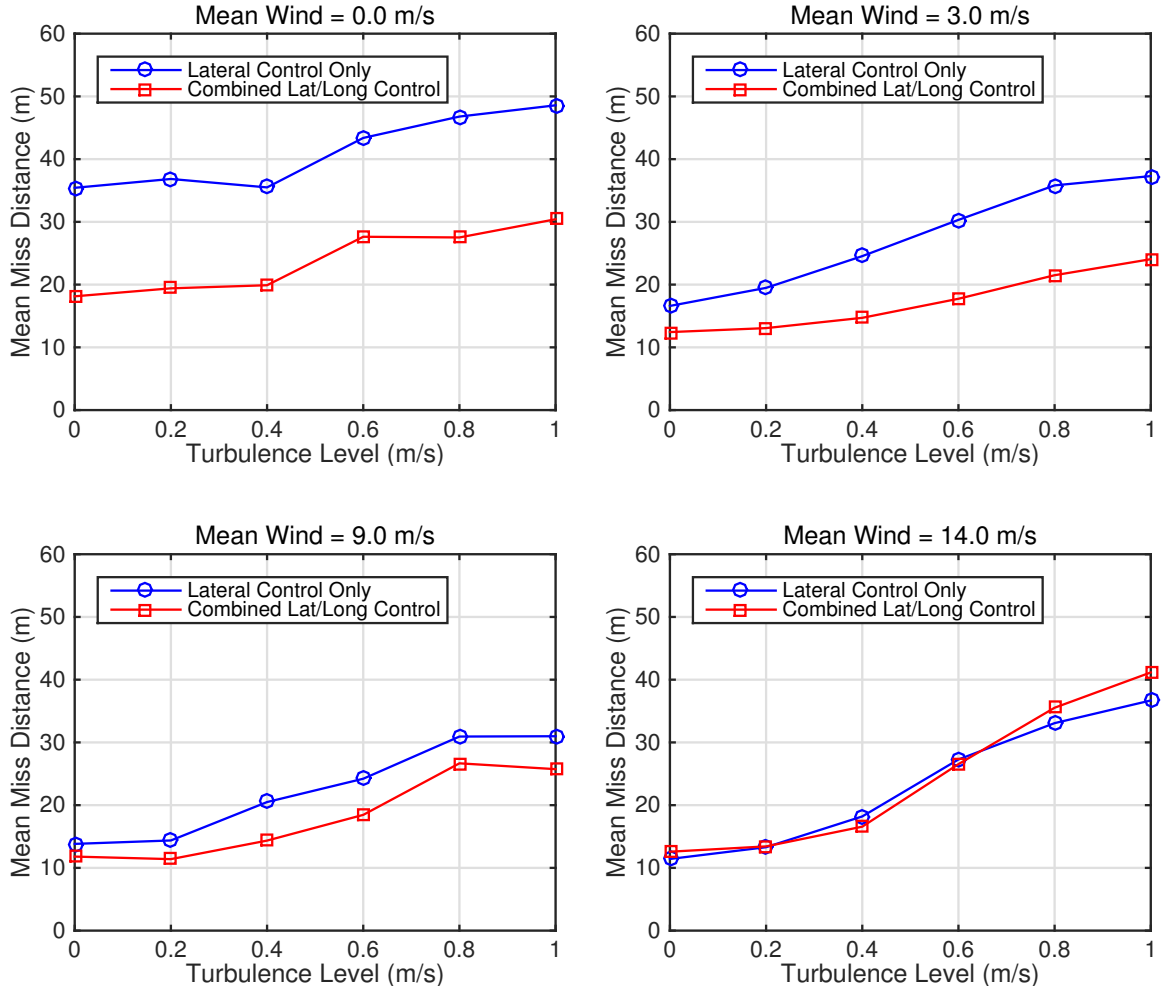


Figure 8.10: MC-4/5 landing accuracy comparison between lateral only and combined lateral and longitudinal control vs. turbulence for different values of mean wind.

for autonomous parafoil aircraft with limited longitudinal control. As seen in Figure 8.10, the combined lateral and longitudinal control logic is able to reduce mean miss distance by nearly 50% over the entire range of turbulence levels considered at zero mean wind. Additionally, mean miss distance is shown to steadily increase with increasing turbulence over all four mean wind speeds considered. However, it must be noted that the relative improvement in mean miss distance when using the combined lateral and longitudinal control logic diminishes slightly with increasing mean wind speed to the point where no apparent improvement is evident at 14 m/s. Again, this result is expected given that longitudinal control using upper surface canopy spoilers

is most effective in relatively gusty conditions where the mean wind is constantly changing direction, i.e. low mean wind speeds with high levels of turbulence.

8.4 Autonomous Landing Performance in Flight Tests

In addition to the simulated autonomous landing performance of the MC-4/5 using in-canopy actuators, a total of three fully autonomous flight tests from canopy opening to ground impact are reported demonstrating the capability of the in-canopy actuation system for control of large scale parafoil aircraft. All flight tests were performed over two days of testing in Eloy, Arizona (March 11–12, 2015) in conjunction with the Natick Soldier Research, Development and Engineering Center (NSRDEC) Airdrop Technology Team. Total miss distances for each of the three autonomous flights include 192.2 m, 24.1 m, and 33.5 m. Note upper surface spoilers were used only for lateral steering as opposed to both lateral and longitudinal control. Approximate deployment altitude was 10,000 ft (3048 m) above ground level.

Despite such few recorded landings, it must be noted that miss distances of both 24.1 m and 33.5 m are truly unprecedented and represent the first ever fully autonomous flights of a large scale parafoil and payload aircraft in which all actuators necessary for control are mounted entirely within the parafoil canopy itself. Furthermore, the one landing with a total miss distance of 192.2 m was severely compromised by a drastic reduction in mean wind speed from over 8 m/s to nearly 0 m/s during the last portion of the flight resulting in significant overshoot of the intended target. Nevertheless, this flight serves as the quintessential example justifying the need for longitudinal control where unknown changes in the assumed winds nearest ground level often result in significant impact point errors.

Figures 8.11 and 8.12 present the inertial frame vehicle trajectory and estimated north and east wind components with changing altitude for the second test flight with a miss distance of 24.1 m. Note for this flight, the estimated winds are relatively

calm and blowing mostly toward the northwest direction at speeds less than 3 m/s. Additionally, Figure 8.13 presents the commanded and estimated vehicle heading rate time history during autonomous flight. Accordingly, the MC-4/5 system demonstrates excellent lateral control authority using in-canopy actuators evidenced by its ability to properly track heading rates commanded by the onboard GN&C algorithm.

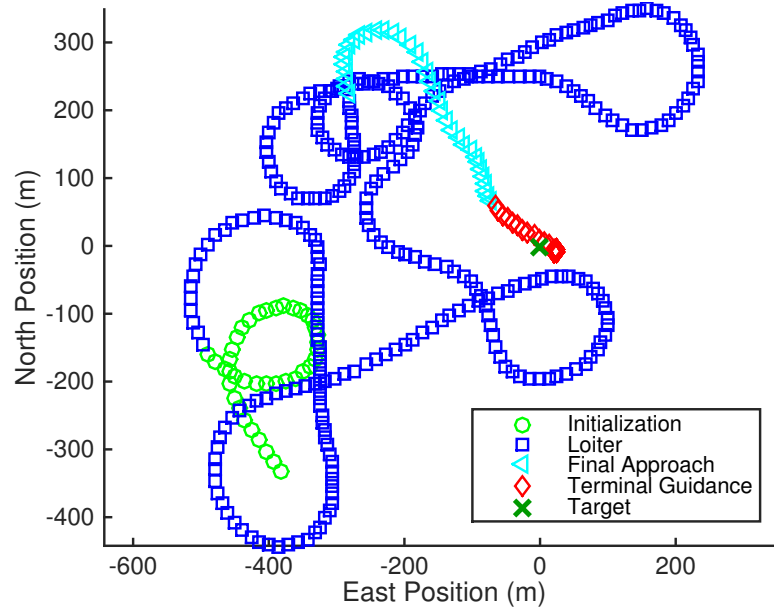


Figure 8.11: Vehicle trajectory relative to inertial frame during MC-4/5 fully autonomous test flight using in-canopy actuators.

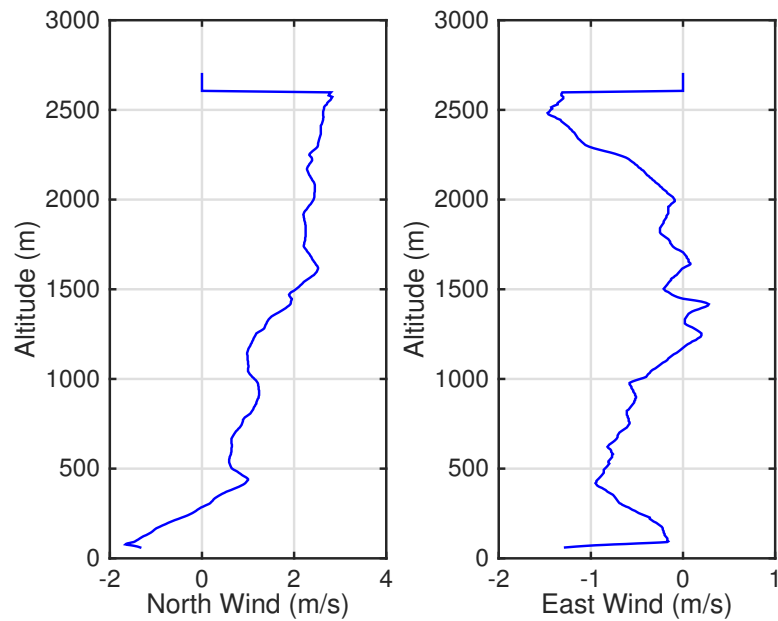


Figure 8.12: Estimated north and east wind components during MC-4/5 autonomous flight.

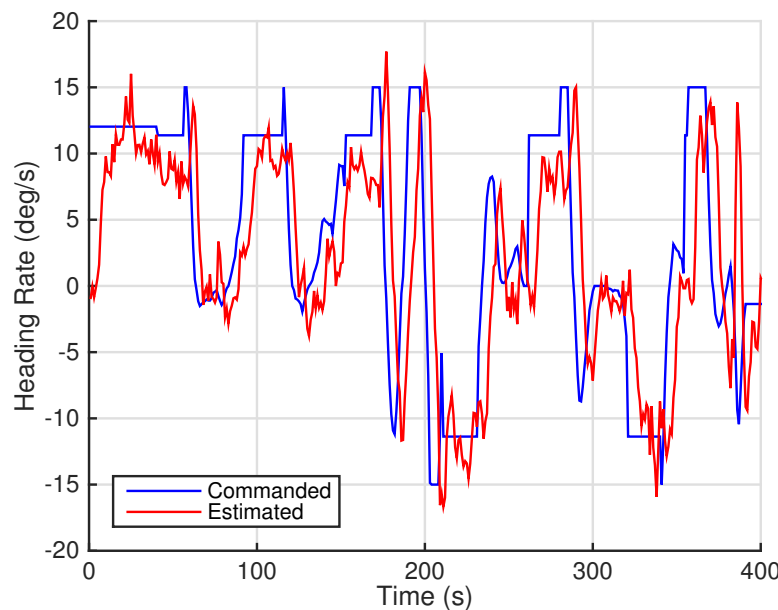


Figure 8.13: Commanded and estimated vehicle heading rate during MC-4/5 fully autonomous test flight.

CHAPTER IX

CONCLUSIONS AND FUTURE WORK

9.1 Conclusions

This dissertation explored the use of upper surface canopy spoilers for control of autonomous parafoil and payload aircraft. Simulation studies and experimental flight tests were largely in good agreement indicating that bleed air control is extremely effective in not only lateral steering but also precise longitudinal control of the vehicle dynamics. For the case where upper surface spoilers are used only for lateral steering, resulting turn rates of the vehicle were shown to exceed the typical range required for autonomous flight. Additionally, autonomous landing statistics in both simulation and experimental flight tests using only lateral steering demonstrated that upper surface spoilers provide an equivalent level of accuracy when compared with that of conventional trailing edge deflection mechanisms. With the addition of specialized control logic designed to leverage the added longitudinal control authority of upper surface spoilers, significant improvements in landing accuracy were reported in which miss distances are reduced by nearly a factor of two.

In addition to providing substantial lateral and longitudinal control authority and improved landing accuracy, upper surface spoilers require significantly less actuation force when compared to conventional trailing edge deflection. As a result, this dissertation also presented the design, development, and flight testing of a novel in-canopy bleed air actuation system suitable for large scale autonomous parafoil and payload aircraft. In this configuration, all required actuation hardware necessary for control was contained entirely within the parafoil canopy using several lightweight, low-power

winch actuators with embedded wireless connectivity. For comparison with conventional trailing edge control of the MC-4/5 system, the in-canopy actuation hardware accounted for nearly a 10 times reduction in total weight compared to the typical AGU. Additionally, maximum torque of one trailing edge brake actuator for the MC-4/5 is over 17 times more than that of a single in-canopy bleed air actuator. In practice, the in-canopy bleed air actuation system has been shown to work extremely well. Several fully autonomous flights of the MC-4/5 system have been performed demonstrating the capability of the in-canopy actuation system for large scale autonomous parafoil aircraft. Accordingly, continued development of this technology could provide the opportunity for not only significant reductions in cost, size, and rigging complexity of conventional systems, but also increase the control effectiveness, performance, and landing accuracy of currently fielded autonomous parafoil aircraft through bleed air control.

9.2 Recommended Future Work

The results of this dissertation have established that upper surface canopy spoilers are a viable mechanism for autonomous control of parafoil and payload aircraft. Accordingly, several opportunities for future work are briefly described below that could both expand upon the findings described here and help improve the control effectiveness and robustness of the upper surface spoiler control mechanism with the ultimate goal of transitioning reliable and highly accurate bleed air control technologies to currently fielded autonomous airdrop systems.

In the current work, all canopy aerodynamic forces are assumed to act at a single point. Although this simplistic model is both computationally efficient and agrees favorably with observed flight characteristics for both small and large scale parafoil and payload aircraft, it is not well suited for studying different upper surface spoiler configurations where both the number and spanwise location of the upper surface

openings are varied. One particularly useful extension would be to model the parafoil canopy as a discrete set of connected elements where each element represents that of a single cell given the overall size and shape of the inflated canopy. Although this discrete element aerodynamic model has previously been applied to parafoil and payload aircraft [53, 54] with good results, extension of this model to include the effects of upper surface spoilers is relatively new. Lift and drag for each cell could be supplemented with data acquired through CFD given the specific shape and chordwise location of the upper surface spoiler opening.

The design and shape of the upper surface spoiler opening could be further investigated with the goal of both improving lateral and longitudinal control effectiveness and reducing the actuation loads required to open the upper surface vent. Other shapes, including rectangular, triangular, or even circular openings, could prove more effective for both lateral and longitudinal control of the vehicle when compared to that of a single spanwise slit. Also, the orientation of the expelled stream of high pressure ram air relative to the canopy upper surface could be varied to further manipulate the associated aerodynamic forces and moments acting on the canopy. Although the current work only considers the performance of flows normal to the upper canopy surface, tangential flows may also prove beneficial.

Regarding the in-canopy bleed air actuation system, several exciting opportunities exist in terms of control law development. First, an adaptive control strategy is greatly needed to improve the robustness of the entire system in the event that one or more actuators fail during flight. Although systems using conventional trailing edge brakes for control are similarly at risk of failed actuators, the in-canopy bleed air actuation system is unique in that loss of one or even two actuators is unlikely to prevent turn rates in one direction altogether. Accordingly, recognizing and actively compensating for one or more failed actuators while still maintaining the ability to steer in either direction is extremely powerful. Also, all turn rate and glide ratio mappings

are essentially static mappings determined from prior system identification. Incorporating the ability to actively estimate and update these mappings in-flight would significantly improve control law robustness and reduce the dependence on careful system identification and control mechanism characterization prior to autonomous flight. Second, the idea of binary control where each individual in-canopy actuator is either fully open or fully closed is very promising. This idea of binary control not only reduces the complexity of the onboard control algorithm by eliminating the need for continuous specification of control line length but also reduces the hardware requirements and cost of each individual in-canopy actuator by removing the need for rotary encoders providing continuous spool position feedback.

REFERENCES

- [1] Knacke, T., “Technical-Historical Development of Parachutes and Their Applications Since World War I,” *AIAA Paper 86-2423*, 1986.
- [2] Benney, R., Barber, J., McGrath, J., McHugh, J., Noetscher, G., and Tavan, S., “The Joint Precision Airdrop System Advanced Concept Technology Demonstration,” *AIAA Paper 05-1601*, 2005.
- [3] Airborne Systems, “Cargo Delivery Parachute Systems,” <http://www.airborne-sys.com/pages/view/cargo-delivery-parachute-systems> (accessed: 12 August 2014).
- [4] Berland, J.-C., Barber, J., Gargano, B., and Bagdonovich, B. P., “Autonomous Precision Delivery of 42,000 Pounds (19,000 kg) Under One Parachute,” *AIAA Paper 09-2928*, 2009.
- [5] Wright, R., Benney, R., and McHugh, J., “Precision Airdrop System,” *AIAA Paper 05-1644*, 2005.
- [6] Brown, G., Haggard, R., Almassy, R., Benney, R., and Dellicker, S., “The Affordable Guided Airdrop System (AGAS),” *AIAA Paper 99-1742*, 1999.
- [7] Dellicker, S., Benney, R., Patel, S., Williams, T., Hewgley, C., Yakimenko, P., Howard, R., and Kaminer, I., “Performance, Control, and Simulation of the Affordable Guided Airdrop System,” *AIAA Paper 00-4309*, 2000.
- [8] Gilles, B., Hickey, M., and Krainski, W., “Flight-Testing of a Low-Cost Precision Aerial Delivery System,” *AIAA Paper 05-1651*, 2005.
- [9] Jalbert, D. C., “Multi-cell wing type aerial device,” Nov. 15 1966, US Patent 3,285,546.
- [10] Menard, G. L. C., Nicolaides, J., and Speelman, III, R. J., “A Review of Para-Foil Applications,” *Journal of Aircraft*, Vol. 7, No. 5, 1970, pp. 423–431.
- [11] Ghoreyshi, M., Seidel, J., Bergeron, K., Jirsek, A., Lofthouse, A. J., and Cummings, R. M., “Prediction of Aerodynamic Characteristics of a Ram-Air Parachute,” *AIAA Paper 14-2831*, 2014.
- [12] Airborne Systems, “Product Listing,” <http://www.airborne-sys.com/pages/view/firefly> (accessed: 12 August 2014).
- [13] Barton, W. R. and Knapp, C. F., “Controlled Recovery of Payloads at Large Glide Distances, Using the Para-Foil,” *Journal of Aircraft*, Vol. 5, No. 2, 1968, pp. 112–118.

- [14] Sim, A. G., Murray, J. E., Neufeld, D. C., and Reed, R. D., “Development and Flight Test of a Deployable Precision Landing System,” *Journal of Aircraft*, Vol. 31, No. 5, 1994, pp. 1101–1108.
- [15] Murray, J. E., Sim, A. G., Neufeld, D. C., Rennich, P. K., Norris, S. R., and Hughes, W. S., “Further Development and Flight Test of an Autonomous Precision Landing System Using a Parafoil,” *AIAA Paper 94-2141*, 1994.
- [16] Bennett, T. and Fox, R., “Design, Development & Flight Testing of the NASA X-38 7500 ft² Parafoil Recovery System,” *AIAA Paper 03-2107*, 2003.
- [17] Benney, R., Meloni, A., Cronk, A., and Tiaden, R., “Precision Airdrop Technology Conference and Demonstration 2007,” *AIAA Paper 09-2927*, 2010.
- [18] Benney, R., Henry, M., Lafond, K., Meloni, A., and Patel, S., “DoD New JPADS Programs & NATO Activities,” *AIAA Paper 09-2952*, 2009.
- [19] Calise, A. J. and Preston, D., “Swarming/Flocking and Collision Avoidance for Mass Airdrop of Autonomous Guided Parafoils,” *Journal of Guidance, Control, and Dynamics*, Vol. 31, No. 4, 2008, pp. 1123–1132.
- [20] Carter, D., George, S., Hattis, P., Singh, L., and Tavan, S., “Autonomous Guidance, Navigation, and Control of Large Parafoils,” *AIAA Paper 05-1643*, 2005.
- [21] Carter, D., George, S., Hattis, P., McConley, M., Rasmussen, S., Singh, L., and Tavan, S., “Autonomous Large Parafoil Guidance, Navigation, and Control System Design Status,” *AIAA Paper 07-2514*, 2007.
- [22] Carter, D., Singh, L., Wholey, L., Rasmussen, S., Barrows, T., George, S., McConley, M., Gibson, C., Tavan, S., and Bagdonovich, B., “Band-Limited Guidance and Control of Large Parafoils,” *AIAA Paper 09-2981*, 2009.
- [23] Jann, T., “Advanced Features for Autonomous Parafoil Guidance, Navigation and Control,” *AIAA Paper 05-1642*, 2005.
- [24] Kaminer, I. I. and Yakimenko, O. A., “Development of Control Algorithm for the Autonomous Gliding Delivery System,” *AIAA Paper 03-2116*, 2003.
- [25] Slegers, N. J. and Yakimenko, O. A., “Optimal Control for Terminal Guidance of Autonomous Parafoils,” *AIAA Paper 09-2958*, 2009.
- [26] Calise, A. and Preston, D., “Design of a Stability Augmentation System for Airdrop of Autonomous Guided Parafoils,” *AIAA Paper 06-6776*, 2006.
- [27] Yakimenko, O. A., Slegers, N. J., and Tiaden, R. A., *Development and Testing of the Miniature Aerial Delivery System Snowflake*, 2009.
- [28] Gavrilovski, A., Ward, M., and Costello, M., “Parafoil Control Authority with Upper-Surface Canopy Spoilers,” *Journal of Aircraft*, Vol. 49, No. 5, 2012, pp. 1391–1397.

- [29] Slegers, N. and Costello, M., “On the Use of Rigging Angle and Canopy Tilt for Control of a Parafoil and Payload System,” *AIAA Paper 03-5609*, 2003.
- [30] Ward, M., Culpepper, S., and Costello, M., “Parafoil Control Using Payload Weight Shift,” *Journal of Aircraft*, Vol. 51, No. 1, 2014, pp. 204–215.
- [31] Bergeron, K., Fejzic, A., and Tavan, S., “AccuGlide 100: Precision Airdrop Guidance and Control via Glide Slope Control,” *AIAA Paper 11-2530*, 2011.
- [32] Ward, M. and Costello, M., “Adaptive Glide Slope Control for Parafoil and Payload Aircraft,” *Journal of Guidance, Control, and Dynamics*, Vol. 36, No. 4, 2013, pp. 1019–1034.
- [33] Slegers, N., Beyer, E., and Costello, M., “Use of Variable Incidence Angle for Glide Slope Control of Autonomous Parafoils,” *Journal of Guidance, Control, and Dynamics*, Vol. 31, No. 3, 2008, pp. 585–596.
- [34] Moore, J. E., “Drogue Assisted Variable Glide Slope Control,” *AIAA Paper 13-1380*, 2013.
- [35] Bergeron, K., Ward, M., and Costello, M., “Aerodynamic Effects of Parafoil Upper Surface Bleed Air Actuation,” *AIAA Paper 12-4737*, 2012.
- [36] Barrows, T. M., “Apparent Mass of Parafoils with Spanwise Camber,” *Journal of Aircraft*, Vol. 39, No. 3, 2002, pp. 445–451.
- [37] Lissaman, P. B. S. and Brown, G. J., “Apparent Mass Effects on Parafoil Dynamics,” *AIAA paper 93-1236*, 1993.
- [38] Press, W., Teukolsky, S., Vetterling, W., and Flannery, B., *Numerical Recipes: The Art of Scientific Computing*, Cambridge University Press, New York, 3rd ed., 2007.
- [39] u-blox, “LEA-6 Series Positioning Modules,” <http://www.u-blox.com/en/gps-modules/pvt-modules/previous-generations/lea-6-family.html> (accessed: 18 August 2014).
- [40] “Flying Qualities of Piloted Aircraft,” MIL-HDBK-1797, Department of Defense, 1997.
- [41] Moorhouse, D. and Woodcock, R., “Background Information and User Guide for MIL-F-8785C, Military Specification – Flying Qualities of Piloted Airplanes,” *Air Force Wright Aeronautical Laboratories*, 1982.
- [42] Gage, S., “Creating a Unified Graphical Wind Turbulence Model from Multiple Specifications,” 2003.
- [43] Smith, D. R., Amitay, M., Kibens, V., Parekh, D., and Glezer, A., “Modification of Lifting Body Aerodynamic Using Synthetic Jet Actuators,” *AIAA paper 98-0209*, 1998.

- [44] Amitay, M., Smith, D. R., Kibens, V., Parekh, D. E., and Glezer, A., "Aerodynamic Flow Control Over an Unconventional Airfoil Using Synthetic Jet Actuators," *AIAA Journal*, Vol. 39, No. 3, 2001, pp. 361–370.
- [45] Amitay, M. and Glezer, A., "Controlled Transients of Flow Reattachment Over Stalled Airfoils," *International Journal of Heat and Fluid Flow*, Vol. 23, No. 5, 2002, pp. 690 – 699.
- [46] Jann, T., Doherr, K.-F., and Gockel, W., "Parafoil Test Vehicle ALEX – Further Development and Flight Test Results," *AIAA Paper 99-1751*, 1999.
- [47] Jann, T., "Aerodynamic Model Identification and GNC Design for the Parafoil-Load System ALEX," *AIAA Paper 01-2015*, 2001.
- [48] Jann, T., "Aerodynamic Coefficients for a Parafoil Wing with Arc Anhedral: Theoretical and Experimental Results," *AIAA Paper 03-2106*, 2003.
- [49] Jann, T. and Strickert, G., "System Identification of a Parafoil-Load Vehicle – Lessons Learned," *AIAA Paper 05-1663*, 2005.
- [50] Hur, G. and Valasek, J., "System Identification of Powered Parafoil-Vehicle from Flight Test Data," *AIAA Paper 03-5539*, 2003.
- [51] Kothandaraman, G. and Rotea, M., "Simultaneous-Perturbation-Stochastic-Approximation Algorithm for Parachute Parameter Estimation," *Journal of aircraft*, Vol. 42, No. 5, 2005, pp. 1229–1235.
- [52] Yakimenko, O. A. and Statnikov, R. B., "Multicriteria Parametrical Identification of the Parafoil-Load Delivery System," *AIAA Paper 05-1664*, 2005.
- [53] Ward, M., Costello, M., and Slegers, N., "On the Benefits of In-Flight System Identification for Autonomous Airdrop Systems," *Journal of guidance, control, and dynamics*, Vol. 33, No. 5, 2010, pp. 1313–1326.
- [54] Ward, M., Costello, M., and Slegers, N., "Specialized System Identification for Parafoil and Payload Systems," *Journal of Guidance, Control, and Dynamics*, Vol. 35, No. 2, 2012, pp. 588–597.
- [55] Goodrick, T. F., Pearson, A., and Murphy, A. L., "Analysis of Various Automatic Homing Techniques for Gliding Airdrop Systems with Comparative Performance in Adverse Winds," .
- [56] Stengel, R., *Optimal Control and Estimation*, Dover Publications, 1994.
- [57] Ward, M., "Adaptive Glide Slope Control for Parafoil and Payload Aircraft," Ph.D. Dissertation, *Georgia Institute of Technology*, 2012.
- [58] Wamore Inc., "UltraFly Precision Guided Airdrop System Official Product Brochure," <http://www.wamore.com/getdoc/c0b9cd26-aa5c-4261-8023-7c464a2e4756/Ultra-Fly-Brochure-OL.aspx> (accessed: 30 March 2015).

VITA

Edward J. Scheuermann was born and raised in Lafayette, LA. In May of 2009, he received a Bachelor of Science in Mechanical Engineering from Louisiana State University and later went on to work for ExxonMobil as a project engineer in Houston, TX. In August 2010, he entered the Woodruff School of Mechanical Engineering at the Georgia Institute of Technology, receiving an MS in 2012 and continuing his studies to pursue a PhD. His technical interests include dynamic modeling, mechatronics, and control system engineering.